

AD 667798

AFFDL-TR-67-144

Volume I

# INVESTIGATION OF TURBULENT HEAT TRANSFER AT HYPERSONIC SPEEDS

Volume I. Analytical Methods

R. T. Savage

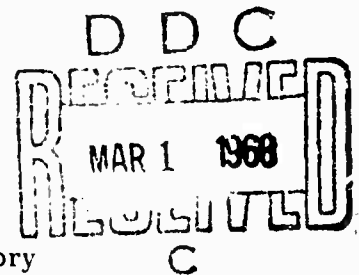
C. L. Jaeck

THE BOEING COMPANY

TECHNICAL REPORT AFFDL-TR-67-144. VOLUME I

December 1967

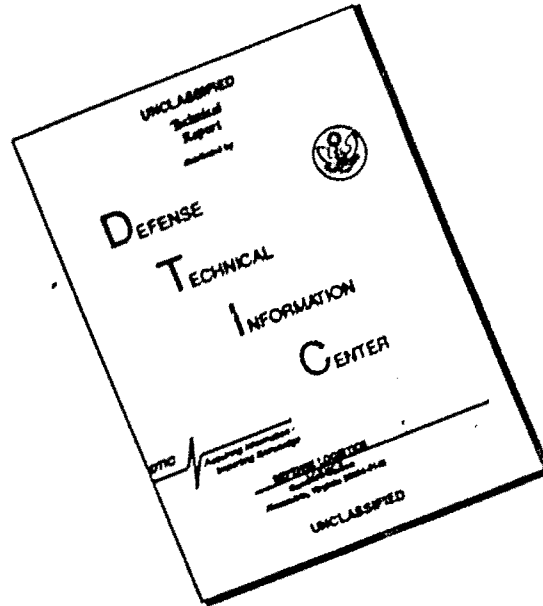
This document has been approved for public release and sale;  
its distribution is unlimited.



Air Force Flight Dynamics Laboratory  
Air Force Systems Command  
Wright-Patterson Air Force Base, Ohio

Reproduced by the  
CLEARINGHOUSE  
for Federal Scientific & Technical  
Information Springfield Va. 22151

# DISCLAIMER NOTICE



THIS DOCUMENT IS BEST QUALITY AVAILABLE. THE COPY FURNISHED TO DTIC CONTAINED A SIGNIFICANT NUMBER OF PAGES WHICH DO NOT REPRODUCE LEGIBLY.

AFFDL-TR-67-144  
Volume I

# INVESTIGATION OF TURBULENT HEAT TRANSFER AT HYPERSONIC SPEEDS

Volume I. Analytical Methods

R. T. Savage  
C. L. Jaeck

THE BOEING COMPANY

TECHNICAL REPORT AFFDL-TR-67-144, VOLUME I

December 1967

This document has been approved for public release and sale;  
its distribution is unlimited.

Air Force Flight Dynamics Laboratory  
Air Force Systems Command  
Wright-Patterson Air Force Base, Ohio

## NOTICES

When government drawings, specifications, or other data are used for any purpose other than in connection with a definitely related government procurement operation, the United States government thereby incurs no responsibility nor any obligation whatsoever; and the fact that the government may have formulated, furnished, or in any way supplied the said drawings, specifications, or other data, is not to be regarded by implication or otherwise as in any manner licensing the holder or any other person or corporation, or conveying any rights or permission to manufacture, use, or sell any patented invention that may in any way be related thereto.

ACCESSION BY		
CPDT	WHITE SECTION	<input checked="" type="checkbox"/>
BSC	DDFF SECTION	<input type="checkbox"/>
UNANNOUNCED		<input type="checkbox"/>
JUSTIFICATION		
BY		
DISTRIBUTION/AVAILABILITY CODES		
REST.	AVAIL.	and or SPECIAL
/		

Copies of this report should not be returned to the Air Force Flight Dynamics Laboratory unless return is required by security considerations, contractual obligation, or notice on a specific document.

FOREWORD

This report was prepared by the Space Division, Aerospace Group of The Boeing Company, Seattle, Washington, under direction of Messrs. A. L. Nagel and V. Deriugin, program managers. The contract was initiated under BPSN 5(611366-62405334), Project 1366 Hypersonic Gas Dynamic Heating, Task 136607 Aerodynamics and Flight Mechanics, USAF Contract AF33(615)-2372, Investigation of Turbulent Heat Transfer at Hypersonic Speeds. The work was administered by the Air Force Flight Dynamics Laboratory, Air Force Systems Command, Wright-Patterson Air Force Base, Ohio. Mr. Richard D. Neumann (FDMG) was the Air Force project engineer.

Results obtained during this program are published in three volumes. Volume I, Analytical Methods; Volume II, Analysis of Heat Transfer and Pressure Data on a Flat Plate, Cone, Ogive, Cylindrical Leading Edge, Blunt Delta Wing, and X-15 Aircraft; and Volume III, The Laminar-Turbulent  $\rho r \mu_r$  Momentum Integral and Turbulent Nonsimilar Boundary Layer Computer Programs. Boeing document numbers assigned to these volumes are D2-113531-1, -2, and -3, respectively.

This report covers work conducted between March 1965 and March 1967. The report was submitted by the authors in May 1967.

The authors acknowledge Barbara J. Safley for her exceptional effort in generating and editing the figures contained in this report.

This technical report has been reviewed and is approved.

*Philip P. Antonatos*

---

PHILIP P. ANTONATOS  
Chief, Flight Mechanics Division  
Air Force Flight Dynamics Laboratory

## ABSTRACT

This report presents a combined analytical and experimental investigation of turbulent heat transfer on basic and composite configurations at hypersonic speeds. The analytical results are presented in Volume I, the experimental results, including data-theory comparisons, are presented in Volume II, and computer programs incorporating the analytical methods described herein are presented in Volume III.

Two analytical approaches are presented: the  $\rho_r \mu_r$  method and the turbulent nonsimilar boundary layer method.

The  $\rho_r \mu_r$  method, which is derived from the boundary-layer momentum and energy integral equations, is recommended for predicting turbulent heating rates. Effects of dissociation, pressure and wall temperature gradients, three-dimensional flow, and nose bluntness are included. Simplified methods for making turbulent heating estimates using a slide rule or desk calculator are also presented. The computation of heating rates on a typical reentry configuration in flight and the extrapolation of test data from ground test facilities to flight are described.

The turbulent nonsimilar boundary layer approach offers several advantages over previous methods, and is recommended for specific parametric studies of turbulent flows. Calculations made using this method have been restricted to ideal gases. Modifications can be made to include real-gas effects.

## TABLE OF CONTENTS

		Page
I	INTRODUCTION	1
	1. REQUIREMENT FOR HEAT TRANSFER PREDICTION METHODS	1
	2. PRESENT INVESTIGATION	1
	a. $\rho_r \mu_r$ Method	1
	b. Turbulent Nonsimilar Method	2
II	BASIC METHODS	4
	1. GENERAL APPROACHES	4
	a. Mixing Length Theory	4
	b. Integral Methods	5
	2. $\rho_r \mu_r$ METHOD	5
	a. Basic Formulation	5
	b. Evaluation of $C_x$ and $m$	7
III	COMPRESSIBILITY AND DISSOCIATION EFFECTS	11
	1. EVALUATION OF REFERENCE DENSITY-VISCOSITY PRODUCT	11
	2. REFERENCE STAGNATION VISCOSITY	16
	3. EVALUATION OF PRANDTL NUMBER AND LEWIS NUMBER PARAMETERS	16
IV	STREAMWISE PRESSURE GRADIENT EFFECTS	20
V	THREE-DIMENSIONAL EFFECTS	21
	1. GEOMETRIC EFFECTS— $r$ FACTOR	21
	2. CROSSFLOW PRESSURE GRADIENTS— $f$ FACTOR	22
	a. Evaluation of $\bar{E}_T$	23
	b. Evaluation of $f$	26
	3. SPECIAL CASES	28
	a. Swept Cylinder Stagnation Line	28
	b. Yawed Cone Stagnation Line	29
	c. Delta Wing Centerline	30
VI	NONISOTHERMAL WALL EFFECTS	33
VII	NOSE BLUNTNESS EFFECTS	37
	1. SHOCK ANGLE EFFECTS ON STANTON NUMBER	37
	2. MASS CONSERVATION ANALYSIS	39

TABLE OF CONTENTS (Concluded)

	Page
3. EVALUATION OF ( $\delta - \delta^*$ )	40
4. EVALUATION OF BLUNT BODY CONSTANT $C_B$	41
VIII APPLICATIONS	42
1. GEOMETRY AND TRAJECTORY	42
2. FLOW FIELD AND GAS PROPERTIES	42
a. Surface Pressures	43
b. Edge Velocities	44
c. Wall Temperatures	44
d. Streamline Divergence Parameters	45
e. Gas Model	45
3. BLUNTNES AND REAL GAS EFFECTS	46
4. EXTRAPOLATION TO FLIGHT	50
IX CONCLUDING REMARKS	55
APPENDIX A DERIVATION OF THE $\rho_r \mu_r$ METHOD	57
APPENDIX B SIMPLIFIED $\rho_r \mu_r$ METHOD	87
APPENDIX C TURBULENT NONSIMILAR METHOD	94
REFERENCES	116

## LIST OF ILLUSTRATIONS

Figure		Page
1.	Comparison of incompressible turbulent skin-friction formulas	9
2.	Reference density-viscosity product parameters	12
3.	Viscosity function for air in chemical equilibrium	13
4.	Heat transfer on a flat plate in a shock tunnel	14
5.	Turbulent heat transfer theory comparisons with X-15 flight test data	15
6.	Compressibility-temperature product for air in chemical equilibrium	17
7.	Partial Prandtl number for air	18
8.	Crossflow pressure gradient effect on cylinder stagnation-line turbulent heat transfer	25
9.	Streamline correlation for sharp delta wings	31
10.	Measured and theoretical turbulent heating rates with linear wall temperature gradient on a sharp cone	35
11.	Variation of heat transfer coefficient with shock angle on a blunt flat plate	38
12.	Nose bluntness effect on delta-wing centerline Stanton number	47
13.	Real-gas effect on delta-wing centerline Stanton number using normal-shock method	48
14.	Real-gas effect on delta-wing centerline Stanton number using blunt-body method	49
15.	Real-gas effect on reference Stanton number	51
16.	Real-gas effect on delta-wing centerline Stanton number ratios	52
17.	Stanton number ratios on the cylindrical leading edge of a 75°-swept blunt delta wing at $\sigma = 15^\circ$	53
18.	Turbulent extrapolation factors on a 75°-swept blunt delta wing	54
19.	Laminar Prandtl number effect on Reynolds analogy factor	71
20.	Diffusion effect on laminar heat transfer	72
21.	Correlation of reference density-viscosity product at $M = 0$	73
22.	Reference density-viscosity product for flows with pressure gradient	75
23.	Streamwise pressure gradient function $J_L$	80
24.	Real-gas correlation parameter for swept infinite cylinders	81

## LIST OF ILLUSTRATIONS (Concluded)

Figure		Page
25.	Crossflow correlations for yawed cone flow	82
26.	Streamwise pressure gradient effect on skin friction	83
27.	Turbulent crossflow momentum thickness ratio	89
28.	Stanton numbers from simplified and complete $\rho_r \mu_r$ equations	92
29.	Comparisons of turbulent velocity profiles for incompressible flow on a flat plate	102
30.	Comparisons of turbulent skin friction coefficients for incompressible flow on a flat plate	104
31.	Mach number effect on turbulent skin friction for adiabatic flow on a flat plate	105
32.	Combined effects of Mach number and wall cooling on turbulent skin friction on a flat plate	107
33.	Turbulent Prandtl number effect on recovery factor	108
34.	Turbulent heating distribution on a hemisphere	110
35.	Effect of $\Delta y$ on predicted skin-friction coefficients	112
36.	Numerical stability criteria for nonsimilar boundary layer program	115

## SYMBOLS

a, b, c	constants in turbulent-shear correlation, Equation (C-37)
A	boundary-layer thickness parameter, $2 + (\delta^*/\theta)$
ALT	altitude
$h_{eq}$	equivalent distance in the absence of streamwise pressure gradients, Equation (A-65)
$c_p$	specific heat at constant pressure
$c_v$	specific heat at constant volume
C	coefficient; constant
$C_B$	constant in blunt-body correlation, Equation (74)
$C_D$	drag coefficient, $D/[(1/2) (\rho_\infty u_\infty^2) S]$
$C_f$	skin-friction coefficient, $\tau_w/[(1/2) (\rho u^2)]$
$C_L$	lift coefficient, $L/[(1/2) (\rho_\infty u_\infty^2) S]$
$C_m$	constant in boundary-layer shear law, Equation (4)
$C_P$	pressure coefficient, $(P - P_\infty)/[(1/2) (\rho_\infty u_\infty^2)]$
$C_Q$	constant in boundary-layer heat-transfer law, Equation (3)
$C_x$	constant in boundary-layer shear law, Equation (5)
d	constant in compressible shear correlation, Equation (C-39)
D	nose diameter; leading-edge diameter; drag force
E	crossflow momentum thickness, Equation (A-25)
$\bar{E}$	momentum thickness ratio, $E/\theta$
f	streamline divergence due to crossflow pressure gradients, Equation (A-10)
F	function of x, Equation (A-12)

SYMBOLS (Continued)

$\bar{F}_{Pr}$	Prandtl number function, Equation (A-23)
$F_x$	equivalent distance function, Equations (A-63) and (A-64)
$F_\beta$	function of pressure gradient parameter $\beta$ , Equation (A-50)
$F_\Sigma$	function of density parameter, Equation (A-52)
$g$	scale factor on $y$ , see Appendix A
$G$	boundary-layer parameter, Equations (60) and (A-47)
$h$	height of reference streamline above surface, Equation (63)
$H$	heat-transfer coefficient based on enthalpy, $\dot{q}/(i_{aw} - i_w)$
$\bar{H}$	transformed heat-transfer coefficient, Equation (A-12)
$i$	static enthalpy
$i_D$	energy absorbed in dissociation
$I$	total enthalpy, $i + (u^2/2)$
$J$	streamwise pressure-gradient parameter, Equation (A-24)
$k$	thermal conductivity
$l$	mixing length, Equation (1)
$\mathcal{L}$	diffusion influence parameter, $\dot{q}/\dot{q}_{N_{Le} = 1}$ , Equation (A-22)
$m$	exponent on boundary-layer shear and heat-transfer laws, Equations (3) and (4)
$\dot{m}$	mass flow rate
$M$	Mach number
$M_n$	Mach number component normal to surface, Equation (52)
$N_{Le}$	Lewis number
$N_{Nu}$	reference Nusselt number, see Figure 3

SYMBOLS (Continued)

$N_{Pr}$	Prandtl number
$N_R$	Reynolds number
$N_{St}$	Stanton number, $\dot{q}/[(i_{aw} - i_w)(\rho_\infty u_\infty)]$
$\bar{N}_{CL}$	streamline divergence parameter, Equation (52)
$P$	pressure: streamwise pressure-gradient parameter, Equation (A-33)
$\bar{P}$	dimensionless pressure, $P/(\rho_e u_e^2)$
$\dot{q}$	heat-transfer rate
$Q$	boundary-layer energy thickness, Equation (A-8)
$\bar{Q}$	transformed boundary-layer energy thickness, Equation (A-13)
$r$	streamline divergence due to body geometry; recovery factor, Equation (C-40)
$R$	gas constant in equation of state
$R_n$	nose radius
$R'$	effective shock radius of curvature, Equation (66)
$S$	surface distance measured from stagnation point along centerline
$S_{eq}$	skin-friction equivalent distance, Equation (9)
$T$	temperature
$u$	velocity component in x-direction
$U$	transformed x-component of velocity, Equation (A-12)
$v$	velocity component in y-direction
$\bar{v}$	velocity ratio, $v/u$
$\tilde{v}$	effective velocity, Equation (C-4)
$V$	transformed y-component of velocity, Equation (A-12)

SYMBOLS (Continued)

w	velocity component in z-direction
x	streamwise coordinate along body surface; surface distance
x, y, z	curvilinear coordinates
$x_{eq}$	heat-transfer equivalent distance, Equation (8)
$x'$	distance from nose to heated surface, see Figure 7
X, Y, Z	transformed x, y, z coordinates, Equation (A-12)
Z	compressibility factor, $P/(\rho RT)$
$\alpha$	angle of attack
$\alpha_n$	effective angle of attack at stagnation line, $(90^\circ - \Lambda_{eff})$
$\beta$	pressure gradient parameter, Equation (A-51); wing apex angle, $(90^\circ - \Lambda)$ . Equation (52)
$\gamma$	ratio of specific heats, $c_p/c_v$
$\delta$	boundary-layer thickness; angle between free-stream velocity vector and local tangent plane
$\delta^*$	boundary-layer displacement thickness
$\bar{\delta}$	transformed boundary-layer thickness, Equation (A-10)
$\Delta$	total streamline divergence, rf; streamtube width at the boundary-layer edge
$\Delta x, \Delta y$	increments in x and y
$\epsilon$	crossflow energy thickness, Equation (A-9); velocity perturbation, Equation (C-46); shock angle with respect to free-stream velocity vector; effective turbulent viscosity
$\bar{\epsilon}$	energy thickness ratio, $\epsilon/Q$
$\xi$	dummy variable in x, Equation (57)
$\eta$	cone half-angle

### SYMBOLS (Continued)

$\theta$	boundary-layer momentum thickness
$\Theta$	transformed boundary-layer momentum thickness, Equation (A-28)
$\Lambda$	sweep angle
$\mu$	absolute viscosity
$\xi$	shock standoff angle
$\rho$	density
$\sigma$	partial Prandtl number for translation, rotation, and vibration only
$\Sigma$	mean density ratio, Equations (A-53) and (A-57)
$\tau$	shear stress
$\bar{\tau}$	transformed shear stress
$\tau_T$	Reynolds stress
$\phi$	surface angle measured from stagnation point or stagnation line
$\phi^{**}$	streamline correlation function, Equation (52)
$\Phi$	thermal potential parameter, Equation (54)
$\psi$	streamtube angle at stagnation point, Equation (63)
$\propto$	is proportional to

#### Subscripts

aw	adiabatic wall
BL	boundary layer
c	crossflow
CL	centerline
e	boundary-layer edge
eff	effective

SYMBOLS (Continued)

FLT	flight
i, j	indexes
inc	incompressible
L	laminar
m	matching point; mean
n	normal; nose
ns	neutral stability
NS	evaluated for entropy level behind a normal shock
o	evaluated at stagnation reference conditions; evaluated for $M_e = 0$ , Equation (29); evaluated at $x = 0$ , see Section VI
P	pressure
Q	evaluated for $x_{eq}$
r	evaluated at enthalpy and composition corresponding to $\rho_r \mu_r$
ref	reference
s	streamwise
S	stagnation; evaluated for $S_{eq}$
Sh	evaluated for a sharp nose
SL	stagnation line
S'	evaluated at stagnation enthalpy and local pressure
T	turbulent
TNS	turbulent nonsimilar method
TP	tangent point
w	wall

## SYMBOLS (Concluded)

WT	wind tunnel
x	based on distance x
2-D	two-dimensional flow
3-D	three-dimensional flow
$\infty$	free-stream or undisturbed condition

### Superscript

n	exponent in Equation (52)
- (bar)	normalized value

## SECTION I

### INTRODUCTION

#### 1. REQUIREMENT FOR HEAT TRANSFER PREDICTION METHODS

The need for better methods for estimating aerodynamic heating rates is continually increasing. Relatively crude approximations have usually been adequate for estimating surface temperatures on supersonic aircraft and ablation protection requirements for ballistic reentry capsules. However, the design and operating limits of hypersonic cruise and maneuverable reentry vehicles of the future will be more sensitive to aerodynamic heating considerations. This will require more accurate heat transfer prediction methods.

The prediction of turbulent heating presents a particularly serious problem for two reasons. First, turbulent heating rates are usually much higher than the corresponding laminar values. Since the conditions required for transition from laminar to turbulent flow cannot yet be predicted with confidence, design estimates in regions of uncertainty must be based on the higher turbulent estimates. Secondly, the complexity of turbulent flows necessitates the use of simplifying approximations and empiricism in formulating the fundamental flow equations; thus, methods for predicting turbulent heating rates are inherently less reliable than laminar methods.

#### 2. PRESENT INVESTIGATION

A two-year investigation, including both analytical and experimental studies, was conducted to provide and verify methods for predicting turbulent heating rates on basic shapes and composite bodies at hypersonic speeds. Results of the analytical studies, including recommended methods, are presented in Volume I of this report. Experimental results and data-theory comparisons are presented in Volume II.

Two basic methods are presented. The first, the  $\rho_r \mu_r$  program, is recommended for making turbulent heating estimates. The second, the turbulent nonsimilar program, represents a new approach in treating turbulent flows, and is intended for basic studies of turbulent boundary layer phenomena. Both have been programmed for the SRU 1108 and IBM 7094 digital computers. A description of these computer programs is given in Volume III of this report.

##### a. $\rho_r \mu_r$ Method

The  $\rho_r \mu_r$  method for predicting heat transfer and skin friction for both laminar and turbulent flows was developed by Richard A. Hanks of The Boeing Company in the course of the X-20 program. Modifications and refinements of this method were made under a subsequent NASA contract (Reference 1). The method presented here is

essentially the same as that presented in Reference 1, although some modifications to the computer program were made during the present study.

The derivations of the basic  $\rho_r \mu_r$  equations presented in References 1 and 2 were based on solutions of the boundary-layer momentum integral equation. This equation was transformed into an equivalent incompressible form using a coordinate transformation suggested by Mager in Reference 3. The transformed equation was solved to obtain an expression for skin friction. The corresponding heat transfer equation was then obtained using a generalized form of the Reynolds analogy.

A new derivation leading to the same result for heat transfer, but based on a solution to the transformed boundary-layer energy integral equation, is presented in Appendix A. The heat transfer equation obtained from the solution of the energy integral contains boundary-layer thickness parameters and reference density and viscosity terms as undefined functions. These functions represent effects of fluid property variations, finite streamwise and crossflow pressure gradients, and stream-line divergence. For laminar flow, these functions were evaluated by exact solutions for self-similar boundary layers. Analytic expressions were found that agree with essentially all of the exact similar solutions.

The derivation of the basic  $\rho_r \mu_r$  heat transfer equation and the correlations used in defining the undefined functions for laminar flow are presented in Appendix A. Expressions for evaluating the turbulent functions are presented in the following sections.

Because of the overall complexity of the  $\rho_r \mu_r$  equations, this method is not recommended for making hand calculations. Handbook methods for estimating both laminar and turbulent heating rates using the  $\rho_r \mu_r$  method are presented in References 4 and 5.<sup>1</sup> Simplified approximations to the  $\rho_r \mu_r$  equations permitting hand calculations are presented in Appendix B of this report. Predictions obtained using the simplified equations are usually within 5% of the computer results.

#### b. Turbulent Nonsimilar Method

The turbulent nonsimilar method is an extension of the laminar nonsimilar method reported in References 1 and 6. In this method a semi-empirical expression is used to establish the Reynolds stress term appearing in the momentum equation. The corresponding conduction term in the energy equation is then related to the Reynolds stress by an effective turbulent Prandtl number.

The turbulent nonsimilar method for flows was developed before the present study was started. During this investigation it was extended to include compressibility effects.

---

1 Reference 4 supplements Reference 5. Except for delta wings at angle of attack, turbulent heating estimates obtained from these reports are nearly identical.

The analysis was conducted to provide a method for computing velocity and enthalpy profiles in a compressible turbulent boundary layer including the effects of pressure and wall temperature gradients.

The derivation of the turbulent nonsimilar equations is presented in Appendix C of this report.

## SECTION II

### BASIC METHODS

In contrast to the well-developed theoretical methods available for laminar flows, no truly analytic basis exists for treating turbulent boundary layers. The unsteady velocity fluctuations greatly complicate the mathematical description; consequently, all turbulent methods are founded, at least in part, on empirical correlations.

#### 1. GENERAL APPROACHES

Most turbulent analyses are based on the assumption that turbulent flows are analogous to laminar flows with special viscous and heat conduction properties. These special properties can be expressed in either the fundamental equations of motion in differential form or in the boundary layer momentum and energy integral equations. An example of the first type is furnished by the well-known mixing length theory.

##### a. Mixing Length Theory

For incompressible flow, Prandtl hypothesized that:

$$\tau_T = \rho \ell^2 \left| \frac{\partial u}{\partial y} \right| \frac{\partial u}{\partial y} \quad (1)$$

The mixing length is denoted by  $\ell$ . Prandtl further suggested that  $\ell$  was nearly proportional to the distance from the wall. Equation (1), using the approximation that  $\ell$  is proportion to  $y$ , was found to provide good incompressible skin-friction estimates and velocity profiles when the shear was assumed to be constant with  $y$  (Reference 7). This latter assumption is clearly unrealistic for exterior boundary layers, since the Reynolds stress must approach zero at the edge of the boundary layer.

Many other methods using mixing length theory have been reported, including a widely used method for compressible flows developed by van Driest (Reference 8). However, most of these methods are based on assumed velocity or shear profiles. In addition, restrictive assumptions regarding flow similarity have been required in order to solve the flow equations, thus limiting these analyses to flows with no pressure or wall temperature gradients. Fewer assumptions are required by the turbulent non-similar method, which is described in Appendix C. The method utilizes a shear correlation similar to the mixing length correlation given by Equation (1), but removes many of the restrictions imposed by previous analyses. By solving the boundary-layer conservation equations in partial differential form, velocity and temperature profiles are then obtained as part of the solution. No limitations are imposed regarding pressure or wall temperature gradients except that separated flows cannot be treated.

b. Integral Methods

Boundary layer methods derived from momentum and energy integral equations are often much easier to use than methods requiring the exact solution of the flow equations. The energy integral equation, Eq. (A-9), derived in Appendix A of this report and the momentum integral equation derived in Appendix B of Reference 2 can be expressed in the forms given below:

$$\frac{H}{\rho_e u_e} = \frac{\partial Q}{\partial x} + Q \left[ \frac{1}{u_e} \frac{\partial u_e}{\partial x} + \frac{1}{\rho_e} \frac{\partial \rho_e}{\partial x} + \frac{1}{r} \frac{\partial r}{\partial x} + \frac{\bar{E}}{f} \frac{\partial f}{\partial x} \right]$$

$$\frac{\tau_w}{\rho_e u_e^2} = \frac{\partial \theta}{\partial x} + \theta \left[ \frac{(2+\delta^*/\theta)}{u_e} \frac{\partial u_e}{\partial x} + \frac{1}{\rho_e} \frac{\partial \rho_e}{\partial x} + \frac{1}{r} \frac{\partial r}{\partial x} + \frac{\bar{E}}{f} \frac{\partial f}{\partial x} \right] \quad (2)$$

The equations given above are exact, except for the usual boundary layer assumptions, and are valid for both laminar and turbulent flows. However, the solutions to Equation (2) are quite different for laminar and turbulent flows, since the velocity and enthalpy profile parameters used in solving the equations are different.

2.  $\rho_r \mu_r$  METHOD

a. Basic Formulation

The  $\rho_r \mu_r$  equations are derived in Appendix A from the boundary layer energy and momentum integral equations. The basic correlations are of Blasius type, and are given by:

$$H_T = \frac{\rho_r \mu_r u_e}{\mu_o} \frac{C_Q}{\left[ \frac{\rho_e u_e Q}{\mu_o} \right]^{1/m}} \quad (3)$$

$$\frac{\tau_{w,T}}{u_e} = \frac{\rho_r \mu_r u_e}{\mu_o} \frac{C_m}{\left[ \frac{\rho_e u_e \theta}{\mu_o} \right]^{1/m}} \quad (4)$$

The symbols  $m$ ,  $C_m$ , and  $C_Q$  are profile parameters,  $\theta$  is the momentum thickness, and  $Q$  is the energy thickness. Momentum and energy thicknesses are defined in Appendix A, as are methods for evaluating the reference density-viscosity product  $\rho_r \mu_r$ .

The integral equations are reduced to an incompressible form using a modified Stewartson transformation and are given in detail in Appendix A. The resulting equations, in physical coordinates, for  $H$ ,  $\tau_w/u_e$ , and  $\theta$  are:

$$H = \frac{C_x \mathcal{L} \mu_o}{F_{Pr} x_{eq}} \left[ \frac{\rho_r \mu_r u_e x_{eq}}{\mu_o^2} \right]^{\frac{m}{m+1}} \quad (5)$$

$$\frac{\tau_w}{u_e} = \frac{C_x \mu_o}{S_{eq}} \left[ \frac{\rho_r \mu_r u_e S_{eq}}{\mu_o^2} \right]^{\frac{m}{m+1}} \quad (6)$$

$$\theta = \frac{m-1}{m} C_x \frac{\mu_o}{\rho_e u_e} \left[ \frac{\rho_r \mu_r u_e S_{eq}}{\mu_o^2} \right]^{\frac{m}{m+1}} \quad (7)$$

where the equivalent distance parameters  $x_{eq}$ , and  $S_{eq}$  are defined by:

$$x_{eq,T} = \frac{1}{\left[ J_T \rho_r \mu_r u_e (rf\bar{E})^{\frac{m+1}{m}} \right]_{x_1}} \int_0^{x_1} \rho_r \mu_r u_e (rf\bar{E})^{\frac{m+1}{m}} dx \quad (8)$$

$$S_{eq,T} = \frac{1}{\left[ P_T \rho_r \mu_r u_e^A (rf\bar{E})^{\frac{m+1}{m}} \right]_{x_1}} \int_0^{x_1} \rho_r \mu_r u_e (rf\bar{E})^{\frac{m+1}{m}} dx \quad (9)$$

The equivalent distance  $x_{eq, T}$  is used only in computing heat transfer, and  $S_{eq, T}$  only in computing skin-friction and momentum thickness.

Methods for evaluating the terms appearing in Equations (5) through (9) for laminar flow are given in Appendix A. Expressions for evaluating the equations given in the following sections reflect the latest state-of-the-art, and are essentially the same as reported in References 1 and 4.

For turbulent flow, the profile constants  $C_x$  and  $m$  are discussed later in this section. Methods for evaluating the other parameters are presented in the following sections.

<u>Symbol</u>	<u>Definition</u>	<u>Section</u>
$\rho_r \mu_r$	reference density-viscosity product	III
$\mu_0$	reference stagnation viscosity	III
$F_{Pr}$	influence of Prandtl number on heat transfer, $\dot{q}/\dot{q}_{\sigma=1}$	III
$\mathcal{L}$	influence of atomic diffusion on heat transfer, $\dot{q}/\dot{q}_N$ , $Le = 1$	III
$J$	profile parameter reflecting pressure gradient effects on heat transfer	IV
$P$	profile parameter reflecting pressure gradient effects on wall shear stress	IV
$r$	streamline divergence parameter due to body geometry	V
$f$	streamline divergence parameter due to crossflow pressure gradients	V
$\bar{E}$	crossflow momentum thickness	V

b. Evaluation of  $C_x$  and  $m$

The profile parameters  $C_x$  and  $m$  are by definition; as in the laminar case, independent of pressure gradients and flow compressibility; hence, these parameters can be evaluated on the basis of incompressible flat-plate flow. For this case  $\rho_r \mu_r = \rho_e \mu_e$ ,  $\mu_0 = \mu_e$ , and  $x_{eq} = S_{eq} = x$ ; thus, Equations (5) and (6) simplify to:

$$H = \frac{C_x \mu_e}{F_{Pr} x} \left[ N_{R,e} \right]^{\frac{m}{m+1}} \quad (10)$$

$$C_f = z C_x \frac{\mu_e}{x} \left[ N_{R,e} \right]^{\frac{1}{m-1}} \quad (11)$$

When  $C_x = .0296$  and  $m = 4$ , Equation (10) corresponds to the Colburn equation, and Equation (11) becomes the familiar Blasius expression. No heat transfer data are available for comparative purposes, since the very low heating rates associated with nearly incompressible gas flows cannot be accurately measured. Comparisons with skin friction data show that  $C_x$  and  $m$  are themselves functions of the Reynolds number. To include this variation with Reynolds numbers would greatly complicate computations; hence, an alternate formulation for the skin friction expression was sought.

After a survey of several proposed incompressible friction formulas, a minor modification of the Schultz-Grunow equation (Reference 9) was selected:

$$C_f = \frac{.37}{\left[ \log_{10} (N_{R,e} - 3000) \right]^{2.584}} \quad (12)$$

The modification is the addition of the constant 3000 to the Reynolds number. This modification was made in order to provide more realistic values of  $C_f$  at Reynolds numbers below  $10^4$  (see Figure 1).

The modified and unmodified expressions are shown in Figure 1, together with other available methods. As shown, there is little difference between the various methods, except that the Blasius equation falls low at high values of Reynolds number. Equation (12) was originally selected because of its slight conservatism, although any of the other expressions could have been used.

The form of Equation (12) does not lend itself to calculations in the framework of Equations (10) and (11) due to the variation of  $m$  with Reynolds number. However, comparisons have been made that show that  $m = 4$  is an adequate approximation for evaluating geometric effects. For example, if  $m$  is evaluated at particular values of Reynolds number using Equation (12) the following comparisons are obtained:

$N_{R,e}$	$m = \frac{1}{1 - \frac{d(\ln C_f)}{d(\ln N_{R,e})}}$	$\frac{H_{\text{cone}}}{H_{\text{flat plate}}}$	$\frac{H_{\text{cylinder}}}{H_{\text{cylinder}, m=4.0}}$
$10^5$	3.45	1.20	.99
$4.2 \times 10^5$	4.0	1.17	1.00
$10^6$	4.34	1.16	1.00
$10^8$	6.12	1.11	1.01

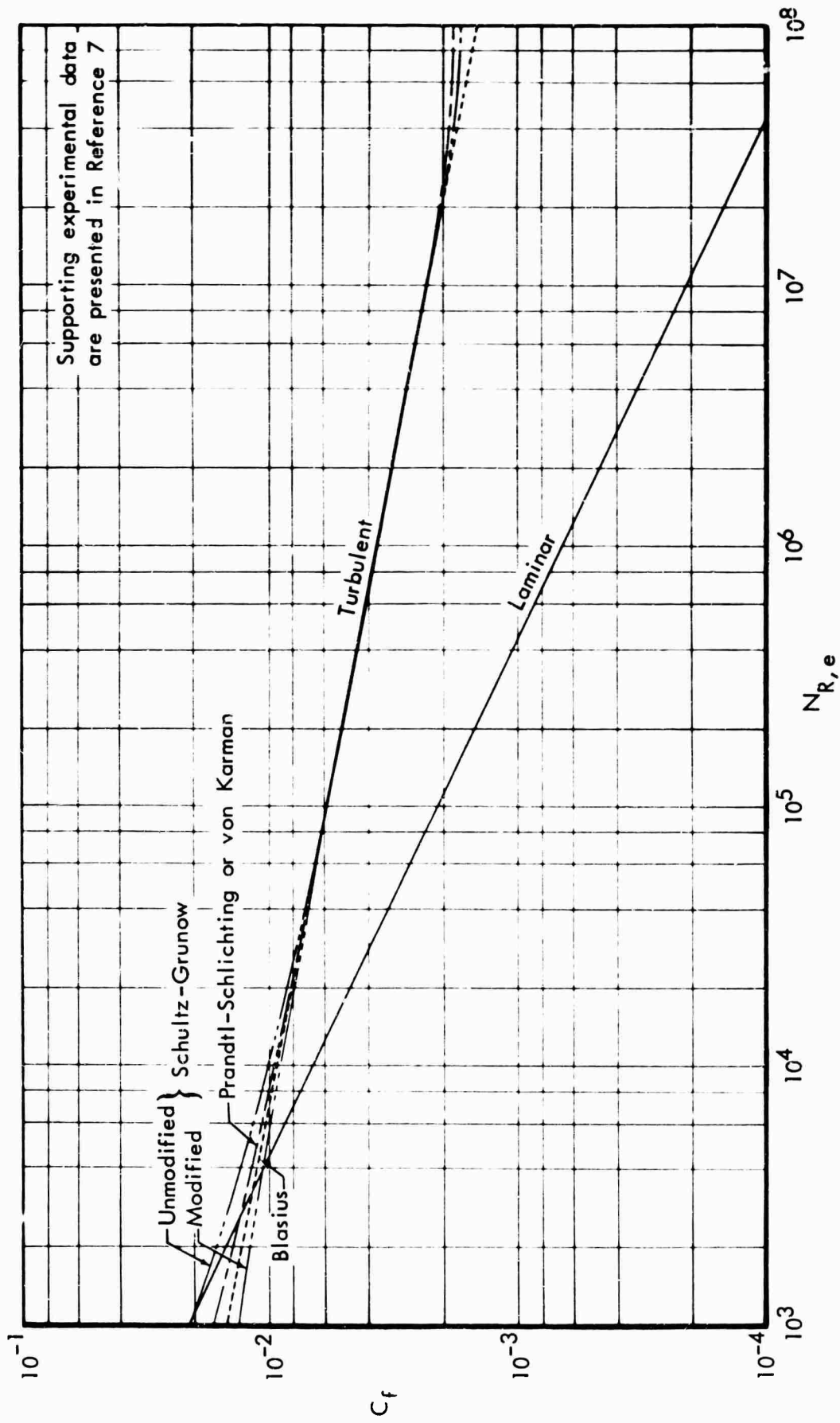


Figure 1: COMPARISON OF INCOMPRESSIBLE TURBULENT SKIN-FRICTION FORMULAS

Thus the effect of variations in  $m$  is seen to be small. Accordingly,  $m = 4.0$  was selected for calculation of geometric effects presented in Sections III, IV, and V.

However, since sizeable errors can result from using  $m = 4$  in Equations (5) and (6), the basic form of Equation (12) has been adopted. The new expressions replacing Equations (5) and (6) are:

$$H_T = \frac{.185 \mathcal{L} \mu_o}{F_{Pr} x_{eq,T}} \frac{N_{R,r,Q}}{\left[ \log_{10} (N_{R,r,Q} + 3000) \right]^{2.584}} \quad (13)$$

$$\frac{\tau_{w,T}}{u_e} = \frac{.185 \mu_o}{S_{eq,T}} \frac{N_{R,r,S}}{\left[ \log_{10} (N_{R,r,S} + 3000) \right]^{2.584}} \quad (14)$$

where

$$N_{R,r,Q} = \frac{\rho_r \mu_r u_e x_{eq,T}}{\mu_o} \quad (15)$$

and

$$N_{R,r,S} = \frac{\rho_r \mu_r u_e S_{eq,T}}{\mu_o} \quad (16)$$

The definitions of  $x_{eq,T}$  and  $S_{eq,T}$  are given by Equations (8) and (9), respectively.

The Schultz-Grunow expression for momentum thickness of an incompressible flat-plate boundary layer is given in Reference 9 by:

$$\theta = .2135 \frac{x}{\left[ \log_{10} N_{R,e} - .407 \right]^{2.64}} \quad (17)$$

The equivalent  $\rho_r \mu_r$  expression is:

$$\theta = .2135 \frac{\mu_o}{\rho_e u_e} \frac{N_{R,r,S}}{\left[ \log_{10} N_{R,r,S} - .407 \right]^{2.64}} \quad (18)$$

## SECTION III

### COMPRESSIBILITY AND DISSOCIATION EFFECTS

The influence of compressibility and dissociation effects on heat transfer and skin friction is usually accounted for by basing the density and transport properties (i. e. , coefficients of conductivity and viscosity) on some reference thermal parameter. For example, reference temperatures (or enthalpies) based on a weighted average of the wall, adiabatic wall, and boundary layer edge temperatures (or enthalpies) are commonly used as a thermal reference. The  $\rho_r \mu_r$  method differs from the common reference temperature methods in two respects. First, a reference density-viscosity product  $\rho_r \mu_r$  is evaluated instead of a reference temperature and secondly, a reference stagnation viscosity  $\mu_0$  must be evaluated. Other correction terms appearing in Equation (13) reflecting effects of compressibility and dissociation are expressed by the Prandtl number function  $F_{Pr}$  and the Lewis number function  $\mathcal{L}$ .

#### 1. EVALUATION OF REFERENCE DENSITY-VISCOSITY PRODUCT

The reference density-viscosity product for turbulent flow is taken to be the laminar value defined by Equation (A-42) in Appendix A and plotted in Figure 2 (for air in chemical equilibrium, the density-viscosity ratios required to obtain  $\rho_r \mu_r$  can be obtained from Figure 3). This basic identity is suggested by the fact that  $\rho_r \mu_r$  appears only in connection with the laminar shear terms of the turbulent boundary layer equations<sup>2</sup>. Further justification is provided by the excellent agreement between estimates from the  $\rho_r \mu_r$  method and most experimental data obtained from several facilities covering a wide range of test conditions.

Comparisons of  $\rho_r \mu_r$  predictions with flat plate heat transfer data obtained from the Cornell Aeronautical Laboratory (CAL) 48" shock tunnel and reported in Reference 1 are shown in Figure 4. The  $\rho_r \mu_r$  correlations given by Equation (A-42) provide good agreement with X-15 flight data as shown in Figure 5. The X-15 comparisons are especially noteworthy because of the lack of agreement with other widely used methods. These comparisons demonstrate good agreement between theoretical predictions and experimental measurements. More recent flat plate data obtained from the CAL shock tunnels and reported in Reference 10 are shown in Volume II of this report to be substantially higher than the  $\rho_r \mu_r$  estimates. The reason for the discrepancy between the two sets of data is not fully understood at this time. Some of the possible causes are discussed in Volume II.

---

2 E. g. , Equation (13) in Reference 3.

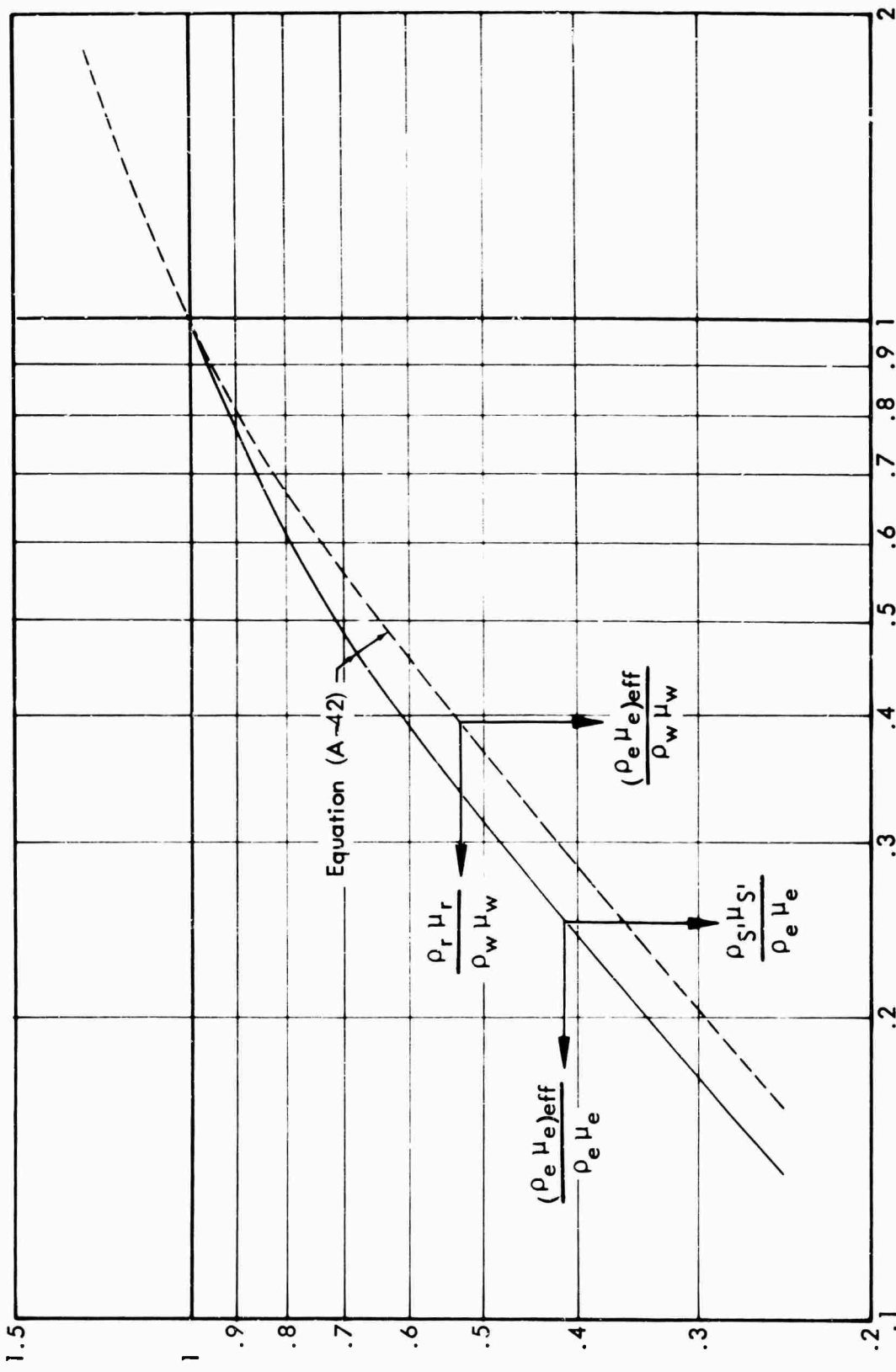


Figure 2: REFERENCE DENSITY-VISCOSITY PRODUCT PARAMETERS

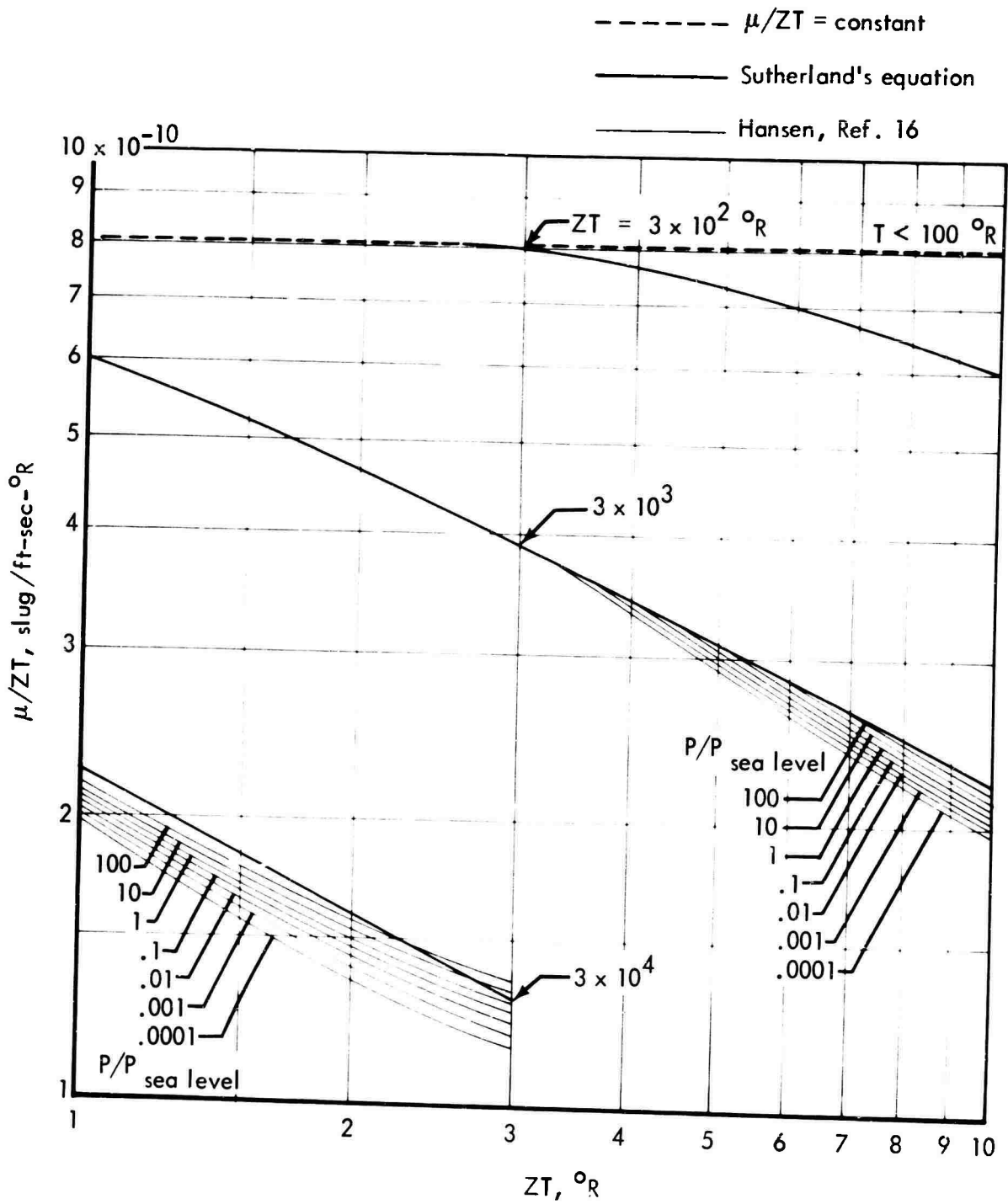


Figure 3: VISCOSITY FUNCTION FOR AIR IN CHEMICAL EQUILIBRIUM

	$T_S, ^\circ R$	$M_e$	$i_w/l_e$	Leading edge	} $M_\infty \approx 6.5$ $\alpha = 15^\circ$
○	2130	4.1	0.240	Sharp	
□	4310	3.8	0.112	Sharp	
△	2150	2.0	0.240	Blunt	

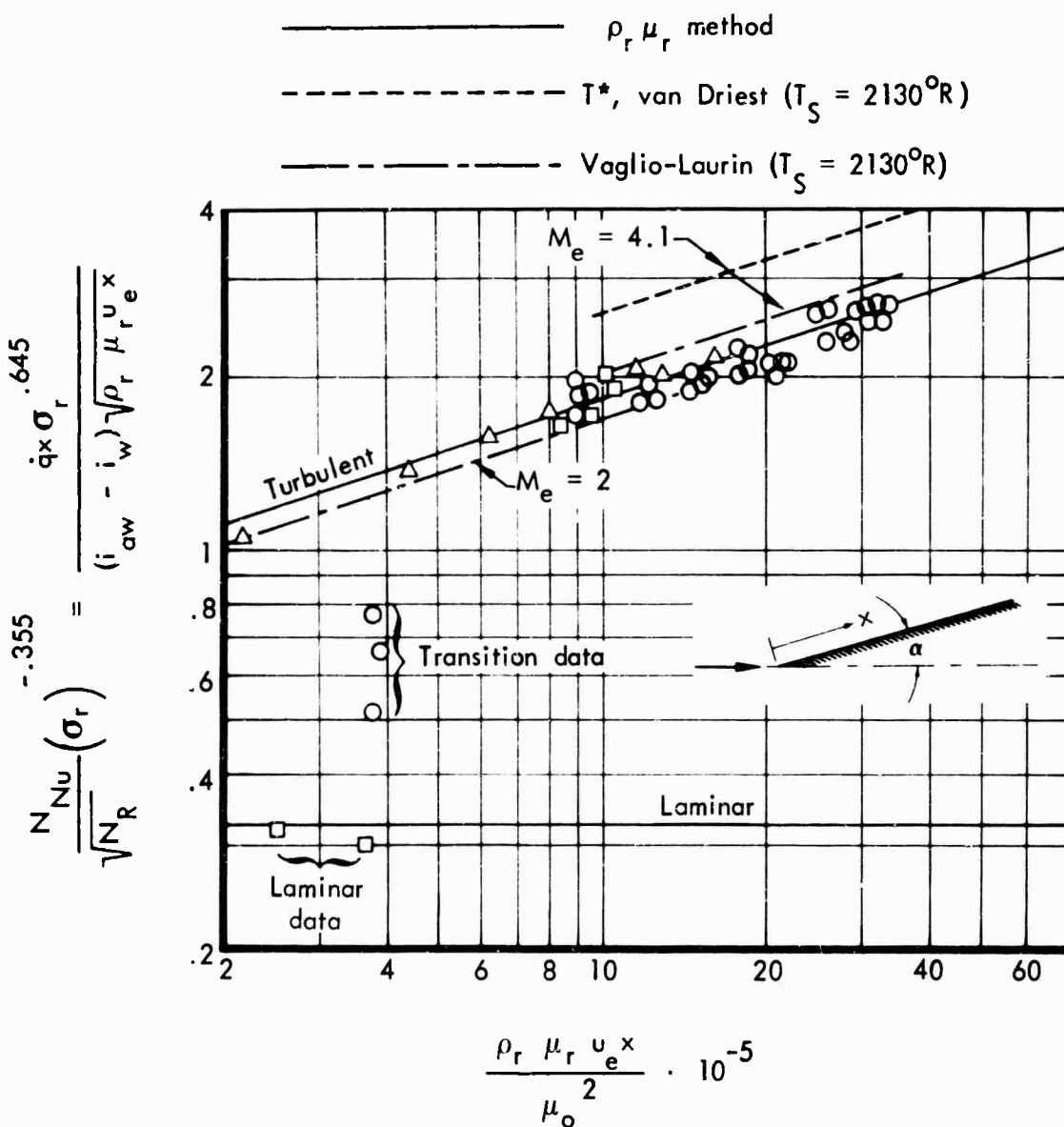
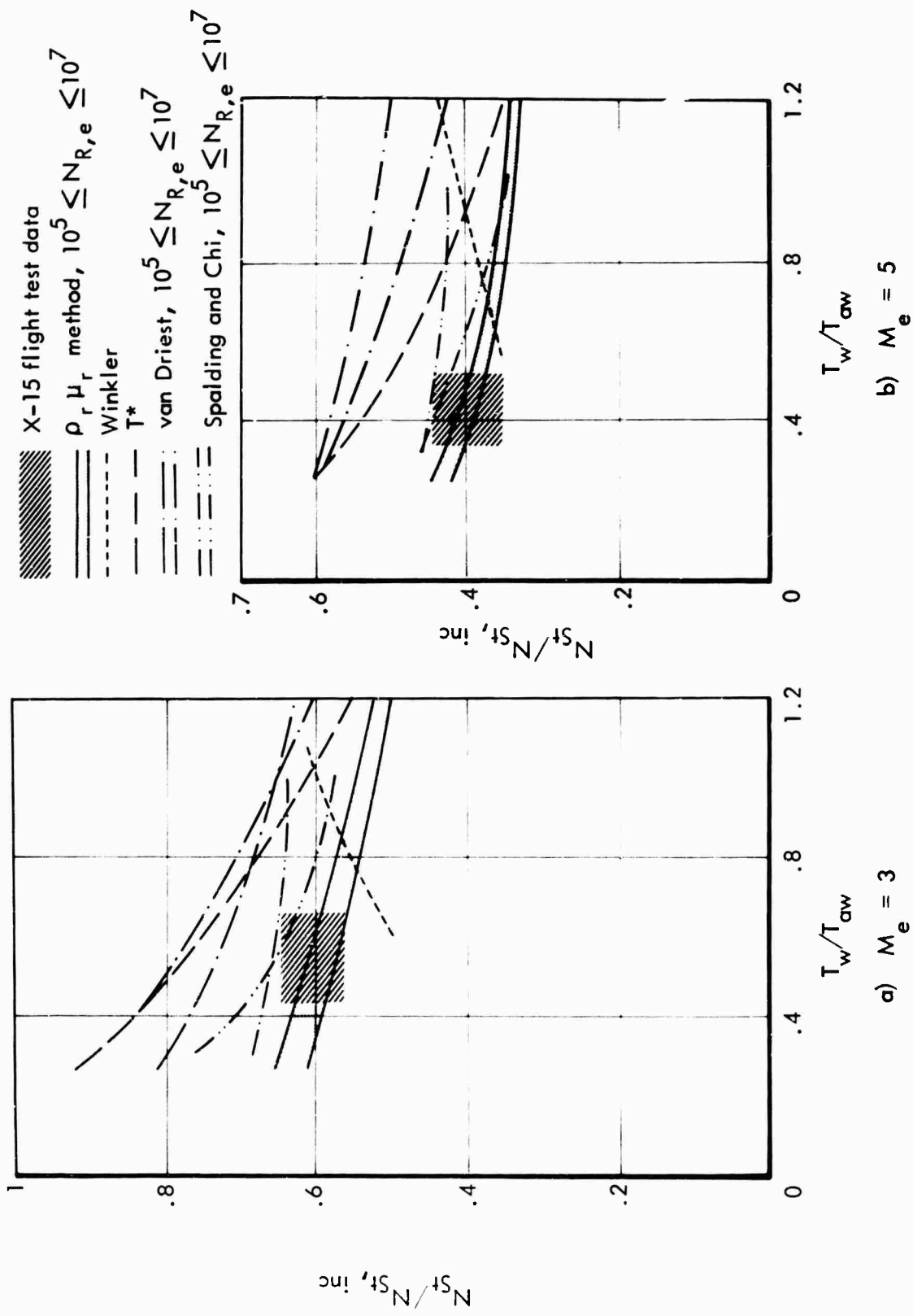


Figure 4: HEAT TRANSFER ON A FLAT PLATE IN A SHOCK TUNNEL



5

## 2. REFERENCE STAGNATION VISCOSITY

Since the reference stagnation viscosity does not appear in the laminar equations, no information regarding its evaluation can be obtained by examining the laminar solutions. The reference stagnation viscosity is assumed by Mager (Reference 3) to be the viscosity evaluated at stagnation conditions. For real-gas flow with the viscosity dependent on the pressure it seems more realistic to consider the local flow composition rather than the composition corresponding to stagnation conditions. Accordingly,  $\mu_0$  is calculated with the Sutherland law and  $\mu_r$  using the value of specific heat corresponding to  $\rho_r \mu_r$ . The result is:

$$\mu_0 = \mu_r \left( \frac{i_e}{i_r} \right)^{\frac{3}{2}} \frac{[(ZT)_r + 200]}{\left[ (ZT)_r \left( \frac{i_e}{i_r} \right) + 200 \right]} \quad (19)$$

When  $\rho_r \mu_r$  and local pressure are known, the compressibility-temperature product ZT can be obtained for air in chemical equilibrium from Figure 3. The corresponding reference enthalpy  $i_r$  can then be determined using Figure 6.

## 3. EVALUATION OF PRANDTL NUMBER AND LEWIS NUMBER PARAMETERS

As with the  $\rho_r \mu_r$  correlations, the effects of Prandtl number on turbulent flat plate heat transfer are assumed to be identical to the laminar case, the correction term is:

$$F_{Pr} = \sigma_r^{.645} \quad (20)$$

Where  $\sigma$  is the partial Prandtl number for translation, rotation, and vibration. The subscript r denotes that  $\sigma$  is evaluated at the enthalpy and composition corresponding to  $\rho_r \mu_r$ . For equilibrium air,  $\sigma$  can be obtained from Figure 7.

Similarly, no analytic basis has been found for determining the influence of atomic diffusion on turbulent heating rates. Furthermore, the combination of high pressures and temperatures required to obtain significant dissociation of air in turbulent boundary layers cannot be obtained in most present-day ground test facilities.

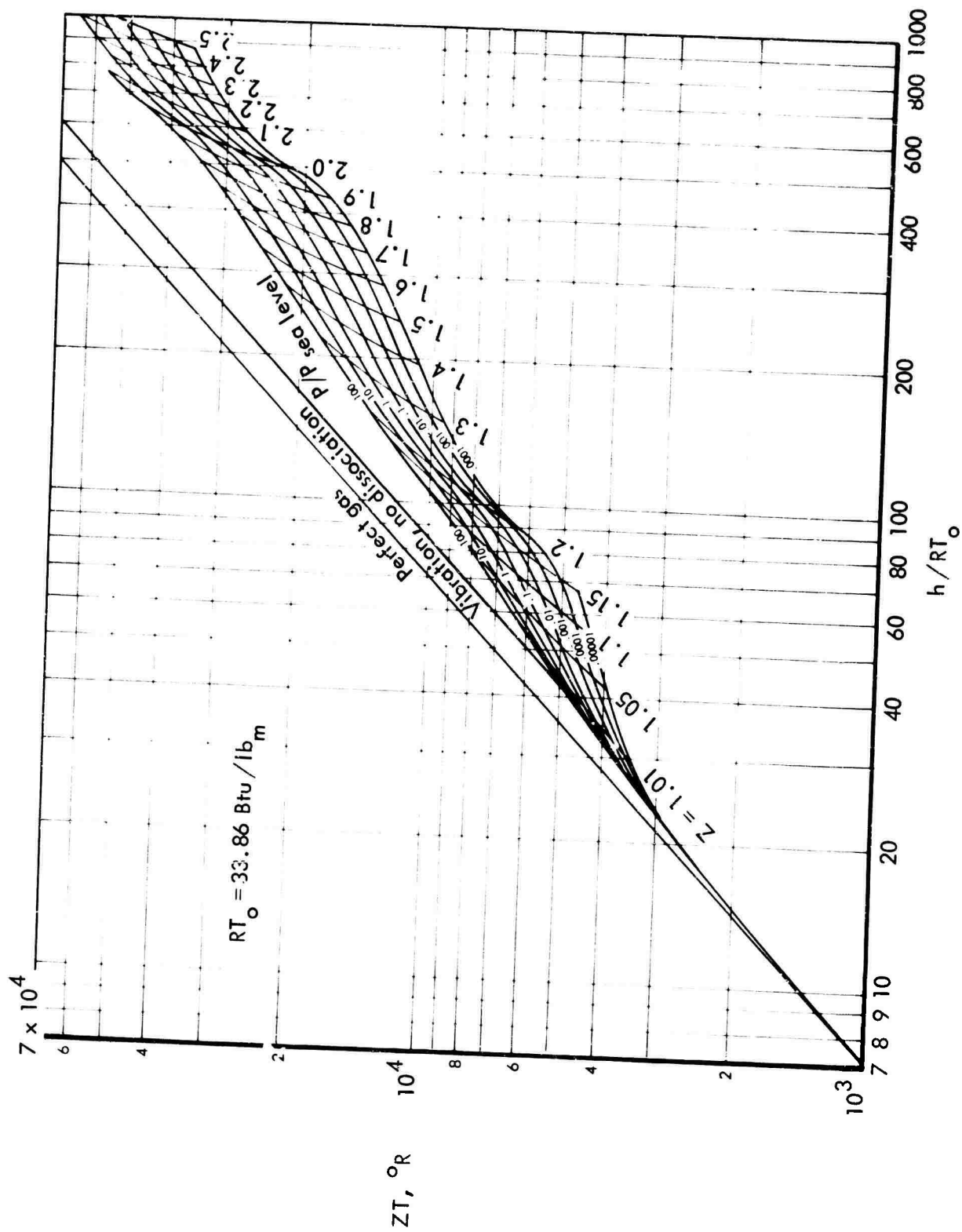


Figure 6: COMPRESSIBILITY-TEMPERATURE PRODUCT FOR AIR IN CHEMICAL EQUILIBRIUM

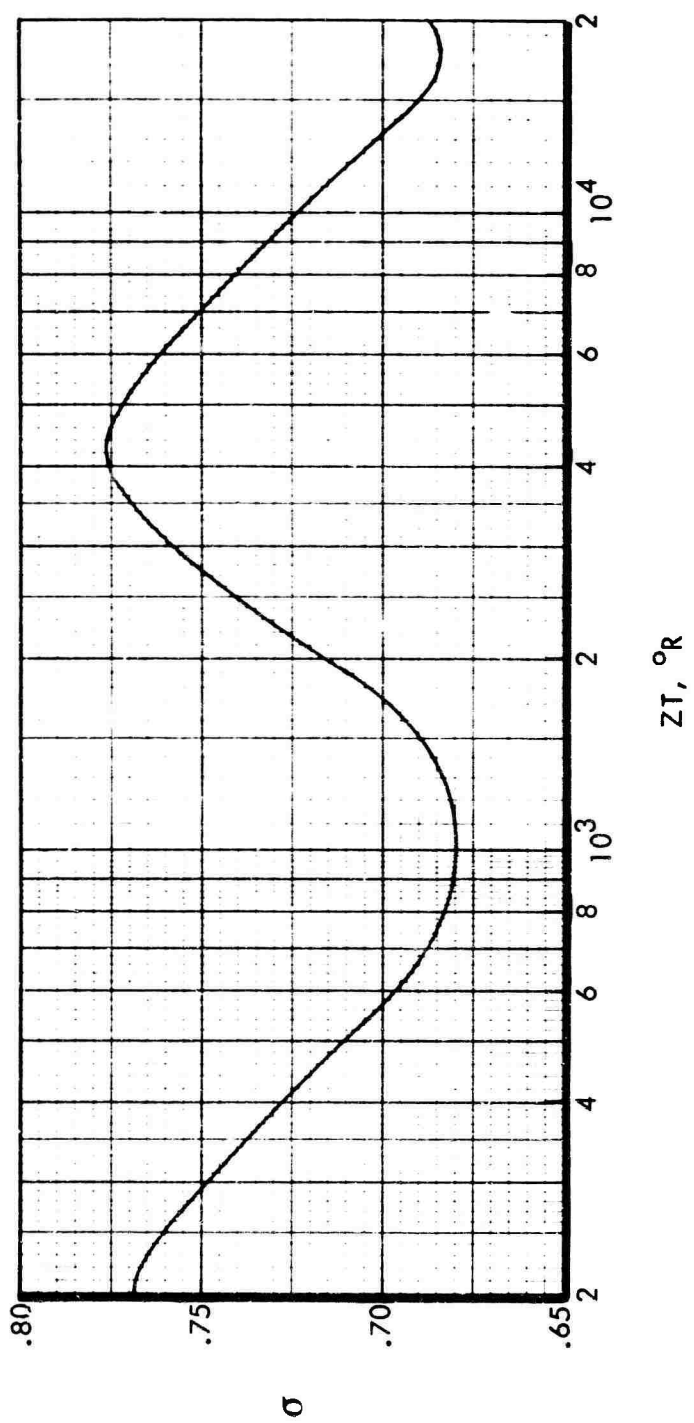


Figure 7: PARTIAL PRANDTL NUMBER FOR AIR

In the absence of a rigorous method, the influence of dissociation is assumed to be the same for turbulent and laminar flows. The laminar expression for  $\mathcal{L}$  is given by Equation (A-41) as:

$$\mathcal{L} = 1 + (N_{Le}^{.52} - 1) \left( \frac{i_{D,r}}{i_r} \right) \quad (21)$$

A plot of  $\mathcal{L}$  as a function of enthalpy and pressure for equilibrium air and a Lewis number of 1.4 is presented in Figure 20 in Appendix A.

## SECTION IV

### STREAMWISE PRESSURE GRADIENT EFFECTS

Except for boundary layer profiles, the effects of pressure variations on heating and skin friction are reflected in the product  $\rho_T \mu_T u_e$  appearing in the integrand in Equations (8) and (9). Changes in boundary layer profiles resulting from pressure gradients are accounted for in  $J_T$  and  $P_T$  appearing in the same equations.

At the time that these correlations were made (1964 and 1965), no reliable methods were available for estimating turbulent profile alterations due to streamwise pressure gradients. Consequently, the selection of expressions for evaluating  $J_T$  and  $P_T$  are based on comparisons with experimental data. The general form of these equations is based on the corresponding laminar relations presented in Appendix A. The expressions selected are:

$$J_T = J_L = \left[ 1 + .718 (\sqrt{1 + F_{\beta,s} F_{\Sigma,s}} - 1) \right] \text{ when } \beta_s > 0 \quad (22)$$

and,

$$J_T = J_L = \left[ 1 + .718 (\sqrt{1 + F_{\beta,s} F_{\Sigma,s}} - 1) \right]^{-1} \text{ when } \beta_s < 0 \quad (23)$$

Also:

$$P_T = P_L = J_L^5 \quad (24)$$

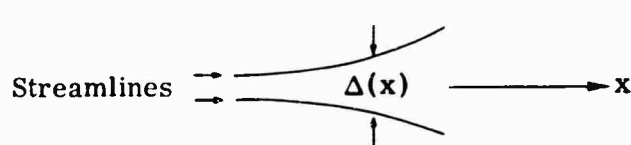
Expressions for evaluating  $F_{\beta,s}$  and  $F_{\Sigma,s}$  are given in Appendix A by Equations (A-50) through (A-53).

## SECTION V

### THREE-DIMENSIONAL EFFECTS

Although three-dimensional effects on turbulent heating are significantly less than for laminar flow, these effects can still be substantial. In particular, sizeable increases in heating due to crossflow pressure gradients can be experienced on leading edges and along the stagnation line of axisymmetric bodies at angles of attack.

In the present analysis, three-dimensional effects on heat transfer are reflected in the equivalent distance defined by Equation (8). The influence of streamline divergence due only to body geometry is determined by  $r$ , and that due to pressure gradients normal to the direction of flow by  $f$ . The combined effects of body geometry and crossflow pressure gradients on the streamline divergence at the boundary layer edge is defined by  $\Delta$ , where:

$$\Delta = rf$$


The diagram shows two streamlines that are parallel on the left and then diverge as they move to the right. A horizontal arrow labeled 'x' points to the right, indicating the direction of flow. The distance between the two streamlines at a specific point is indicated by two vertical arrows pointing towards each other, with the label  $\Delta(x)$  between them. The word 'Streamlines' is written to the left of the lines, with two arrows pointing to the streamlines.

The reason for treating the two causes of three-dimensional flow separately is that crossflow pressure gradients distort the crossflow velocity profile, whereas body geometry does not. The evaluation of the influence of this distortion on heat transfer is easier when crossflow effects are considered separately from geometric effects.

#### 1. GEOMETRIC EFFECTS— $r$ FACTOR

The streamline divergence parameter  $r$  is generally used in connection with axisymmetric flows, and is then defined as the circular radius of a body. In this analysis  $r$  is considered to be the distance between two adjacent streamlines at the edge of the boundary layer over the respective surface, and in the absence of crossflow pressure gradients. For most applications  $r$  can also be considered to be proportional to the body radius of curvature in the plane normal to the streamline.

An exception to this rule, delta wings at angle of attack, is discussed later in this section.

The simplest example of three-dimensional flow occurs on an unyawed cone in a uniform hypersonic flow. Noting that pressure is constant, and considering that the wall temperature is also constant, the product  $\rho_r \mu_r u_e$  appearing in Equations (8) and (9) is constant. Also, from Section IV it is seen that  $J_T$  and  $P_T$  are unity; hence, Equations (8) and (9) reduce to:

$$x_{eq, T} = S_{eq, T} = \frac{1}{[r]_{x_1}^{5/4}} \int_0^{x_1} r^{5/4} dx \quad (25)$$

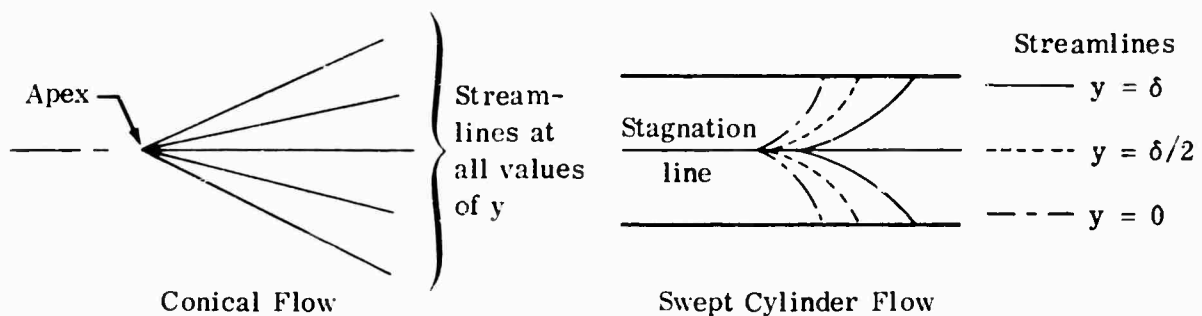
The streamline divergence parameter  $r$  is proportional to the circular radius, and is therefore proportional to  $x$ . Considering that  $H$  is approximately proportional to  $x_{eq, T}^{-2}$ , it is seen that:

$$\frac{H_{\text{cone}}}{H_{\text{2-D}}} = \left(\frac{9}{4}\right)^2 = 1.176 \quad (26)$$

For other types of unyawed axisymmetric bodies, the pressure is not usually constant, and the variation in  $\rho_r \mu_r u_e$  must be considered.

## 2. CROSSFLOW PRESSURE GRADIENTS— $f$ FACTOR

Estimating the effects of crossflow pressure gradients is more difficult than effects of body geometry because of rotation of the streamline patterns in the boundary layer. For example, consider the differences in the streamline pattern on an unyawed cone and a swept cylinder stagnation line sketched below:



The crossflow streamline divergence parameter  $f$  can be considered as proportional to the distance between two adjacent streamlines at the edge of the boundary layer in the absence of geometric effects. Methods of estimating  $f$  are presented later in this section.

The influence of the streamline rotation illustrated above is reflected in the cross-flow momentum thickness ratio  $\bar{E}$ . When streamlines are parallel throughout the depth of the boundary layer at a given station, then  $u/u_e = v/v_e$ . It is seen from Equation (A-25) that  $\bar{E}$  is unity for this case, and the effect of  $f$  becomes identical to that of  $r$  in the expression for heat transfer, Equation (5).

a. Evaluation of  $\bar{E}_T$

The behavior of  $\bar{E}$  in turbulent flow can be described only qualitatively, and most published analyses neglect its effect. However, its effect is usually to increase heating rates and is therefore included in the present method. As in the streamwise pressure gradient case, the turbulent values are based on modifications of the corresponding laminar correlations. However, unlike the streamwise parameter  $J_L$ ,  $\bar{E}_L$  is strongly influenced by Mach number, so that a dual modification is required.

Considering incompressible flow, it is seen from the definition of Equation (A-25) that the upper limit on  $\bar{E}$  is  $\delta^*/\theta$  unless the crossflow velocity component  $v$  within the boundary layer exceeds the external value. Laminar solutions (Reference 11) show that velocity overshoots ( $v/v_e > 1$ ) do not occur for cold-wall zero-Mach-number flow, hence a correction factor of the following form is suggested:

$$\frac{\bar{E}_{T,o}}{\bar{E}_{L,o}} = \frac{(\delta^*/\theta)_T}{(\delta^*/\theta)_L} = \text{constant} \quad (27)$$

However, an inconsistency is noted in that  $\bar{E}_{T,o}$  should be unity when  $\bar{E}_{L,o}$  is unity, since this condition implies that no profile distortion occurs due to crossflow pressure gradients (i. e.,  $v/v_e = u/u_e$ ). This inconsistency is avoided by adopting the following expression:

$$\frac{\bar{E}_{T,o} - 1}{\bar{E}_{L,o} - 1} = 0.77 \quad (28)$$

The constant .77 was selected primarily on the basis of experimental heating rates on swept cylinders.

In Equation (28),  $\bar{E}_{L,o}$  is just  $\bar{E}_L$  evaluated for Mach number equal to zero. For Mach number zero, Equation (A-58) reduces to:

$$i_{m,c,o} = \frac{1}{2} (i_{e,SL} + i_w) \quad (29)$$

Assuming that  $F_{\beta, c} = 1.0$ , and using Equations (28) and (A-49),

$$\bar{E}_{T, o} = 1 + .55 \left( \sqrt{1 + F_{\Sigma, c}} - 1 \right) \left( 2\Sigma_{c, o} \right)^{\exp K} \quad (30)$$

where  $\Sigma_{c, o} = (ZT)_{m, o} / (ZT)_{e, SL}$

and

$\exp K = 0$  when  $N \leq .05$  and  $.99 \leq N \leq 1.01$ ,

$\exp K = -.194 \exp \left[ -\frac{2}{3} N(N-1) \right]$  when  $.05 < N < .99$ ,

$\exp K = .194 \exp \left[ -\frac{2}{3} (N-1) \right]$  when  $N > 1.01$ , and  $N = (x/rf) (\partial rf / \partial x)$ .

The effect of Mach number on  $\bar{E}_T$  was determined from observation of empirical trends in swept cylinder stagnation-line turbulent heat-transfer data, as:

$$\frac{\bar{E}_T}{\bar{E}_{T, o}} = \left( \frac{\bar{E}_L}{\bar{E}_{L, o}} \right)^4 \quad (31)$$

The final expression for  $\bar{E}_T$  now becomes:

$$\bar{E}_T = 1 + .55 \left( \sqrt{1 + F_{\Sigma, c, o}} - 1 \right) \left( 2\Sigma_{c, o} \right)^{\exp K} \left[ \frac{1 + .718 \left( \sqrt{1 + F_{\Sigma, c}} - 1 \right) \left( 2\Sigma_c \right)^{\exp K}}{1 + .718 \left( \sqrt{1 + F_{\Sigma, c, o}} - 1 \right) \left( 2\Sigma_{c, o} \right)^{\exp K}} \right]^4 \quad (32)$$

where the sign on the exponents is plus when  $\partial(rf)/\partial x$  is positive, and negative when  $\partial(rf)/\partial x$  is negative. Although the analysis leading to Equation (32) is based on order-of-magnitude approximations, heat transfer estimates obtained using this method are shown in Figure 8 to agree reasonably well with test data obtained at the stagnation line of a swept cylinder.

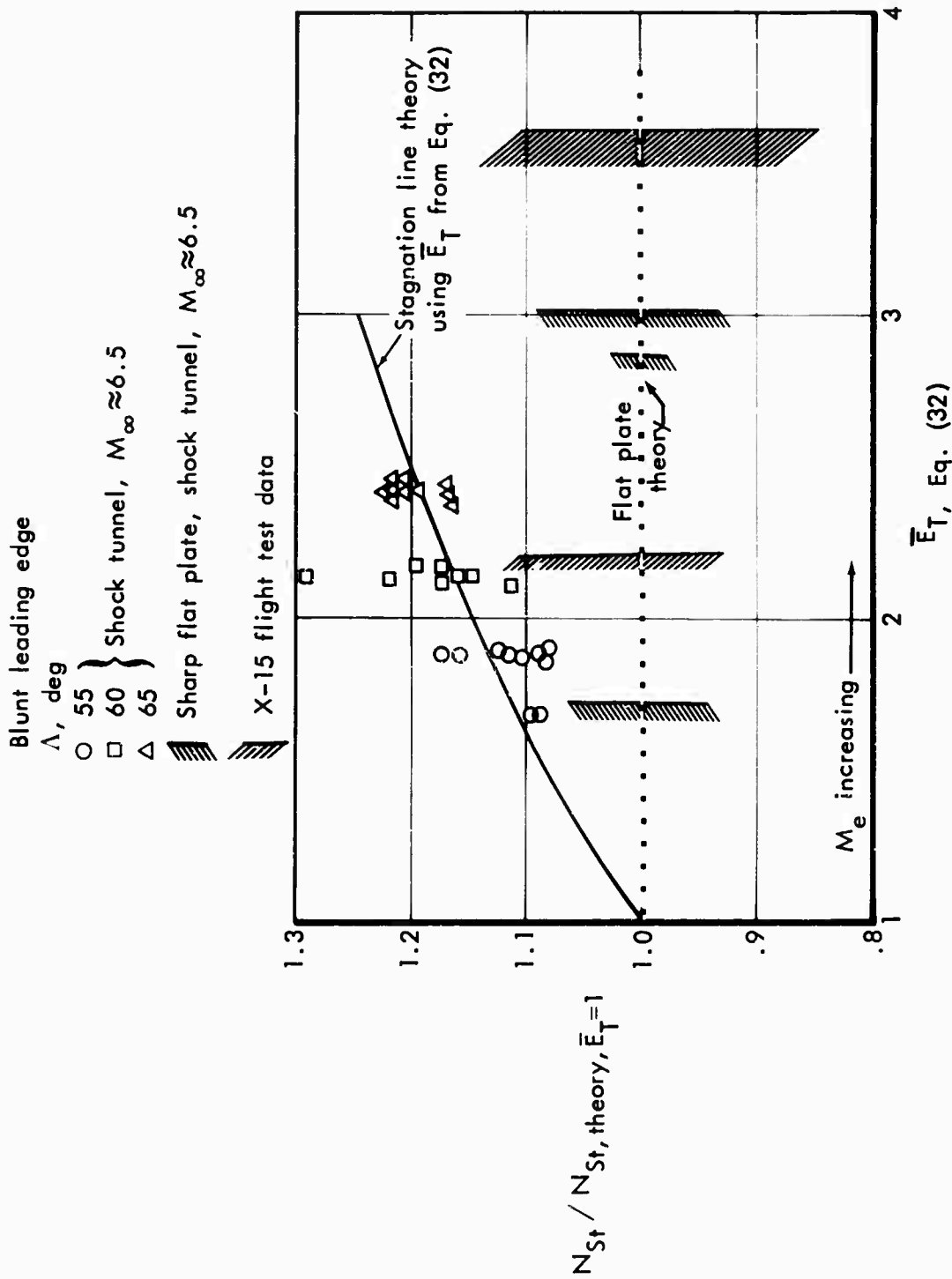


Figure 8: CROSSFLOW PRESSURE GRADIENT EFFECT ON CYLINDER STAGNATION-LINE TURBULENT HEAT TRANSFER

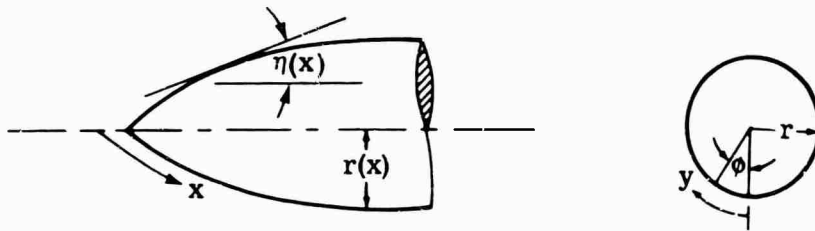
b. Evaluation of f

1) General Equation for Axisymmetric Bodies

The streamline divergence parameter  $f$  is obtained from a solution of the cross-flow momentum equation for inviscid flow given by:

$$\rho_e u_e \frac{\partial v_e}{\partial x} + \rho_e v_e \frac{\partial v_e}{\partial y} = - \frac{\partial P_e}{\partial y} \quad (33)$$

The coordinate system is defined in the sketches shown below:



Differentiating Equation (33) with respect to  $y$ , and noting that at the stagnation line  $v_e = \partial u_e / \partial y = \partial \rho_e / \partial y = 0$ , then:

$$\rho_e \left( \frac{\partial v_e}{\partial y} \right)^2 + \rho_e u_e \frac{\partial^2 v_e}{\partial x \partial y} = - \frac{\partial^2 P_e}{\partial y^2} \quad (34)$$

For most configurations, pressures are more easily expressed as a function of  $x$  and  $\phi$ . Equation (34) is now transformed to  $(x, \phi)$  coordinates. The relations for this transformation are:

$$\left. \frac{\partial(\ )}{\partial y} \right|_x = \frac{1}{r} \frac{\partial(\ )}{\partial \phi} \quad (35)$$

$$\left. \frac{\partial(\ )}{\partial x} \right|_y = \left. \frac{\partial(\ )}{\partial x} \right|_\phi - \frac{\phi}{r} \frac{dr}{dx} \left. \frac{\partial(\ )}{\partial \phi} \right|_x \quad (36)$$

In the transformed system, Equation (34) becomes:

$$\frac{\rho_e}{r} \left( \frac{\partial v_e}{\partial \phi} \right)^2 + \frac{\rho_e u_e}{r} \left[ \frac{\partial^2 v_e}{\partial x \partial \phi} - \frac{\partial v_e}{\partial \phi} \frac{dr/dx}{r} \right] = - \frac{1}{r^2} \frac{\partial^2 P_e}{\partial \phi^2} \quad (37)$$

Equation (37) cannot be easily solved unless it is assumed that  $\partial^2 v_e / \partial x \partial \phi = 0$ . This assumption is clearly valid for yawed cones, and numerical results indicate that errors introduced by neglecting this term on yawed ogives are small. Accordingly, Equation (37) is now simplified to:

$$\left(\frac{\partial \bar{v}}{\partial \phi}\right)^2 - \frac{\partial \bar{v}}{\partial \phi} \left| \frac{dr}{dx} \right| + \frac{\partial^2 \bar{P}}{\partial \phi^2} = 0 \quad (38)$$

where

$$\bar{v} = v_e / u_e$$

$$\bar{P} = P_e / \rho_e u_e^2$$

The solution to Equation (38) is given by the familiar quadratic equation, resulting in:

$$\frac{\partial \bar{v}}{\partial \phi} = \frac{1}{2} \left[ \frac{dr}{dx} \pm \sqrt{\left(\frac{dr}{dx}\right)^2 - 4 \frac{\partial^2 \bar{P}}{\partial \phi^2}} \right] \quad (39)$$

The proper sign in Equation (39) is positive, as seen in the special case for the stagnation line of a swept cylinder ( $\partial r / \partial x = 0$ ) for which the positive value of  $\partial \bar{v} / \partial \phi$  shows diverging streamlines. Thus:

$$\frac{\partial \bar{v}}{\partial \phi} = + \sqrt{-\partial^2 \bar{P} / \partial \phi^2}$$

It is seen from Equation (39) that when  $\partial^2 \bar{P} / \partial \phi^2 = 0$ , then  $\partial \bar{v} / \partial \phi = \partial r / \partial x$ . Thus,  $\partial \bar{v} / \partial \phi$  reflects the streamline divergence due to body geometry as well as crossflow pressure gradients. This result appears to be inconsistent with Equation (A-10), which shows that  $\bar{v}$  includes only crossflow effects. The reason for this apparent contradiction is that in the analysis shown above,  $v$  is defined as the velocity component normal to lines of constant  $y$ , but in Appendix A,  $v$  is the component normal to lines of constant  $\phi$ . With the terminology used in this section:

$$\frac{1}{r} \frac{\partial r}{\partial x} + \frac{1}{f} \frac{\partial f}{\partial x} = \frac{1}{r} \frac{\partial \bar{v}}{\partial \phi}$$

or,

$$\frac{1}{f} \frac{\partial f}{\partial x} = \frac{1}{2r} \left[ -\sin \eta + \sqrt{\sin^2 \eta - 4 \frac{\partial^2 \bar{P}}{\partial \phi^2}} \right] \quad (40)$$

where

$$\sin \eta = \partial r / \partial x$$

2) Evaluation of  $\partial^2 \bar{P} / \partial \phi^2$

Near the stagnation line the pressure variation with  $\phi$  is defined by:

$$C_p = C_{p,SL} \frac{\sin^2 \delta}{\sin^2 \delta_{SL}} \quad (41)$$

where  $\delta$  is the angle of the surface with respect to the free-stream flow. For an axisymmetric body:

$$\sin \delta = \cos \alpha \sin \eta + \sin \alpha \cos \eta \cos \phi \quad (42)$$

Using Equations (41) and (42), it is easily shown that:

$$\frac{\partial^2 \bar{P}}{\partial \phi^2} = -2 \bar{P} \left[ \frac{\sin \alpha \cos \eta}{\sin(\alpha + \eta)} \right] \left( 1 - \frac{P_\infty}{P_e} \right) \quad (43)$$

Methods for evaluating  $\bar{P}$  for a few simple geometries are presented in Section VIII.

### 3. SPECIAL CASES

#### a. Swept Cylinder Stagnation Line

For the stagnation line of swept cylinders  $dr/dx = 0$ , thus only crossflow effects need be considered. For this case, Equation (40) reduces to:

$$\frac{1}{f} \frac{\partial f}{\partial x} = - \frac{1}{r} \frac{\partial^2 \bar{P}}{\partial \phi^2} \quad (44)$$

$\partial^2 \bar{P} / \partial \phi^2$  is found from Equation (43). Then,

$$f = \exp \left( - \frac{x}{r} \frac{\partial^2 \bar{P}}{\partial \phi^2} \right) \quad (45)$$

For this case  $\rho_r \mu_r u_e$  can normally be considered constant, and  $J_T$  is seen to be unity ( $\beta_s = 0$ ). Equation (8) now simplifies to:

$$\begin{aligned} x_{\text{eq}, T} &= \frac{1}{\frac{5}{4} \frac{\bar{E}_T}{f}} \int_0^{x_1} f^{\frac{5}{4}} \bar{E} dx \\ &= \frac{1}{-\frac{5}{4} \frac{\bar{E}_T}{r} \frac{\partial^2 \bar{P}}{\partial \phi^2}} \left[ 1 - \exp \left( \frac{x_1}{r} \frac{\partial^2 \bar{P}}{\partial \phi^2} \right) \right] \end{aligned} \quad (46)$$

For very large values of  $x$  (e.g., infinite cylinder), Equation (46) becomes:

$$x_{\text{eq}, T} = \frac{1}{-\frac{5}{4} \frac{\bar{E}_T}{r} \frac{\partial^2 \bar{P}}{\partial \phi^2}} \quad (47)$$

#### b. Yawed Cone Stagnation Line

The flow along the stagnation line of a yawed cone differs from that on the swept cylinder only in that:

$$\frac{dr}{dx} = \sin \eta$$

where  $\eta$  is the cone half-angle (degrees). For this case, Equation (40) becomes:

$$\frac{1}{f} \frac{df}{dx} = \frac{1}{2x} \left[ -1 + \sqrt{1 - \frac{4}{\sin^2 \eta} \frac{d^2 \bar{P}}{d\phi^2}} \right] \quad (48)$$

A solution for  $f$  is given by:

$$f = cx^N$$

$$N = \frac{1}{2} \left[ 1 + \sqrt{1 - \frac{4}{\sin^2 \eta} \frac{d^2 \bar{P}}{d\phi^2}} \right] \quad (49)$$

Again,  $\rho_1 \mu_1 u_e$  can be considered constant, and  $J_T$  assumed to be unity. Hence,

$$\begin{aligned} x_{\text{eq. T}} &= \frac{1}{x_1 \frac{5}{4} (1 - \bar{E}_T N)} \int_0^{x_1} x^{\frac{5}{4}} (1 - \bar{E}_T N) dx \\ &= \frac{x_1}{1 - \frac{5}{4} (1 - \bar{E}_T N)} \end{aligned} \quad (50)$$

### c. Delta Wing Centerline

Three-dimensional effects along the wing centerline of delta wings at angles of attack were estimated using a method presented in References 2 and 4. This method is based on numerical solutions by the method of Kennet (Reference 12) and wedge theory. The method of Reference 12 is valid only at high angles of attack where the shock wave is detached from the leading edges, while wedge theory is applicable only at low angles of attack. The method of Reference 2 uses the results of Kennet and wedge theory to provide a means of making estimates at intermediate angles of attack.

Near the wing centerline it was found that the edge streamlines could be expressed by:

$$\Delta \propto x^n \quad (51)$$

A correlation for  $n$  reported in Reference 2 is given by:

$$n = (1 + \phi^{**}/\beta) \bar{N}_{CL} \left( \frac{M_n^2}{M_n^2 + 1} \right) \quad (52)$$

where

$$\phi^{**} \equiv \tan^{-1} \left\{ \left( \frac{\gamma-1}{\gamma+1} \right) \left[ \left[ 1 + \frac{2}{\gamma-1} \frac{1}{M_\infty^2} \left( \frac{M_n^2 - 1}{M_n^2} \right) \right] \left( \frac{u_\infty}{u_e} \right)^2 - 1 \right] \right\}^{\frac{1}{2}}$$

$$\beta = 90^\circ - \Lambda$$

$$\text{and } M_n = M_\infty \sin \left[ \tan^{-1} \left( \frac{\sin \alpha}{\cos \alpha \cos \Lambda} \right) \right]$$

$\bar{N}_{CL}$  is presented as a function of  $\phi^{**}/\beta$  and sweep angle  $\Lambda$  in Figure 9.

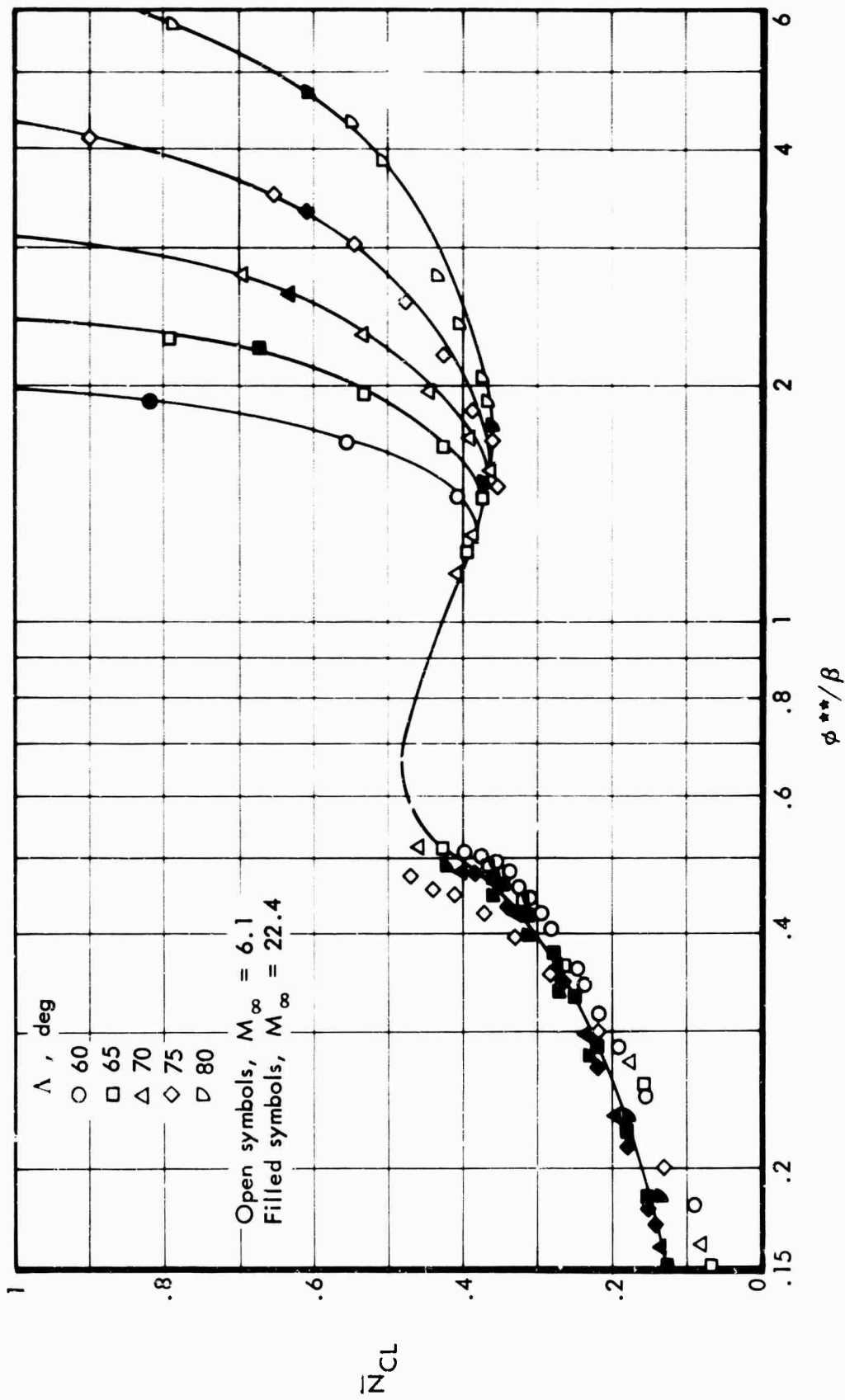


Figure 9: STREAMLINE CORRELATION FOR SHARP DELTA WINGS

In estimating three-dimensional flow effects on heating it is again necessary to separate the influence of geometry and crossflow pressure gradients. In this case  $r$  can vary with  $x$  even though no body curvature exists. This variation is caused by shock wave curvature, and cannot be easily estimated. However, it can be shown from the spanwise momentum equation that crossflow pressure gradients will cause streamline curvature. Hence, it is concluded that when the streamlines are straight the influence of crossflow pressure gradients can be neglected ( $df/dx = 0$ ). This condition is satisfied when  $n$  is either zero (two-dimensional flow) or unity (conical flow). The following relationships were found to satisfy these two conditions.

$$\left. \begin{array}{l} r \propto x^{n(2-n)} \\ f \propto x^{n(n-1)} \end{array} \right\} n \leq 1$$

$$\left. \begin{array}{l} r \propto x \\ f \propto x^{n-1} \end{array} \right\} n > 1 \tag{53}$$

## SECTION VI

### NONISOTHERMAL WALL EFFECTS

Nearly all methods for estimating turbulent heating rates are applicable only to isothermal surfaces. However, in practice, sizeable wall temperature gradients can exist because of variations in local heating rates, surface emissivities, and the presence of internal heat sinks (e. g., cryogenics). In evaluating these effects it is convenient to consider separately the influence of variations of temperature level and that of temperature gradients.

Boundary layer growth is influenced by local wall temperature. Consequently, the boundary layer thickness, and therefore, the local heat transfer coefficient, is dependent on the wall temperature at all upstream locations. The influence of upstream variations in wall temperature are reflected through the  $\rho_r \mu_r$  terms in the equivalent distances defined by Equations (8) and (9). However, these effects on heat transfer rates are usually much smaller than the effects of the corresponding thermal gradients.

The following paragraphs describe a method presented in Reference 1 for estimating effects of thermal gradients. In this method the influence of thermal gradients on heat transfer rates is accounted for by introducing an effective thermal potential term  $\Phi$ , where:

$$\dot{q} = H (i_{aw} - i_{w,0} + \Phi) \quad (54)$$

The subscript 0 denotes that the wall enthalpy is evaluated at  $x = 0$ . The method for evaluating  $\Phi$  is essentially a modification of a method proposed by Seban and described in Reference 13.<sup>3</sup> The approximation of  $\Phi_T$  suggested by Seban is:

$$\Phi_{T, x=x_1} = - \int_0^{x_1} \frac{di_w}{dx} \left[ 1 - \bar{x}^{9/10} \right]^{-1/10} dx \quad (55)$$

where

$$\bar{x} = x/x_1$$

3 The derivation presented in Reference 13 is based on wall temperatures instead of enthalpies.

In spite of its innocuous appearance, Equation (55) cannot be easily integrated. Even numerical integration is difficult because of the singularity occurring when  $x = x_1$ . An alternate formulation is presented in Reference 14 that permits an easier numerical solution as follows:

$$\int_0^{x_1} \frac{di_w}{dx} \left[ 1 - \bar{x}^{9/10} \right]^{-1/10} dx = \int_0^x \frac{di_w}{dx} \frac{d\bar{S}}{dx} dx \quad (56)$$

where

$$\bar{S} = \int_0^{\bar{x}} \left[ 1 - (\xi/x_1)^{9/10} \right]^{-1/10} d(\xi/x_1) \quad (57)$$

where  $\xi$  is a dummy variable in  $x$ .

Solutions to Equation (57) are presented in tabular form in Reference 14. If  $i_w$  is continuous, the integral in Equation (56) can be obtained numerically using:

$$\Phi_{T, x=x_1} = \int_0^{x_1} \frac{di_w}{dx} \frac{d\bar{S}}{dx} dx = x_{i=n} \sum_{i=1}^n \frac{i_{w,i} - i_{w,i-1}}{x_i - x_{i-1}} \left[ \bar{S}_i - \bar{S}_{i-1} \right] \quad (58)$$

The solution of Equation (58) is still tedious, since the numerical integration from  $x = 0$  must be repeated at each station in  $x$ . The computations can be significantly reduced by using the following approximation:

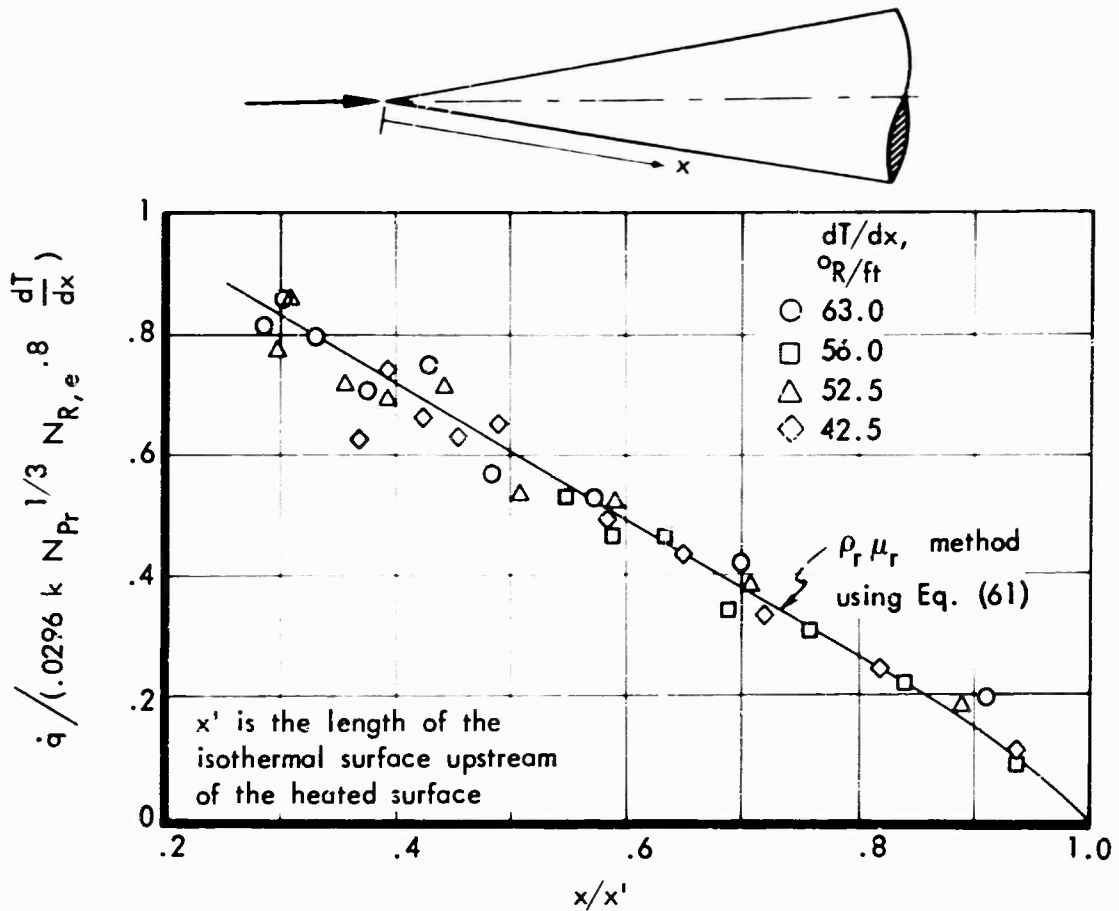
$$\left[ \bar{S}_i - \bar{S}_{i-1} \right] \approx \left[ \bar{x}_i - \bar{x}_{i-1} \right] \left[ 1 - \bar{S}_i^{9/10} \right]^{-1/10} \quad (59)$$

where

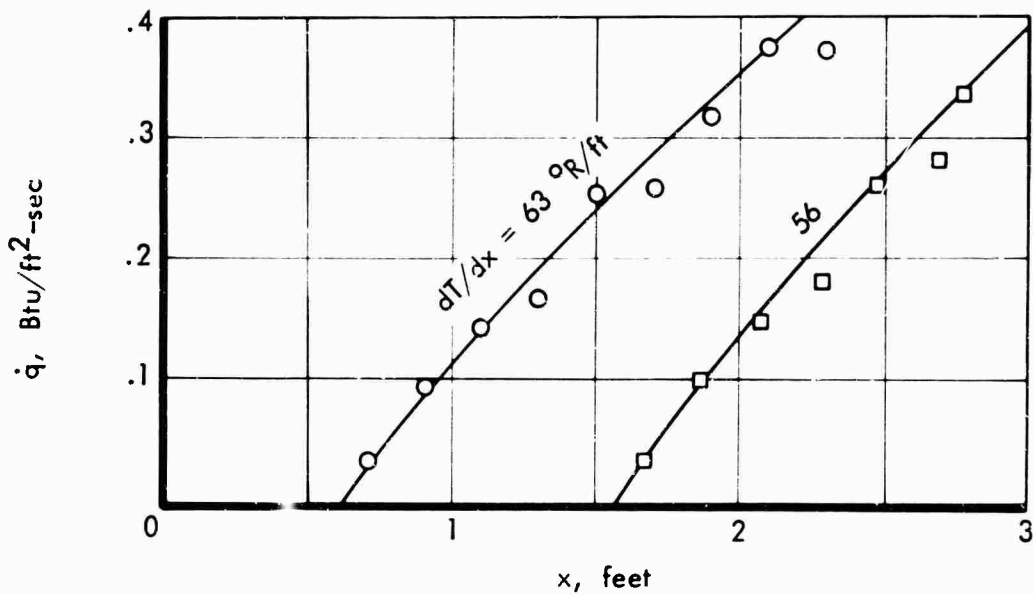
$$\bar{S}_i = \bar{x}_i - \frac{1}{3} (\bar{x}_i - \bar{x}_{i-1})$$

This method has been incorporated into the  $\rho_r \mu_r$  program (Volume III). Program results are shown in Figure 10 to agree well with experimental data reported in Reference 13. Comparisons between results from Equations (57) and (59) are given below:

$\bar{x}_i$	$\bar{x}_{i-1}$	$(\bar{S}_i - \bar{S}_{i-1}) / (\bar{x}_i - \bar{x}_{i-1})$	
		Reference 13 Equation (57)	Equation (59)
.15	0	1.013	1.015
.3	0	1.024	1.030
.3	.15	1.033	1.038
.65	.5	1.114	1.117
1	.7	1.297	1.306
1	.85	1.400	1.411
1	.97	1.665	1.688



a) General Correlation



b) Typical Comparison

Figure 10: MEASURED AND THEORETICAL TURBULENT HEATING RATES WITH LINEAR WALL TEMPERATURE GRADIENT ON A SHARP CONE

The foregoing analysis is restricted to flat plate flows. The influence of pressure gradients and three-dimensional effects are included by replacing the dimensionless streamwise distance  $\bar{x}$  with an equivalent distance  $\bar{S}_T'$ , where

$$\bar{S}_T' = \frac{\int_0^{\bar{x}_i} \rho_r \mu_r u_e (rf \bar{E})^{5/4} d\bar{x}}{\int_0^1 \rho_r \mu_r u_e (rf \bar{E})^{5/4} d\bar{x}} = \frac{\int_0^{x_i} G_T dx}{\int_0^x G_T dx} \quad (60)$$

The basis for this definition of  $\bar{S}_T'$  rests primarily on a similar analysis for laminar flows presented in Reference 1.

The set of equations for estimating the effects of wall temperature gradients is given in finite difference form by:

$$\dot{q}_T = H_T (i_{aw} - i_{w,0} + \Phi_T) \quad (61)$$

where

$$\Phi_T = \sum_{i=1}^n (i_{w,i} - i_{w,i-1}) \left[ 1 - (\bar{S}_i)'^{9/10} \right]^{-1/9}$$

$$\bar{S}_i' = \frac{\bar{S}_i' - 1/3(\bar{S}_i' - \bar{S}_{i-1}')}{S_n'}$$

and

$$\bar{S}_i' = \frac{\sum_{j=1}^i (G_j - G_{j-1})(x_j - x_{j-1})}{\sum_j^n (G_j - G_{j-1})(x_j - x_{j-1})}$$

## SECTION VII

### NOSE BLUNTNESSE EFFECTS

The flow field surrounding a vehicle in hypersonic flight is dependent on the nose geometry. The presence of a blunt nose, for example, tends to increase static temperature and decrease velocity at the boundary layer edge. This effect, which can extend many diameters downstream of the nose, can cause a substantial decrease (30 to 40 percent) in aerodynamic heating rates.

Nose bluntness effects are dependent on the vehicle configuration, Mach number, Reynolds number, wall cooling, and total enthalpy (real gas effects). Two limiting cases are immediately recognized. A good estimate of the upper bound on heating can be obtained by assuming sharp body values for local velocity and enthalpy. Conversely, the lower limit is obtained by assuming all of the fluid in the boundary layer has passed through a normal shock in computing local flow properties. The flow conditions at the boundary layer edge are then obtained assuming an isentropic expansion from the stagnation to the local pressure. This approach is restricted to equilibrium or frozen flows.

An approximate method for interpolating between the upper and lower heating limits was developed during the present study. The derivation of this method is presented in this section, and data-theory comparisons are presented in Volume II of this report.

#### 1. SHOCK ANGLE EFFECTS ON STANTON NUMBER

The first step in the present analysis was to determine the influence of the shock angle  $\epsilon$  on the Stanton number  $N_{St}$ . Calculations of  $N_{St}$  were made using the  $\rho_r \mu_r$  method for edge velocities and static enthalpies corresponding to several shock angles. Local static pressures were assumed to be unaffected by bluntness. The local flow properties were calculated assuming an isentropic expansion behind the shock wave. The results, shown in Figure 11, indicate that:

$$N_{St} \approx N_{St, NS} + \frac{\sin^2 \epsilon}{\sin^2 \epsilon_{Sh}} (N_{St, Sh} - N_{St, NS}) \quad (62)$$

The subscript NS denotes that the evaluation is made for a normal shock ( $\epsilon = 0$ ) and Sh denotes that the evaluation is for a sharp body with an attached shock.

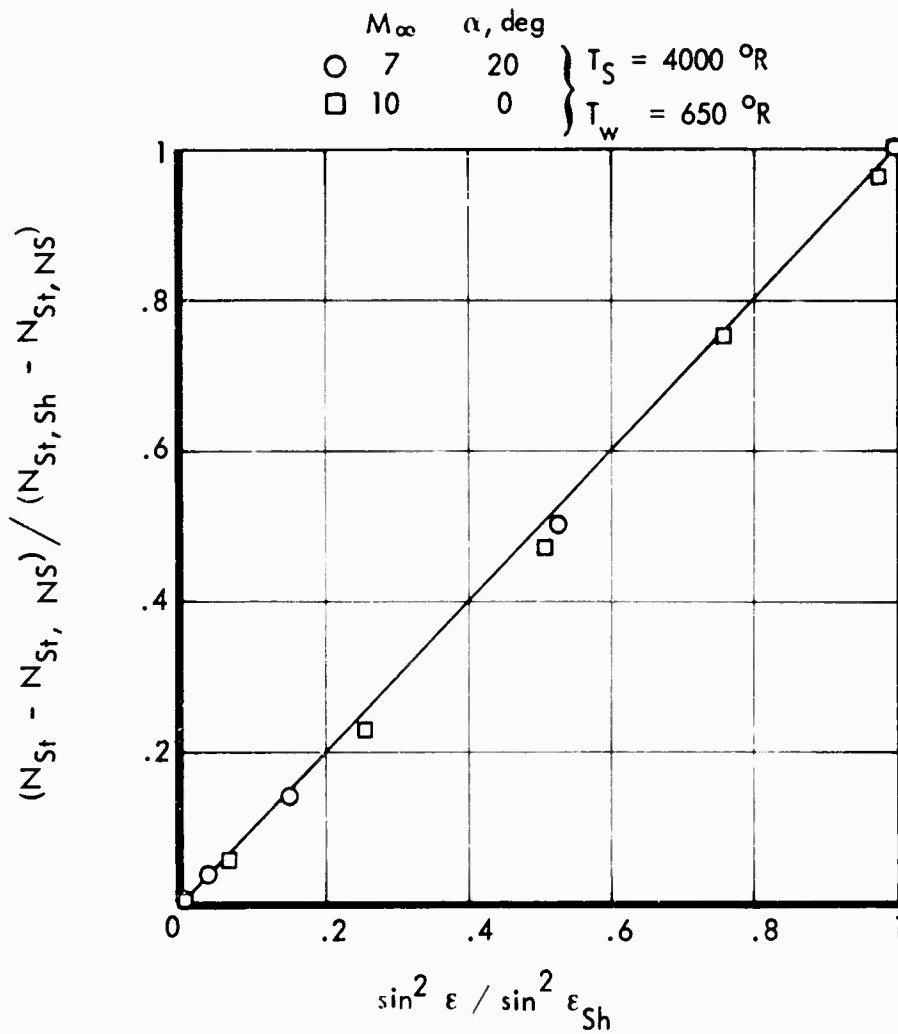
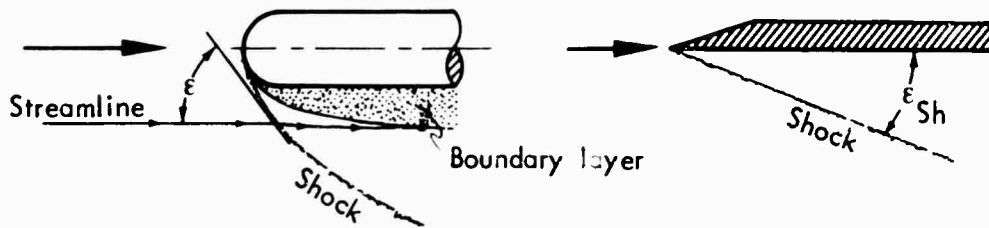
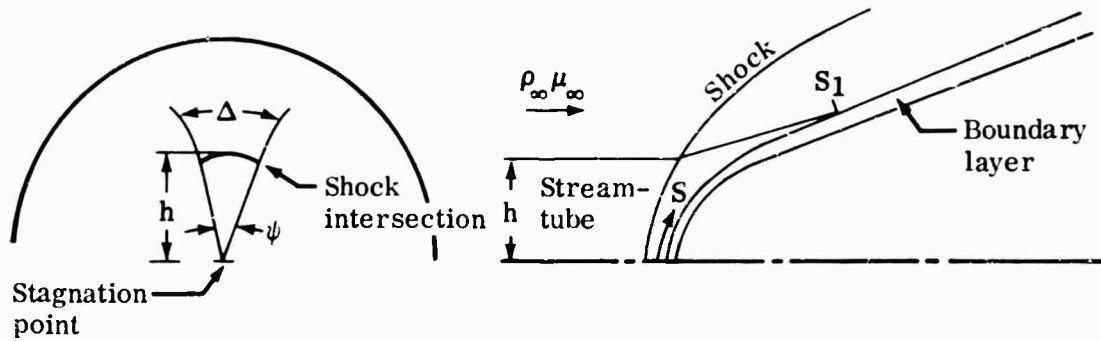


Figure 11: VARIATION OF HEAT TRANSFER COEFFICIENT WITH SHOCK ANGLE ON A BLUNT FLAT PLATE

## 2. MASS CONSERVATION ANALYSIS

The shock strength applying to the boundary layer at any given location was determined using the simple streamtube concept sketched below:



The mass flow rate,  $\dot{m}$ , in the streamtube entering the shock layer is:

$$\dot{m}_{\text{Shock}} = \frac{1}{2} \rho_{\infty} u_{\infty} h^2 \psi \quad (63)$$

Similarly, the mass flow rate in the boundary layer at  $S = S_1$  is:

$$\dot{m}_{\text{BL, } S=S_1} = \Delta \int_0^{\delta} \rho u dy = \rho_e u_e (\delta - \delta^*) \Delta \quad (64)$$

The angle  $\psi$  determines the width of the streamtube at the shock, and  $\Delta$  is the corresponding streamtube width at the boundary layer edge. Since the mass flow must be constant in the streamtube:

$$\frac{1}{2} \rho_{\infty} u_{\infty} h^2 \psi = \rho_e u_e (\delta - \delta^*) \Delta \quad (65)$$

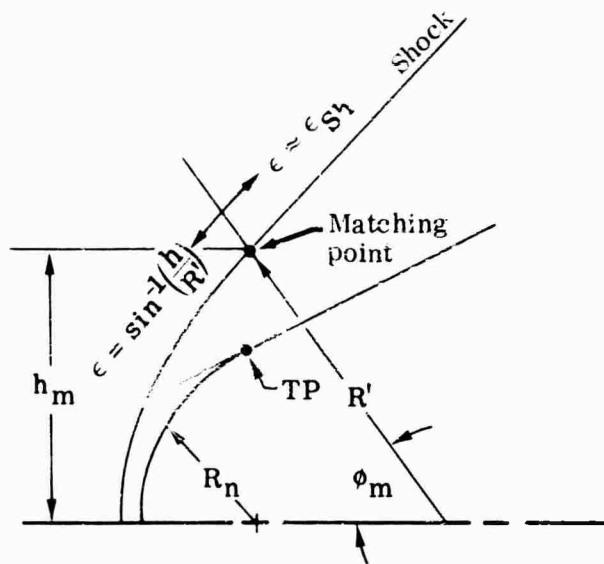
The relationship between the streamtube height  $h$  and the shock angle  $\epsilon$  is illustrated in the sketch on the following page.

Downstream of the matching point,  $\epsilon$  is assumed to be uninfluenced by bluntness. Upstream, the shock wave radius of curvature  $R'$  is assumed to be constant, and is expressed by

$$R' \propto R_n \left( \frac{\phi_m}{90^\circ - \epsilon_m} \right) \quad (66)$$

Hence,

$$h = R' \sin \epsilon \propto R_n \sin \epsilon \left( \frac{\phi_m}{90^\circ - \epsilon_m} \right) \quad (67)$$



Substituting Equation (67) into Equation (65) and solving for  $\sin^2 \epsilon$  gives

$$\sin^2 \epsilon \propto \frac{\rho_e u_e (\delta - \delta^*)}{\rho_\infty u_\infty R_n^2} \left( \frac{90^\circ - \epsilon_m}{\phi_m} \right)^2 \left( \frac{\Delta}{\psi} \right)^2 \quad (68)$$

Methods for obtaining the streamtube width  $\Delta$  are presented in Section V. On the hemisphere, the flow is assumed to be axisymmetric. At the tangent point TP of the hemisphere-wing centerline

$$\Delta_{TP} \approx \psi R_n \cos \phi_m \quad (69)$$

The angle delta is the angle of the body surface with respect to the free stream flow. Using Equation (69), Equation (68) becomes

$$\sin^2 \epsilon = C_B \frac{\rho_e u_e}{\rho_\infty u_\infty} \left( \frac{\delta - \delta^*}{R_n} \right) \left( \frac{90^\circ - \epsilon_m}{\phi_m} \right)^2 \left( \frac{\Delta}{\Delta_{TP}} \right)^2 \cos \phi_m \quad (70)$$

### 3. EVALUATION OF $(\delta - \delta^*)$

If pressure gradient effects are neglected, the thickness parameter  $(\delta - \delta^*)$  is easily related to the momentum thickness  $\theta$ . Following the practice of Beckwith and

Gallagher (Reference 14), it is assumed that the velocity and enthalpy profiles can be related to the corresponding incompressible profiles by the following transformation:

$$Y = \int_0^y (\rho/\rho_e) dy$$

$$\bar{\delta} = Y_{y=\delta} \quad (71)$$

The velocity ratio  $u/u_e$  is then considered to be a function only of  $Y/\bar{\delta}$ , and independent of wall cooling and Mach number. Thus:

$$\frac{\delta - \delta^*}{\theta} = \frac{\int_0^\delta \frac{\rho u}{\rho_e u_e} dy}{\int_0^\delta \frac{\rho u}{\rho_e u_e} \left(1 - \frac{u}{u_e}\right) dy} = \frac{\int_0^1 \frac{u}{u_c} d(Y/\bar{\delta})}{\int_0^1 \frac{u}{u_c} \left(1 - \frac{u}{u_e}\right) d(Y/\bar{\delta})}$$

$$= \left(\frac{\delta - \delta^*}{\theta}\right)_{inc} \quad (72)$$

If the influence of pressure gradients is neglected, then  $u/u_e \approx (Y/\bar{\delta})^{1/7}$ , which gives:

$$\frac{\delta - \delta^*}{\theta} = 9.0 \quad (73)$$

The momentum thickness  $\theta$  can be obtained either by using the  $\rho_r \mu_r$  program described in Volume III or from Equation (18).

#### 4. EVALUATION OF BLUNT BODY CONSTANT $C_B$

Using Equations (70) and (73), Equation (62) becomes:

$$N_{St} = N_{St} + \left(\frac{C_B}{\sin^2 \epsilon_m}\right) \left(\frac{\rho_e u_e}{\rho_\infty u_\infty}\right) \left(\frac{\cos \phi_m}{R_n}\right) \left(\frac{\Delta}{\Delta_{TP}}\right) \left(\frac{90^\circ - \epsilon_m}{\phi_m}\right)^2 \theta \left[ N_{St, Sh} - N_{St, NS} \right] \quad (74)$$

$\epsilon_m$  is assumed to correspond to the equivalent attached shock angle. Bluntness affects  $\rho_e$ ,  $u_e$ ,  $\theta$ , and  $\Delta$ . However, including this effect would require a tedious iterative treatment. Excellent agreement with data was obtained, however, when these parameters were computed for an attached shock along with the approximation that  $C_B = 7$ .

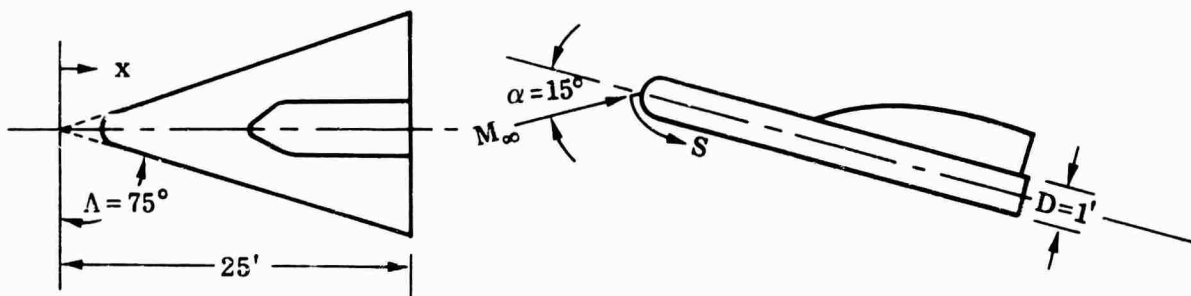
## SECTION VIII

### APPLICATIONS

Equations and correlations defining the  $\rho_r \mu_r$  method for computing turbulent heating rates are presented in preceding sections and in Appendix A of this volume. In this section, applications of this method in estimating turbulent heating on a blunt delta wing configuration during orbital reentry are described. Three gas models are used in order to illustrate real-gas effects. The application of the  $\rho_r \mu_r$  method in extrapolating experimental heat transfer data obtained from ground facilities to flight conditions is also discussed.

#### 1. GEOMETRY AND TRAJECTORY

The configuration selected for this analysis is a delta wing with a hemispherical nose cap and cylindrical leading edges. The dimensions are given in the sketch shown below.



The flight path selected is 20,000 feet below the equilibrium glide trajectory for a  $W/SC_L$  of 150. This path represents a severe reentry heating trajectory. The 15-degree angle of attack approximates the condition for maximum lift to drag ratio for this geometry.

#### 2. FLOW FIELD AND GAS PROPERTIES

The following information regarding flow field and gas properties is required in order to estimate turbulent heat transfer coefficients using the  $\rho_r \mu_r$  method:

1. surface pressure and streamwise pressure gradient
2. velocity,  $u_e$ , and enthalpy,  $i_e$ , at the boundary layer edge
3. temperature,  $T_w$ , or enthalpy,  $i_w$ , at the wall

4. streamline divergence parameters  $r$  and  $f$
5. diffusion parameter  $\mathcal{L}$
6. viscosity,  $\mu$ , partial Prandtl number,  $\sigma_p$ , and compressibility factor-temperature product,  $ZT$ .

The flow field parameters (items 1 through 4) must be specified at all points along a streamline. The gas properties (items 5 and 6) are usually specified as a function of pressure and enthalpy.

a. Surface Pressures

Pressures along the delta-wing lower surface are obtained using methods presented in Reference 2. The expression for sharp delta wing pressure coefficients is:

$$C_P = 2 (\sin \alpha) \left| \frac{\sin(\alpha + \xi)}{\cos \xi} \right| \quad (75)$$

The shock standoff angle  $\xi$  is obtained using:

$$\xi = 70 \left( \frac{\rho_\infty}{\rho_e} \right) \left( \frac{\tan \alpha}{\tan \Lambda} \right)^{.566} \quad (\text{degrees}) \quad (76)$$

Equation (76) is an empirical fit to numerical flow field solutions obtained on a sharp delta wing using the method of Reference 12. Results from this method are in good agreement with those from Reference 4.

The influence of nose bluntness is estimated using the following equation suggested by van Hise (Reference 15).

$$C_P - C_{P_{\text{Sharp}}} = \frac{.12}{\gamma} \frac{C_{D,n}}{(S/D)} - \frac{.9}{M_\infty^2} \quad (77)$$

The drag coefficient for the hemisphere ( $C_{D,n}$ ) is assumed to be 0.8, which is obtained by integrating the hemisphere pressures given in Reference 4.

Pressures on the leading edge are computed assuming the shock wave is parallel to the surface. For this case, the stagnation line pressure is equal to the total pressure based on the flow component normal to the leading edge. Except very near the nose, real-gas effects on pressures were found to be small at the flight conditions considered, and are neglected in this analysis.

b. Edge Velocities

The velocities at the boundary layer edge for the sharp delta wing case are computed using Equation (78) which is an empirical expression presented in Reference 4.

$$\frac{u_e}{u_\infty} = 1 - \frac{\alpha^2}{5600} \quad (78)$$

Where  $\alpha$  is in degrees.

The velocities for the normal shock calculations are computed assuming an isentropic expansion from the stagnation point. Bluntness effects on heat transfer are estimated from the sharp and normal shock results using Equation (74).

Consistent with the parallel shock assumption, stagnation line velocities are obtained by:

$$\frac{u_e}{u_\infty} = \cos \Lambda_{\text{eff}} \quad (79)$$

For an unyawed condition, the effective sweep angle ( $\Lambda_{\text{eff}}$ ) is expressed by:

$$\Lambda_{\text{eff}} = \sin^{-1} \left( \frac{\sin \Lambda}{\sin \alpha} \right) \quad (80)$$

c. Wall Temperatures

The wall temperatures are assumed to be constant over the vehicle at any given instant of time. These temperatures are given as a function of velocity and altitude in the following table.

<u><math>V_\infty</math>, ft/sec</u>	<u>ALT, ft</u>	<u><math>T_w</math>, °R</u>
18,700	187,000	3040
16,000	171,500	2960
14,000	160,500	2840
12,000	149,000	2660
10,000	137,500	2400
8,000	125,000	2100

These temperatures are representative of equilibrium values for a radiation cooled surface.

d. Streamline Divergence Parameters

The streamline divergence parameters  $r$  and  $f$  are computed using Equations (52) and (53) presented in Section V.

e. Gas Model

Most of the heat transfer calculations presented in this section are for air in chemical equilibrium for an ideal gas. However, computations for a frozen flow are shown at the enthalpy for peak turbulent heating ( $V_\infty = 18,700$  fps). Since equilibrium flow implies infinite reaction rates and frozen flow zero reactions, differences in heating rates for these conditions are indicative of the maximum influence of reaction rates on turbulent heating.

1) Chemical Equilibrium

The turbulent heat transfer estimates for equilibrium flows were obtained using the  $\rho_r \mu_r$  program described in Volume III. The diffusion parameter  $\mathcal{L}$  is computed from Equation (21), and the stagnation reference viscosity  $\mu_0$  from Equation (19). Other thermodynamic and transport properties are essentially the same as those presented in Reference 16.

2) Frozen Flow

For this case, the gas is assumed to be frozen at the stagnation point composition. This composition and the corresponding thermodynamic and transport properties are computed using the equations presented in Reference 16. The stagnation point gas composition was obtained from Reference 17. The flow properties on the wing surface are based on an isentropic expansion.

For the range of temperatures considered, the vibrational energy level of the diatomic molecules can be considered to be proportional to the translational and rotational energy levels. This approximation greatly simplifies computations since the specific heats  $c_p$  and  $c_v$  are then constant with temperature.

By definition of frozen flow, no chemical recombination of atoms occurs. Consequently, the energy absorbed in dissociation must be considered unavailable in computing the total enthalpy of the flow. For the present case, the total enthalpy of the flow at the boundary layer edge is reduced by dissociation to about 47 percent of the free-stream value at  $V_\infty = 18,700$  fps. The resulting decrease in adiabatic wall enthalpy causes a substantial reduction in heating rates. The frozen flow adiabatic wall enthalpy is given by:

$$i_{aw} = r i_e + (1 - r) i_e = .47 r i_\infty + (1 - r) i_e \quad (81)$$

A second frozen-flow heat-transfer calculation was made that differs from that described previously only in that the adiabatic wall enthalpy is based on the total enthalpy of the free-stream flow as follows:

$$i_{aw} = r i_{\infty} + (1 - r) i_e \quad (82)$$

The second approach is presented to furnish an estimate of the influence of sudden recombination of atoms or heating. A noncatalytic wall is assumed in all cases.

### 3) Ideal Gas

Since the gas composition is assumed to be frozen in the free-stream state, the ideal gas case is a special type of frozen flow. Viscosities are computed using Sutherland's law. The usual thermodynamic parameters for low temperature air given below were assumed.

$$\gamma = 1.4$$

$$c_p = 6006 \text{ ft}^2/\text{sec}^2 - ^\circ\text{R}$$

$$R = 1716 \text{ ft}^2/\text{sec}^2 - ^\circ\text{R}$$

$$Z = 1.0$$

## 3. BLUNTNES AND REAL GAS EFFECTS

Bluntness effects on the Stanton number along the wing centerline are illustrated in Figure 12. At the highest velocity considered, the influence of bluntness is seen to extend only about 2 diameters downstream of the nose cap. At lower velocities and altitudes, the boundary layer displacement thickness is smaller; consequently, bluntness effects extend much further downstream. The sharp body estimates in computing the blunt body heating rates are based on local velocities and enthalpies for a sharp wing, but are adjusted to account for bluntness effects on local pressure.

Real gas effects are illustrated in Figure 13 which shows Stanton numbers for equilibrium, frozen, and ideal gas flows, all based on normal-shock theory (see Section VI). The frozen flow estimates are seen to be substantially lower than the equilibrium values, even when the adiabatic wall enthalpy is based on the free-stream total enthalpy.

The comparisons shown in Figure 13 are unrealistic in that the frozen flow composition applies only to the flow originating at the stagnation point. A more meaningful comparison is given in Figure 14, which shows the blunt body estimates obtained using Equation (74). The frozen flow composition is assumed in computing the normal-shock

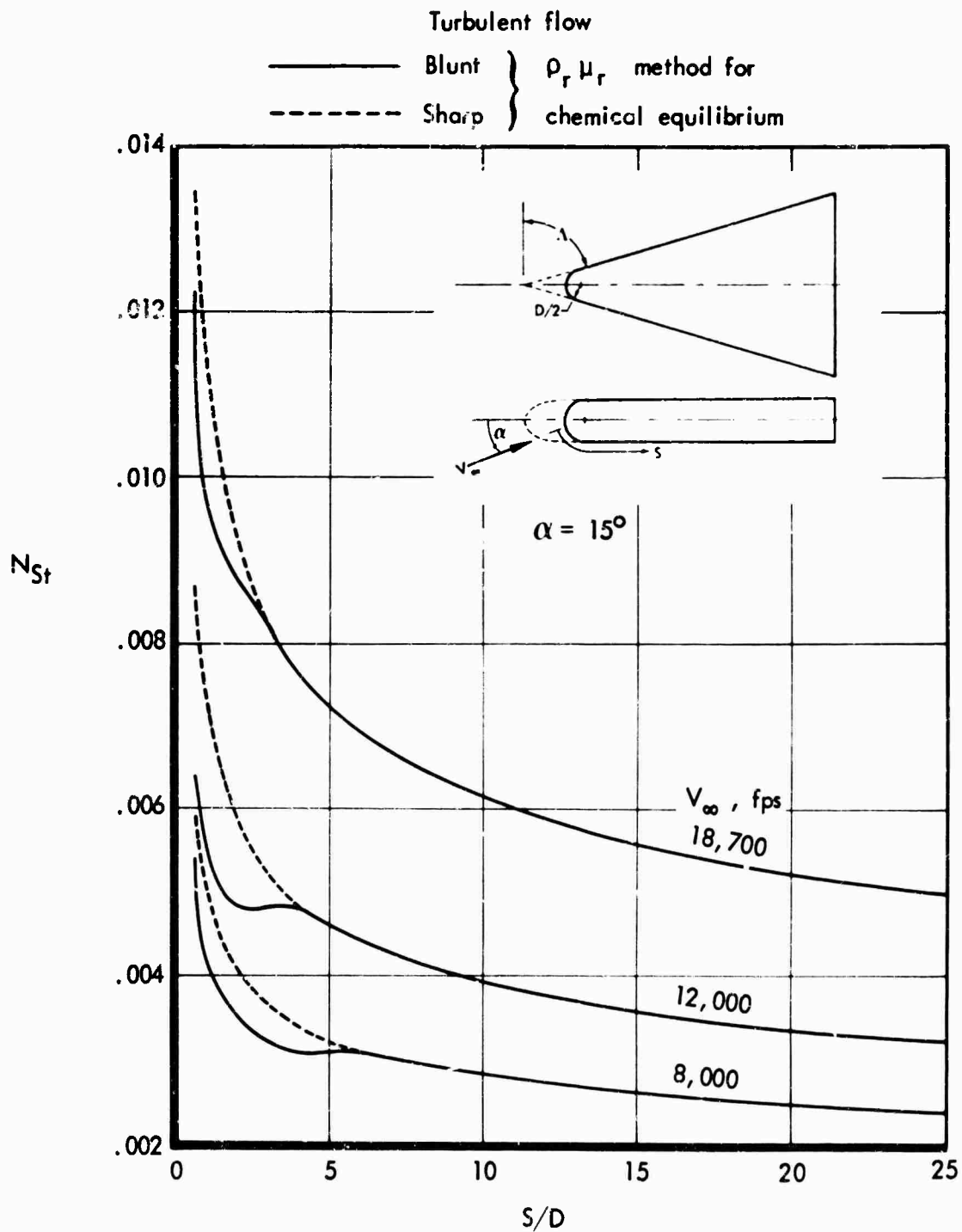


Figure 12: NOSE BLUNTNESS EFFECT ON DELTA WING CENTERLINE STANTON NUMBER

Normal-shock method

- Chemical equilibrium
- - - - - Ideal gas,  $\gamma = 1.4$
- · - · - Frozen flow

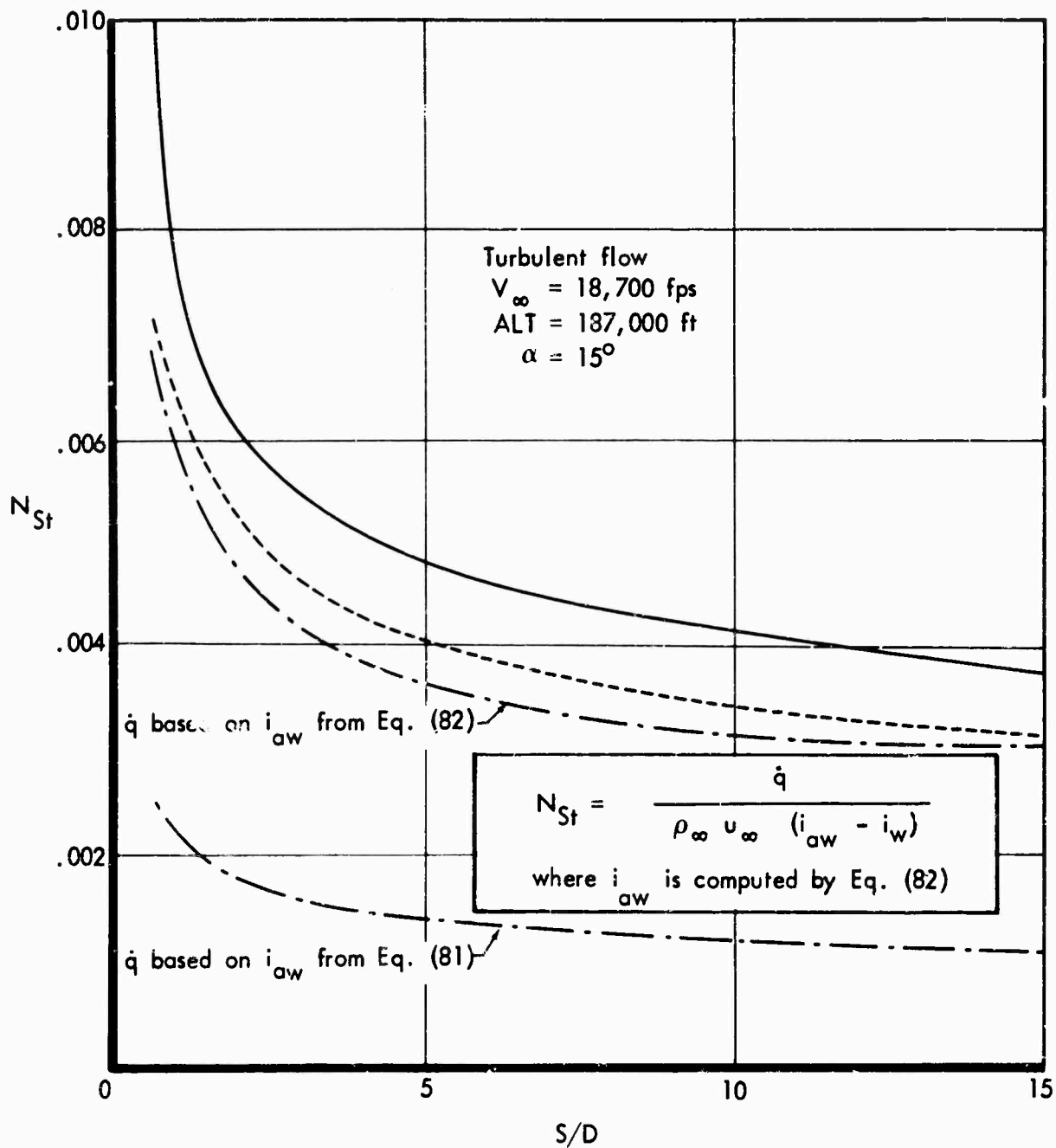


Figure 13: REAL-GAS EFFECT ON DELTA-WING CENTERLINE STANTON NUMBER USING NORMAL-SHOCK METHOD

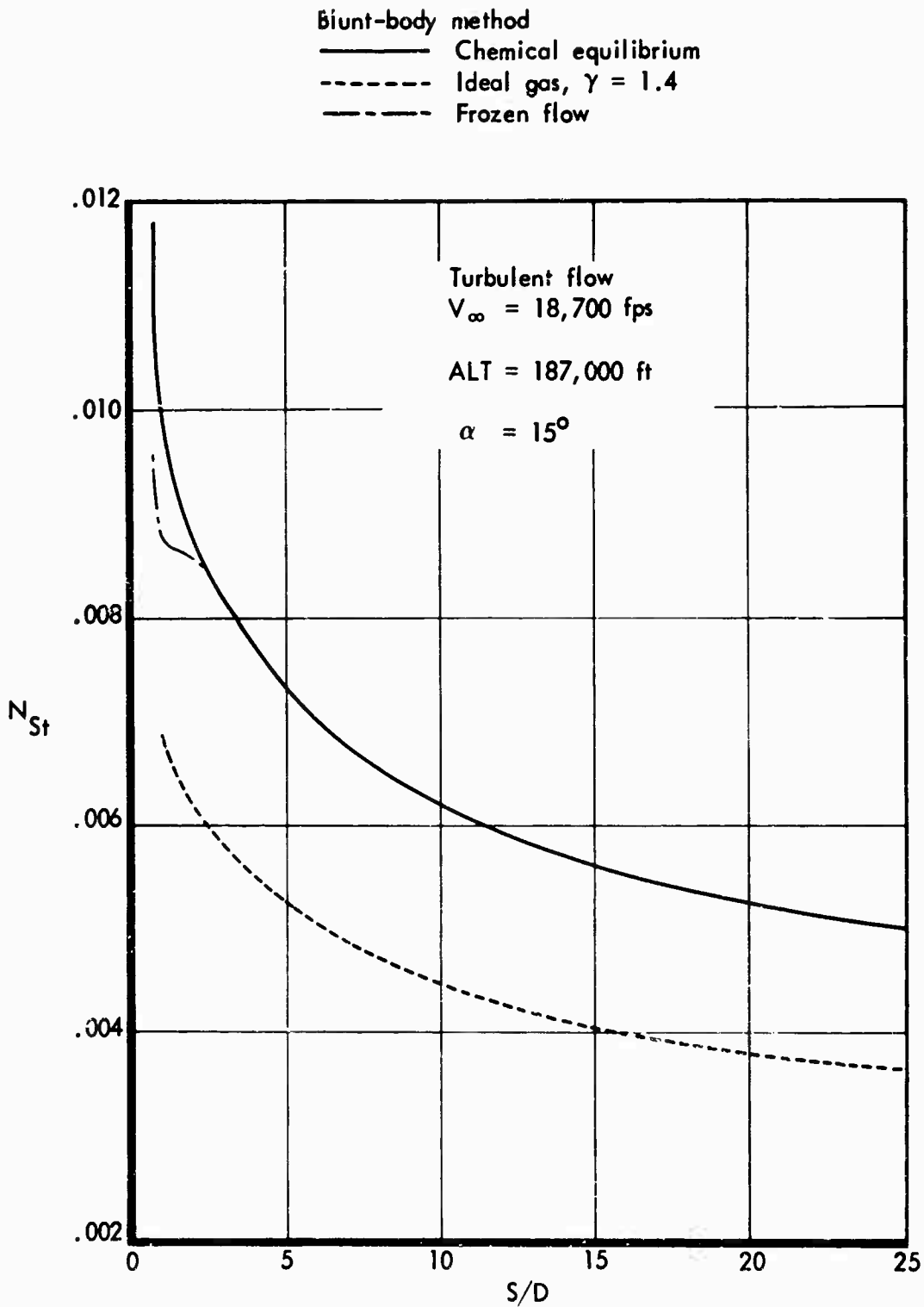


Figure 14: REAL-GAS EFFECT ON DELTA-WING CENTERLINE STANTON NUMBER USING BLUNT-BODY METHOD

values, and equilibrium flow is used in computing the sharp wing heating rates. It is seen that for this case reaction rates influence heating only near the nose cap. The ideal-gas Stanton numbers are about 40 percent lower than the corresponding equilibrium values.

#### 4. EXTRAPOLATION TO FLIGHT

At this time no test facility except hypersonic gun ranges, is capable of duplicating hypersonic flight conditions for speeds greater than about 10,000 feet per second. Except for shock tubes, the total enthalpy is less than high-speed flight. Shock tubes are capable of simulating enthalpy but are limited to low Mach numbers. For this reason, empirical methods alone cannot be relied upon to provide accurate heat transfer predictions for hypersonic flight. However, analytical methods alone are not adequate for predicting heating on realistic aerodynamic configurations unless supported by test data for that specific configuration. It therefore becomes necessary to interpret test data obtained from ground facilities in such a way that these data can be reflected in predictions for flight. One approach for making this interpretation is to extrapolate these data to flight conditions using analytical methods. In performing this extrapolation, it is convenient, whenever possible, to normalize Stanton numbers with respect to some reference condition such that the normalized Stanton numbers are not greatly dependent on flow conditions. The reference condition selected for this analysis is the stagnation line of an infinite cylinder of one foot diameter and a sweep angle of 60 degrees. The reference Stanton numbers for the flight path being considered is presented in Figure 15 for both equilibrium and ideal-gas flows.

The Stanton number ratios at the wing centerline are shown in Figure 16. Similar comparisons for the leading edge stagnation line and the lower-surface leading-edge tangent lines are presented in Figure 17. Extrapolation factors for two typical wind-tunnel test conditions are shown in Figure 18. The good simulation of Stanton number ratios for the stagnation line is not surprising since the reference Stanton number is also for the stagnation line but at a different sweep angle. However, significant differences in Stanton number ratios are noted for the delta wing centerline, particularly for Arnold center tunnel B. These deviations are due to differences in local Mach number, enthalpy level, and the ratio of the wall enthalpy to the total enthalpy.

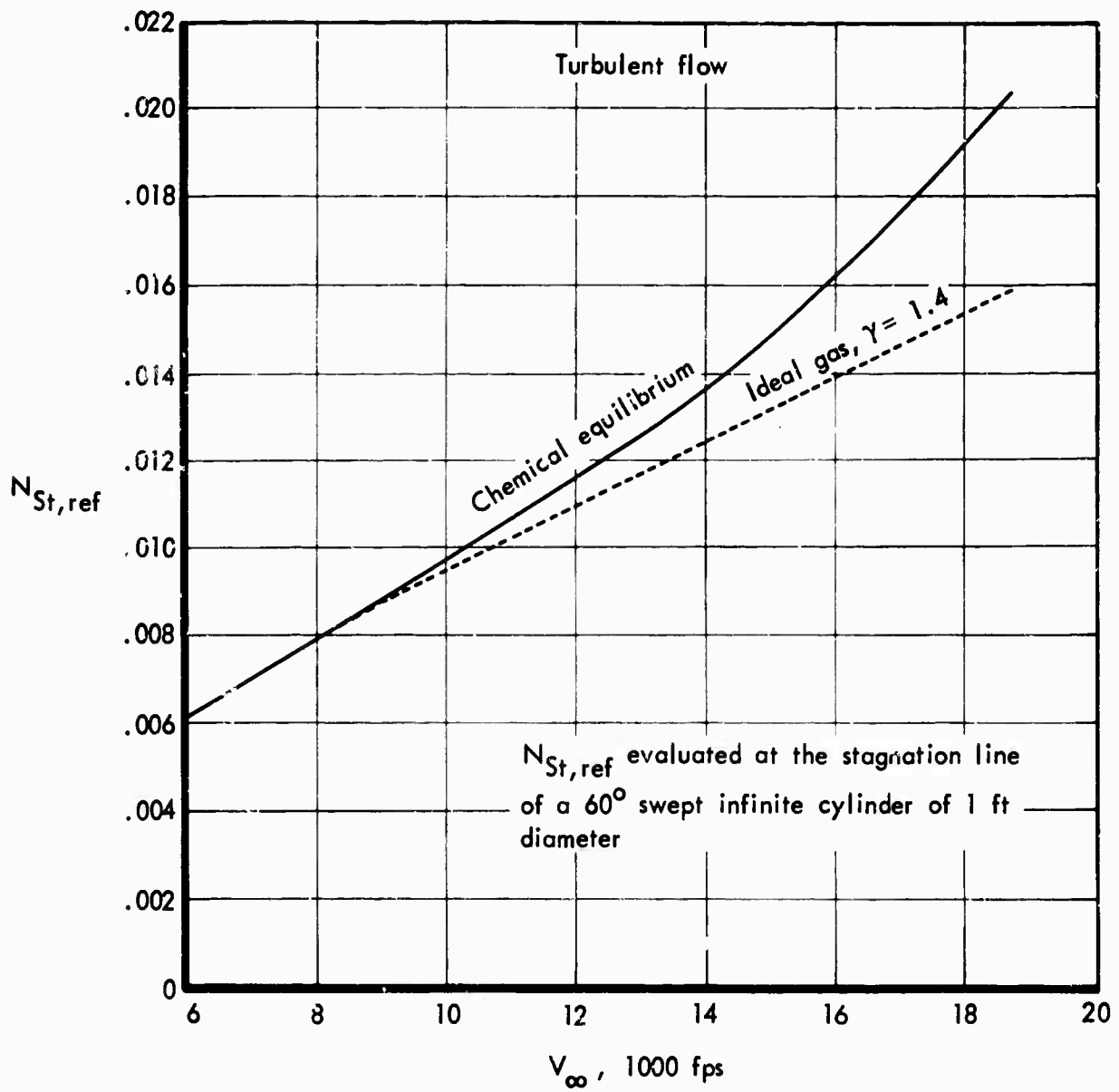


Figure 15: REAL-GAS EFFECT ON REFERENCE STANTON NUMBER

Turbulent flow

————— Chemical equilibrium

..... Ideal gas,  $\gamma = 1.4$

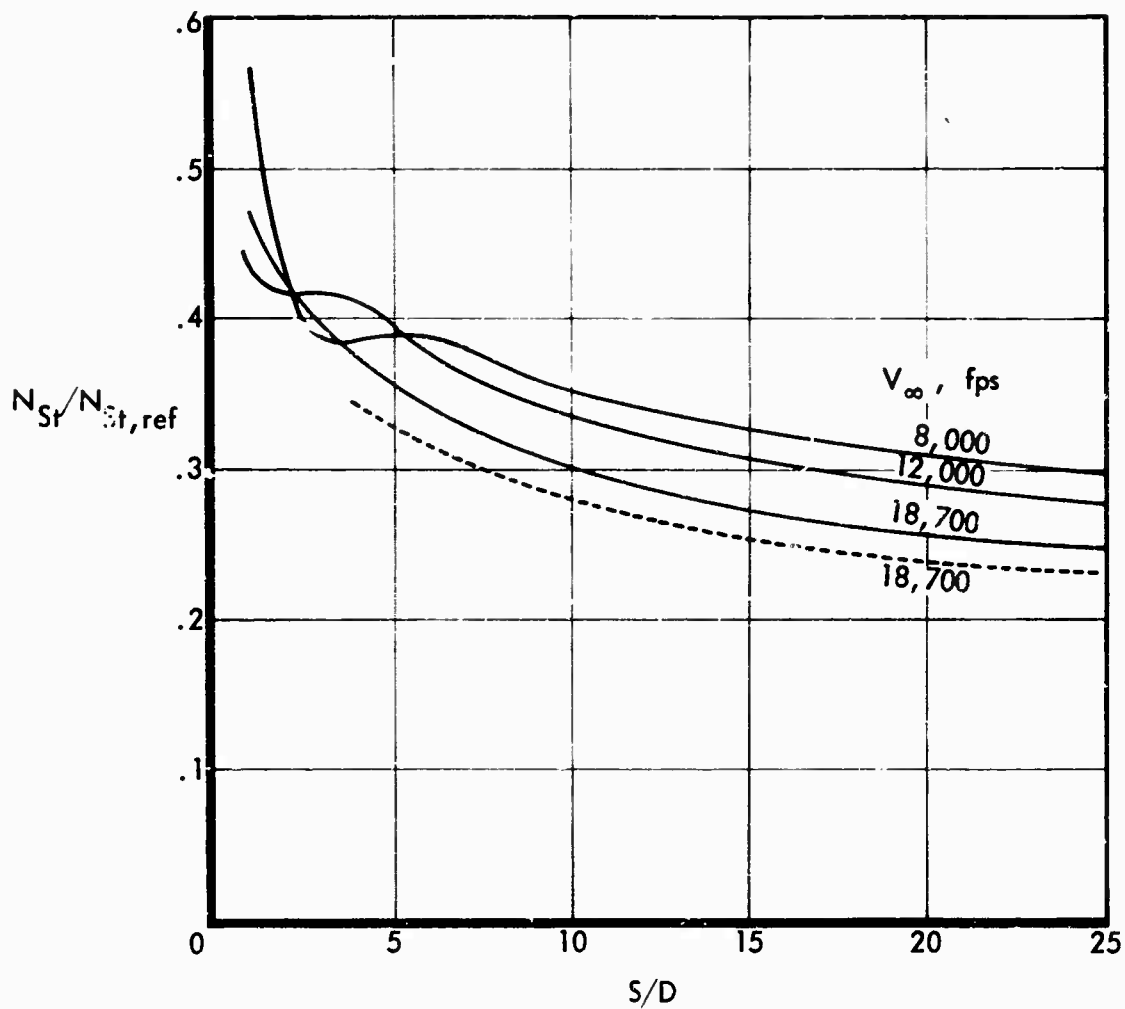
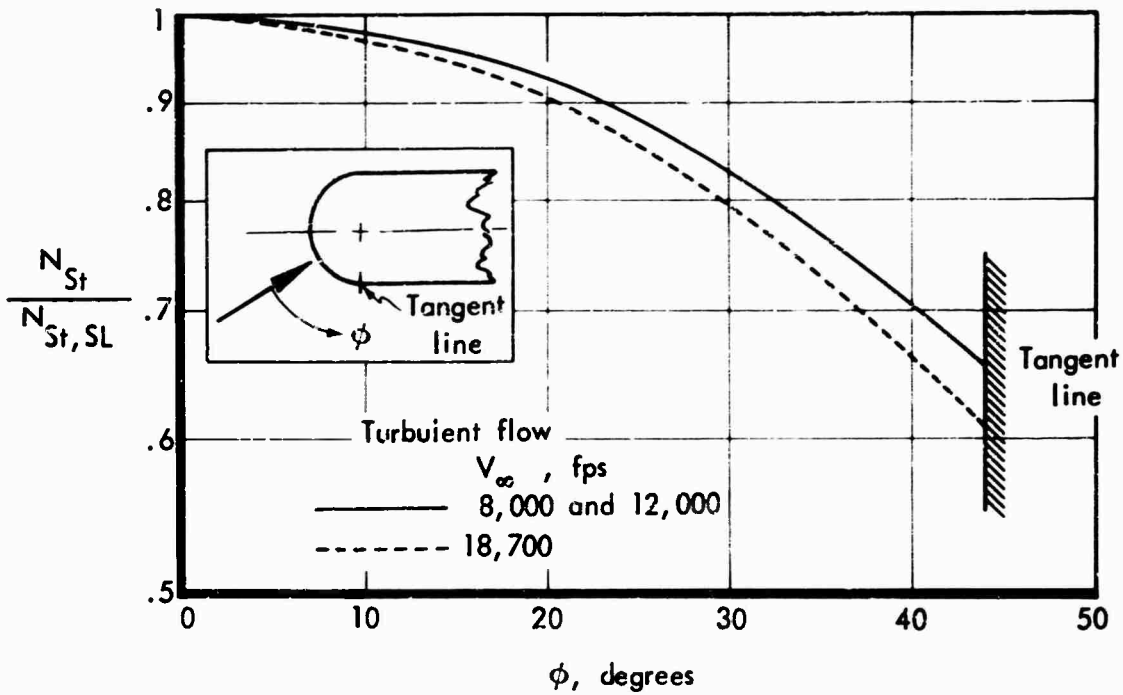
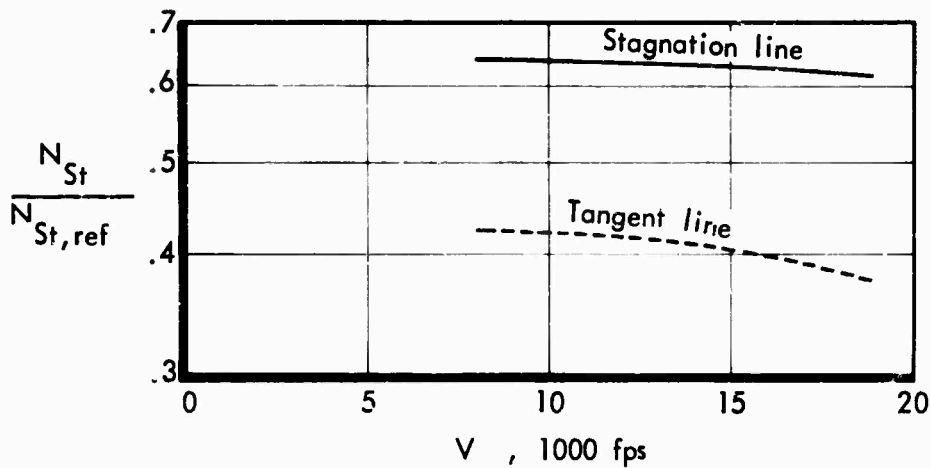


Figure 16: REAL-GAS EFFECT ON DELTA WING CENTERLINE STANTON NUMBER RATIOS

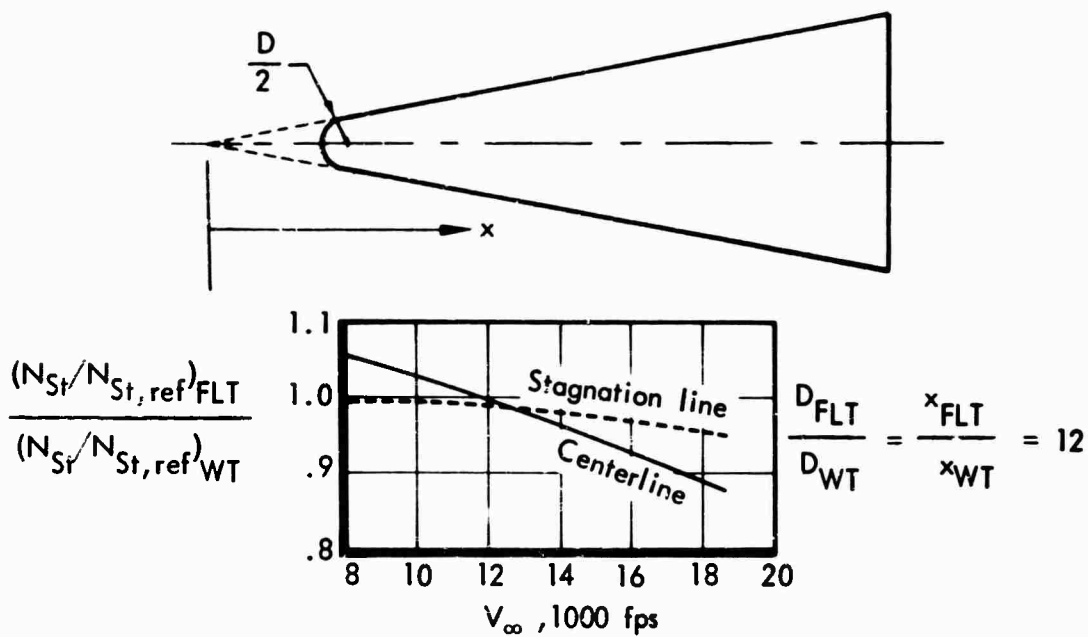


a) Leading Edge Stanton Number Distribution

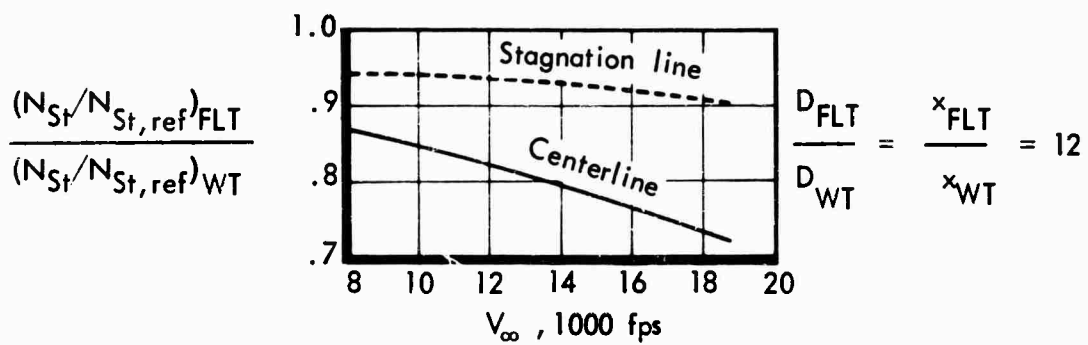


b) Stanton Numbers on the Leading Edge Stagnation Line and Tangent Line

Figure 17: STANTON NUMBER RATIOS ON THE CYLINDRICAL LEADING EDGE OF A  $75^\circ$ -SWEEPED BLUNT DELTA WING AT  $\alpha = 15^\circ$



a) AC-B Tunnel,  $M_\infty = 7$ ,  $P_\infty = 48.6$  psf,  $I_\infty = 6.3 \times 10^6$  ft<sup>2</sup>/sec<sup>2</sup>



b) CAL Shock Tunnel,  $M_\infty = 7.2$ ,  $P_\infty = 414$  psf,  $I_\infty = 3.41 \times 10^8$  ft<sup>2</sup>/sec<sup>2</sup>

Figure 18: TURBULENT EXTRAPOLATION FACTORS ON A 75°-SWEPT BLUNT DELTA WING

## SECTION IX

### CONCLUDING REMARKS

The  $\rho_r \mu_r$  method for estimating turbulent heating rates is well substantiated by experimental data obtained on several body shapes and for a wide range of test conditions. In particular, effects of local Mach number, wall cooling ratio ( $I_e/i_w$ ), three-dimensional flow, and streamwise pressure gradients predicted by this method are in excellent agreement with experimental trends. Similarly, the method for estimating nose bluntness effects described in Section VII, in general, furnishes good agreement with available heat transfer data.

Methods for predicting real-gas effects are not as well established. The combination of high pressures and temperatures required to obtain a highly dissociated turbulent flow is difficult to achieve in ground facilities; consequently, very little data are available for turbulent flows with significant levels of dissociation and high Mach numbers.

Whenever possible, it is recommended that the  $\rho_r \mu_r$  computer program described in Volume III be used for calculating convective heat transfer rates. However, if computations must be made manually, the simplified equations presented in Appendix B are recommended. In most cases, the simplified equations provide heat transfer estimates within a few percent of the complete equations. Handbook methods presented in Reference 5 will also provide heating estimates that are in good agreement with the  $\rho_r \mu_r$  computer program except for delta wing surfaces. Significant discrepancies in heating estimates on sharp delta wings can occur because of differences in methods of determining three-dimensional parameters.

The purpose of developing the turbulent nonsimilar method was to furnish a basis for evaluating the profile parameters appearing in the equations and to substantiate the method presented in Section VI for estimating effects of wall temperature gradients. Unfortunately, it was impossible to complete these studies during the present investigation. Numerical instabilities often developed when pressure gradients were imposed on the flow. Although measures were usually found for eliminating these instabilities, they resulted in substantial increases in computing time.

In spite of these difficulties, the turbulent nonsimilar method is believed to represent a new and promising approach in treating turbulent flows. This approach offers several advantages over previous methods. Empirical correlations are used only in defining Reynolds stresses, and no assumptions regarding velocity profiles or shear distributions are required. Since the flow equations are solved in partial differential form, no coordinate transformations are required. Such transformations usually impose restrictions on boundary conditions and flow similarity. Skin-friction coefficients and heat-transfer rates obtained using this method are in good agreement with experimental data over a wide range of test conditions.

## APPENDIX A

### DERIVATION OF THE $\rho_r \mu_r$ METHOD

The derivation of the  $\rho_r \mu_r$  equations presented in this appendix is based on a solution of the boundary layer energy integral equation. A similar derivation based on a solution of the momentum integral equation is presented in Appendix B of Reference 2. The present derivation is given in the following parts:

1. Derivation of a general form of the boundary layer energy integral equation.
2. Transformation and solution of the energy integral equation.
3. Solution of the momentum integral equation.
4. Evaluation of laminar boundary layer parameters.
5. Combined laminar and turbulent method.

A simplified version for making hand calculations is presented in Appendix B and the IBM 7094 digital computer program using the equations presented in this appendix is described in Volume III.

The correlations given in part 4 of this appendix are the same as those presented in Reference 1, but differ from those of Reference 2. However, differences in heating rates computed using the present correlations and those of Reference 2 are small.

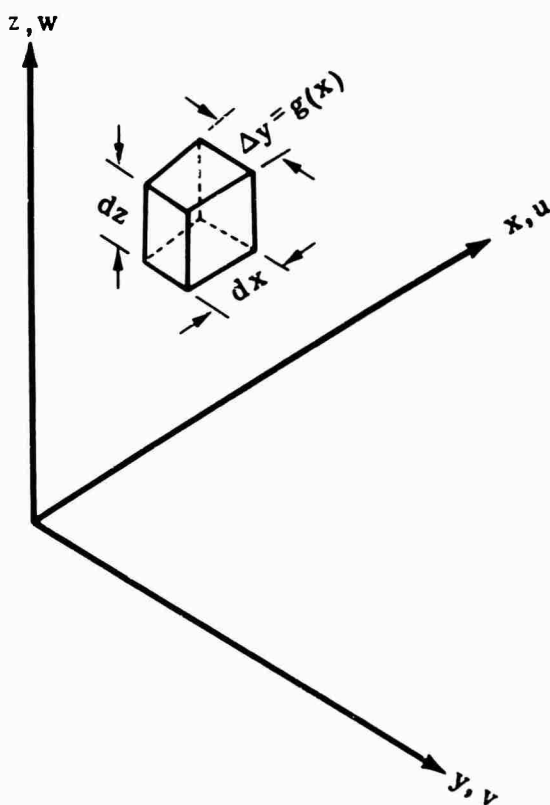
#### 1. DERIVATION OF THE ENERGY INTEGRAL EQUATION

This derivation is restricted to the vicinity of a plane of symmetry as well as by the usual boundary layer assumptions. The mass and energy conservation equations for boundary layer flows are given by Equations (A-1) and (A-2), respectively:

$$\frac{1}{g} \frac{\partial \rho u g}{\partial x} + \frac{\partial \rho v}{\partial y} + \frac{\partial \rho w}{\partial z} = 0 \quad (\text{A-1})$$

$$\rho u \frac{\partial I}{\partial x} + \rho v \frac{\partial I}{\partial y} + \rho w \frac{\partial I}{\partial z} = \frac{\partial \dot{q}}{\partial z} + \frac{\partial (u\tau)}{\partial z} \quad (\text{A-2})$$

The corresponding control volume is shown in the following sketch:



The length elements in  $x$  and  $z$  are unity. However, the length element in  $y$  is determined by the function  $\Delta y = g(x)$ , which remains arbitrary (subject to the restriction that  $dg/dx$  remains finite). Later it will be seen that in most cases the most convenient choice of  $g$  is dependent on the geometry of the body under consideration. The surface  $y = 0$  is by definition a line of symmetry, hence  $v$ , but not necessarily  $\partial v/\partial y$ , is zero when  $y = 0$ . Also, it should be noted that for turbulent flows the flow parameters appearing in Equations (A-1) and (A-2) are averaged with respect to time. For turbulent flows,  $\tau$  represents the effective shear stress including the Reynolds stress, and  $\dot{q}$  represents a corresponding effective heat flux.

The velocity component normal to the body,  $w$ , is found by integrating Equation (A-1) with respect to  $z$ :

$$w = -\frac{1}{\rho} \int_0^z \left[ \frac{1}{g} \frac{\partial \rho u g}{\partial x} - \frac{\partial \rho v}{\partial y} \right] dz - \frac{\rho_w w_w}{\rho} \tag{A-3}$$

Using Equation (A-3), and assuming that  $w_w = 0$ , Equation (A-2) can be written:

$$\rho u \frac{\partial I}{\partial x} + \rho v \frac{\partial I}{\partial y} - \frac{\partial I}{\partial z} \int_0^z \left[ \frac{1}{g} \frac{\partial \rho u g}{\partial x} + \frac{\partial \rho v}{\partial y} \right] dz = \frac{\partial \dot{q}}{\partial z} + \frac{\partial (u\tau)}{\partial z} \quad (\text{A-4})$$

In order to obtain the boundary layer momentum integral, Equation (A-4) is integrated from the wall to some arbitrary location ( $z = h$ ) outside of the boundary layer. Neglecting external vorticity,  $\dot{q}_{z=h} = \tau_{z=h} = 0$ , the momentum integral becomes:

$$\int_0^h \left[ \rho u \frac{\partial I}{\partial x} + \rho v \frac{\partial I}{\partial y} \right] dz - \int_0^h \frac{\partial I}{\partial z} \int_0^z \left[ \frac{1}{g} \frac{\partial \rho u g}{\partial x} + \frac{\partial (\rho v)}{\partial y} \right] dz dz = -\dot{q}_{z=0} \quad (\text{A-5})$$

Integrating the second term by parts and rearranging, Equation (A-5) can be expressed:

$$\dot{q}_{z=0} \equiv \dot{q}_w = \frac{1}{g} \frac{\partial}{\partial x} \int_0^h \rho u g (I_e - I) dz + \frac{\partial}{\partial y} \int_0^h \rho v (I_e - I) dz \quad (\text{A-6})$$

Since this analysis is restricted to lines of symmetry, it can be easily shown that:

$$\frac{\partial \rho_c}{\partial y} = 0, \quad \frac{\partial \left( \frac{v}{v_c} \right)}{\partial y} = 0$$

and

$$\frac{\partial (i_{aw} - i_w)}{\partial y} = 0$$

In the present analysis it is further assumed that:

$$\frac{\partial (i_{aw} - i_w)}{\partial x} = 0$$

The influence of wall temperature gradients on heat transfer is treated separately in Section VI.

Thus, Equation (A-6) can now be expressed in terms of the heat transfer coefficient,  $H$ , as follows:

$$\begin{aligned} \frac{\dot{q}_w}{\rho_e u_e (i_{aw} - i_w)} &= \frac{H}{\rho_e u_e} = \frac{\partial}{\partial x} \int_0^h \frac{\rho u}{\rho_e u_e} \left[ \frac{I_e - I}{i_{aw} - i_w} \right] dz \\ &+ \frac{1}{\rho_e u_e g} \frac{\partial \rho_c u_e g}{\partial x} \int_0^h \frac{\rho u}{\rho_e u_e} \left[ \frac{I_e - I}{i_{aw} - i_w} \right] dz \\ &+ \frac{\partial v_e / \partial y}{u_e} \int_0^h \frac{\rho v}{\rho_e v_e} \left[ \frac{I_e - I}{i_{aw} - i_w} \right] dz \end{aligned} \quad (A-7)$$

Now, introducing the boundary layer thickness parameters, energy thickness:

$$Q \equiv \int_0^h \frac{\rho u}{\rho_e u_e} \left[ \frac{I_e - I}{i_{aw} - i_w} \right] dz \quad (A-8)$$

and the crossflow energy thickness ratio:

$$\bar{\epsilon} \equiv \frac{1}{Q} \int_0^h \frac{\rho v}{\rho_e v_e} \left[ \frac{I_e - I}{i_{aw} - i_w} \right] dz$$

Equation (A-7) now reduces to:

$$\frac{H}{\rho_e u_e} = \frac{\partial Q}{\partial x} + Q \left[ \frac{1}{u_e} \frac{\partial u_e}{\partial x} + \frac{1}{\rho_e} \frac{\partial \rho_c}{\partial x} + \frac{1}{g} \frac{\partial g}{\partial x} + \bar{\epsilon} \frac{\partial v_e / \partial y}{u_e} \right] \quad (A-9)$$

Note that  $\bar{\epsilon}$  and  $\partial v_e / \partial y$  are determined by the definition of  $g$ , which is still arbitrary. Since results obtained from Equation (A-9) are independent of this definition, the selection is made solely on the basis of convenience in evaluating the appropriate flow parameters.

It is seen from Equation (A-8) that an exact evaluation of  $\bar{\epsilon}$  requires a solution of both the streamwise and crossflow velocity profiles. Such solutions are available only for laminar flow over simple shapes. It is therefore desirable to define  $g$  in such a way that  $\bar{\epsilon}$  and  $\partial v_e / \partial y$  reflect only the influence of crossflow pressure gradients. For this case  $g$  reflects only the streamline divergence due to body geometry. In the absence of a more exact approach,  $g$  can be assumed to be proportional to the body radius of curvature,  $r$ , normal to the streamline. In order to be consistent with the

most common symbology,  $r$  is used in place of  $g$  in the following analysis. Also, the streamline divergence due to crossflow pressure gradients is denoted by  $f$ , where  $f$  is defined by:

$$\frac{1}{f} \frac{\partial f}{\partial x} \equiv \frac{1}{u_e} \frac{\partial v_e}{\partial y} \quad (\text{A-10})$$

Using Equation (A-10), Equation (A-9) can now be expressed as:

$$H = \frac{1}{rf\bar{\epsilon}} \frac{\partial}{\partial x} (\rho_e u_e r f \bar{\epsilon} Q) \quad (\text{A-11})$$

## 2. TRANSFORMATION AND SOLUTION OF THE ENERGY INTEGRAL EQUATION

### a. Transformation

In order to obtain a more useful form of the energy equation, a modified Stewartson transformation suggested by Mager (Reference 3) is adopted in which:

$$\begin{aligned} X &= \int_0^x F \frac{\rho_r \mu_r}{\rho_o \mu_o} dx & V &= \frac{v}{F} \\ Y &= y & \bar{I} &= \frac{I}{F^2} \\ Z &= F \int_0^z \frac{\rho}{\rho_o} dz & \bar{i}_{aw} &= \frac{i_{aw}}{F^2} \\ U &= \frac{u}{F} & \bar{i}_w &= \frac{i_w}{F^2} \end{aligned} \quad (\text{A-12})$$

The stagnation values of density and viscosity,  $\rho_o$  and  $\mu_o$ , are required to be constant, and  $F$  is an unspecified function of  $X$  only. With these definitions, the energy thickness and heat transfer coefficient in the transformed coordinate system are, respectively:

$$\bar{Q} = \int_0^h \frac{U}{U_e} \frac{\bar{I}_e - \bar{I}}{\bar{i}_{aw} - \bar{i}_w} dZ = F \frac{\rho_e}{\rho_o} Q$$

$$\bar{H} = \frac{1}{F} \frac{\rho_o \mu_o}{\rho_r \mu_r} H \quad (A-13)$$

$\bar{\epsilon}$ ,  $r$ , and  $f$  are unchanged by the transformation. The transformed energy equation now becomes:

$$\bar{H} = \frac{1}{rf\bar{\epsilon}} \frac{\partial}{\partial X} \left( \rho_o U_e r f \bar{\epsilon} \bar{Q} \right) \quad (A-14)$$

b. Solution of the Transformed Integral Equation

In Appendix B of Reference 2, the transformed momentum integral equation was solved by assuming a transformed Blasius shear law given below:

$$\frac{\bar{\tau}_w}{\rho_o U_e^2} = \frac{C_m}{(\rho_o U_e^{\oplus} / \mu_o)^{1/m}} \quad (A-15)$$

The exponent  $m$  is unity for laminar flows, and approximately 4 for turbulent boundary layers. However, by leaving  $m$  unspecified the following analysis is valid for both types of flow.

Assuming unit Prandtl number and, neglecting the effects of streamwise pressure gradients, the enthalpy can be related to velocity by the well-known Crocco energy relationship given by:

$$\frac{I - i_w}{I_e - i_w} = \frac{u}{u_e}$$

For this case it is easily demonstrated that the following expression relating heat transfer coefficient to energy thickness corresponds exactly to Equation (A-15):

$$\bar{H} = C_m \frac{\rho_o U_e}{(\rho_o U_e \bar{Q} / \mu_o)^{1/m}} \quad (\text{A-16})$$

The form of Equation (A-16) is retained in this analysis, but the constant  $C_m$  is replaced by  $C_Q$ . This substitution is necessary to account for differences in the constant resulting from errors introduced by using the Crocco approximation.

Using Equation (A-16), but with the new constant, Equation (A-14) now becomes:

$$C_Q (\rho_o U_e)^{(m-1)/m} \mu_o^{1/m} \bar{Q}^{-1/m} = \frac{1}{\text{rf} \bar{\epsilon}} \frac{\partial}{\partial X} (\rho_o U_e \text{rf} \bar{\epsilon} \bar{Q}) \quad (\text{A-17})$$

Equation (A-17) can be solved for  $(\rho_o U_e \bar{Q})$  by multiplying both sides by

$$(\rho_o U_e \bar{Q})^{\frac{1}{m}} (\text{rf} \bar{\epsilon})^{\frac{m+1}{m}},$$

rearranging, and integrating both sides with respect to  $X$ . Using the boundary condition that either  $U_e = 0$  or  $\bar{Q} = 0$  at  $X = 0$ , the solution is given by:

$$(\rho_o U_e \bar{Q})^{1/m} = \frac{\left[ \int_0^X \frac{m+1}{m} C_Q \rho_o U_e \mu_o^{1/m} (\text{rf} \bar{\epsilon})^{(m+1)/m} dX \right]^{1/(m+1)}}{(\text{rf} \bar{\epsilon})^{1/m}} \quad (\text{A-18})$$

Substituting Equation (A-18) into (A-16):

$$\bar{H} = \frac{C_Q \rho_o U_e (\text{rf} \bar{\epsilon})^{1/m} \mu_o^{1/m}}{\left[ \int_0^X \frac{m+1}{m} C_Q \rho_o U_e \mu_o^{1/m} (\text{rf} \bar{\epsilon})^{(m+1)/m} dX \right]^{1/(m+1)}} \quad (\text{A-19})$$

In the untransformed physical plane, Equation (A-19) is:

$$H = \frac{C_Q \rho_r \mu_r u_e \mu_o^{(1-m)/m} (rf\bar{\epsilon})^{1/m}}{\left[ \int_0^x \frac{m+1}{m} C_Q \rho_r \mu_r u_e (rf\bar{\epsilon})^{(m+1)/m} dx \right]^{1/(m+1)}} \quad (A-20)$$

Neither  $\rho_o$  nor  $F$  appear in this equation, and their definitions are therefore immaterial. It was stated earlier that  $\mu_o$  was independent of  $x$ . The preceding solution is valid only if  $m$  is constant with  $x$ . If  $C_Q$  is also assumed to be independent of  $x$ , Equation (A-20) reduces to:

$$H = \frac{\left(\frac{m}{m+1}\right)^{1/(m+1)} (C_Q)^{m/(m+1)} (\mu_o)^{\frac{1-m}{1+m}} (\rho_r \mu_r u_e)^{m/(m+1)}}{\left[ \frac{1}{\rho_r \mu_r u_e (rf\bar{\epsilon})^{(m+1)/m}} \int_0^x \rho_r \mu_r u_e (rf\bar{\epsilon})^{(m+1)/m} dx \right]^{1/(m+1)}} \quad (A-21)$$

It is convenient to express  $C_Q$  and  $m$  using the following:

$$\left(\frac{m}{m+1}\right)^{\frac{1}{m+1}} (C_Q)^{\frac{m}{m+1}} = C_{FP} J^{\frac{1}{m+1}}$$

where  $C_{FP}$  is the flat plate value of

$$\left(\frac{m}{m+1}\right)^{\frac{1}{m+1}} C_Q^{\frac{m}{m+1}}$$

and  $J$  reflects the influence of streamwise pressure gradients. Correlations of exact laminar boundary layer solutions show that  $C_{FP}$  can be expressed by:

$$C_{FP} = .332 \frac{\mathcal{L}}{F_{Pr}}$$

Based on this result, the following expression is assumed to apply to both laminar and turbulent flows:

$$\left(\frac{m}{m+1} C_Q\right)^{\frac{m}{m+1}} = \frac{C_x \mathcal{L} J^{\frac{m}{m+1}}}{F_{Pr}} \quad (A-22)$$

where  $C_x$  is approximately 0.332 for laminar flow, and is a constant to be specified later for turbulent flow. Using Equation (A-22),  $H$  can now be expressed in the more familiar form shown below:

$$H = \frac{C_x \mathcal{L} \mu_o}{F \text{Pr}^{x_{\text{eq}}}} \left( \frac{\rho_r \mu_r u_e x_{\text{eq}}}{\mu_o^2} \right)^{\frac{m}{m+1}} \quad (\text{A-23})$$

where  $x_{\text{eq}}$  is an equivalent flat plate length parameter defined by:

$$x_{\text{eq}} = \frac{1}{J \rho_r \mu_r u_e (\text{rf} \bar{\epsilon})^{(m+1)/m}} \int_0^x \frac{\rho_r \mu_r u_e (\text{rf} \bar{\epsilon})^{(m+1)/m}}{\mu_o^2} dx \quad (\text{A-24})$$

Equations (A-23) and (A-24) are equivalent to the result reported in Appendix B of Reference 2 with one exception. The exponent  $\bar{\epsilon}$  in Equation (A-24) appears in place of the crossflow momentum thickness ratio,  $\bar{E}$ , in Reference 2, where:

$$\bar{E} = \frac{\int_0^h \frac{\rho v}{\rho_e v_e} \left( 1 - \frac{u}{u_e} \right) dz}{\int_0^h \frac{\rho u}{\rho_e u_e} \left( 1 - \frac{u}{u_e} \right) dz} \quad (\text{A-25})$$

If the Crocco energy relationship is assumed, it is easily seen that  $\bar{\epsilon}$  and  $\bar{E}$  are equal. Considering that approximate methods must be used in evaluating either  $\bar{\epsilon}$  or  $\bar{E}$ , particularly for turbulent flow, it appears reasonable to have the same approximations for both parameters. Accordingly,  $\bar{\epsilon}$  is replaced by  $\bar{E}$  in the following analysis in order to make the nomenclature consistent with that of previous publications (e. g. . References 1, 2, and 3).

### 3. SOLUTION OF THE MOMENTUM INTEGRAL EQUATION

The purpose of this derivation is to obtain expressions for momentum thickness and skin friction consistent with the heat transfer expression given by Equations (A-23) and (A-24).

The boundary layer momentum integral is given in Appendix B of Reference 2 by:

$$\frac{\tau_w}{\rho_e u_e^2} = \frac{\partial \theta}{\partial x} + \theta \left( \frac{2 + \delta^*/\theta}{u_e} \frac{\partial u_e}{\partial x} + \frac{1}{\rho_e} \frac{\partial \rho_e}{\partial x} + \frac{1}{r} \frac{\partial r}{\partial x} + \frac{\bar{E}}{f} \frac{\partial f}{\partial x} \right) \quad (\text{A-26})$$

where  $\theta$  is the boundary layer momentum thickness.

Equation (A-26) can be rearranged into a simple form similar to the energy integral expression given by Equation (A-11), giving:

$$\frac{\tau_w}{u_e} = \frac{1}{u_e^{A-1} r f \bar{E}} \frac{\partial}{\partial x} \left( \rho_e u_e^A r f \bar{E} \theta \right) \quad (\text{A-27})$$

where  $A = 2 + \delta^*/\theta$ .

Applying the Magari transformation defined by Equation (A-12), Equation (A-27) becomes:

$$\frac{\bar{\tau}_w}{U_e} = \frac{1}{U_e^{A-1} F^{A-1} r f \bar{E}} \frac{\partial}{\partial x} \left( \rho_e U_e^A F^{A-1} r f \bar{E} \bar{\Theta} \right) \quad (\text{A-28})$$

where

$$\bar{\tau}_w = \frac{\tau_w}{F^2} \left( \frac{\rho_o \mu_o}{\rho_r \mu_r} \right)$$

and

$$\bar{\Theta} = \int_0^h \left[ \frac{U}{U_e} - \left( \frac{U}{U_e} \right)^2 \right] dZ = F \frac{\rho_e}{\rho_o} \theta$$

By replacing the left side of Equation (A-28) with the transformed Blasius shear law, Equation (A-15), an expression for  $\bar{\Theta}$  is obtained in the same way as was  $\bar{Q}$  in part 2 of this appendix. The result is:

$$\bar{\Theta} = \frac{\left[ \int_0^X \frac{1}{m} C_m F^{A-1} \rho_o U_e^A \mu_o^{1/m} (r f \bar{E})^{\frac{m+1}{m}} dX \right]^{\frac{m}{m+1}}}{F \rho_o U_e r f \bar{E}} \quad (\text{A-29})$$

In untransformed physical coordinates, the equivalent expression for  $\theta$  is:

$$\theta = \frac{\left[ \int_0^{x_1} \frac{m+1}{m} C_m \rho_r \mu_r u_e^A \mu_o^{\frac{1-m}{m}} (rf\bar{E})^{\frac{m+1}{m}} dx \right]^{\frac{m}{m+1}}}{\rho_c u_e rf\bar{E}} \quad (A-30)$$

The momentum thickness is related to skin friction by the modified Blasius shear law given by Equation (A-15). The untransformed equivalent of Equation (A-15) is given by:

$$\frac{\tau_w}{u_e} = \frac{\rho_r \mu_r u_e}{\mu_o} \frac{C_m}{\left( \frac{\rho_e u_e \theta}{\mu_o} \right)^{1/m}} \quad (A-31)$$

Substituting Equation (A-30) into (A-31) gives:

$$\frac{\tau_w}{u_e} = \frac{C_m \mu_o^{\frac{1-m}{m}} \rho_r \mu_r u_e^{\frac{1}{m}} (rf\bar{E})^{\frac{1}{m}}}{\left[ \int_0^{x_1} \frac{m+1}{m} C_m \mu_o^{\frac{1-m}{m}} \rho_r \mu_r u_e^{\frac{A(m+1)-1}{m}} (rf\bar{E})^{\frac{m+1}{m}} dx \right]^{\frac{1}{m+1}}} \quad (A-32)$$

Assuming that  $C_m$  is independent of  $x$ , it can be expressed in a form similar to that for  $C_Q$  in Equation (A-22) by the following:

$$\left( \frac{m}{m+1} \right)^{\frac{1}{m+1}} (C_m)^{\frac{m}{m+1}} = C_x P^{\frac{1}{m+1}} \quad (A-33)$$

the profile parameter  $C_x$  is the flat plate value for

$$\left( \frac{m}{m+1} \right)^{\frac{1}{m+1}} \quad \text{and} \quad C_m^{\frac{m}{m+1}}$$

and  $P$  reflects the influence of streamwise pressure gradients.

Using Equation (A-33), Equation (A-32) can be reduced to a form similar to that for  $H$  given by Equation (A-23). The corresponding skin friction expression is:

$$\frac{\tau_w}{\rho_e u_e} = \frac{C_x \mu_o}{S_{eq}} (N_{R,r,S})^{\frac{m}{m+1}} \quad (A-34)$$

where:

$$N_{R,r,S} = \frac{\rho_r \mu_r u_e S_{eq}}{\mu_o^2} \quad (A-35)$$

and the skin-friction equivalent distance is defined by:

$$S_{eq} = \frac{\int_0^{x_1} \rho_r \mu_r u_e (rf\bar{E})^{\frac{m+1}{m}} dx}{P \rho_r \mu_r u_e (rf\bar{E})^{\frac{m+1}{m}}} \quad (A-36)$$

Using these definitions for  $N_{R,r,S}$  and  $S_{eq}$ , Equation (A-30) simplifies to:

$$\theta = \frac{m+1}{m} C_x \frac{\mu_o}{\rho_e u_e} (N_{R,r,S})^{\frac{m+1}{m}} \quad (A-37)$$

#### 4. EVALUATION OF LAMINAR BOUNDARY LAYER PARAMETERS

Exact solutions of the similarity form of the laminar boundary layer equations were used to evaluate the parameters appearing in Equations (A-23), (A-24) and (A-32). This was done in an orderly manner, beginning with two-dimensional constant-property constant-pressure flow, and progressing to the most complex conditions for which exact solutions are available. The evaluations determined from the simpler cases were retained or amplified in analyzing the more complex cases. Thus, the constant  $C_x$  for laminar flow is always taken to be 0.33206, the value given by Howarth in Reference 18 for incompressible flat plate flow. The effects of pressure gradients, wall cooling, etc., are accounted for in other terms of Equations (A-23) and (A-32).

In some cases, alternate definitions were possible. For example, the authors of References 19 and 20 incorporated (in effect) pressure gradients into the term  $\rho_r \mu_r$  appearing in Equation (A-23), while in the present formulation such effects appear in the heat transfer equivalent distance  $x_{eq}$ . The latter definition is to be preferred as the former cannot be made consistent with the results of Reference 12, which presents solutions for various pressure gradients, but with  $\rho\mu$  held constant. The definitions used here were adopted only after an examination of several possible alternatives. The criteria for selection were consistency between the results of the various special cases, conformity with physical considerations, accuracy, simplicity, and freedom from interdependencies.

a. General Considerations

As a matter of physical consistency, it is required that if the fluid properties  $\rho$  and  $\mu$  are constant through the boundary layer then the reference values of the fluid properties be equal to those constant values. This principle is extended to constant products as well, i. e. , it is required that when in a given numerical calculation (e. g. , References 12 and 21) the product of density and viscosity is held constant at some base value (usually the wall), then the reference density-viscosity product,  $\rho_r \mu_r$ , must also be equal to that base value. The functions  $F_{Pr}$  and  $\mathcal{L}$  are equal to 1.0 when  $\sigma$  and  $N_{Le}$  are equal to 1.0, and  $\mathcal{L} = 1.0$  for ideal gases. Also, in flat plate flow the equivalent distance is equal to the physical distance from the leading edge.

b. Two-Dimensional Flat Plate Flow

The special case of two-dimensional flat plate flow is examined first since the effect of fluid property variations within the boundary layer can be examined without the additional complexity of streamwise variations. For the case of constant fluid properties, the solutions of Howarth (Reference 18) show that  $m = 1$  and  $C_x = .332$ , so that Equation (A-23) becomes:

$$H = .332 \frac{\mathcal{L}}{F_{Pr}} \left( \frac{\rho_r \mu_r u_e}{x_{eq}} \right)^{\frac{1}{2}} \quad (A-38)$$

$$= .332 \frac{\mathcal{L}}{F_{Pr}} \left( \frac{\rho_c \mu_c u_e}{x} \right)^{\frac{1}{2}} \quad (A-39)$$

where Equation (A-39) follows from the principles stated in the preceding paragraph. For this special case, the only undetermined quantities are the Reynolds analogy factors  $\mathcal{L}$  and  $F_{Pr}$ . Note that the reference stagnation viscosity,  $\mu_0$ , no longer appears.

c. Reynolds Analogy Factors

Following the practice of Reference 19, for example, the Prandtl number effect is correlated in terms of  $\sigma$ , the partial Prandtl number for translation, rotation, and vibration. The Prandtl number effect on Reynolds analogy in flat plate flow, usually given as  $F_{Pr} = (\sigma)^{2/3}$  for constant  $\sigma$ , is somewhat better represented by  $\sigma \cdot 645$  as may be seen in Figure 19.

For variable Prandtl number there is an uncertainty as to which value should be used in correlating its effect. All solutions in the literature for which the Prandtl number is variable also involve variable  $\rho\mu$ , so that  $\rho_r\mu_r$  is not necessarily equal to  $\rho_e\mu_e$ . For such cases, it was found that the Prandtl number should be evaluated at the enthalpy and pressure corresponding to  $\rho_r\mu_r$ . This value of the Prandtl number is hereafter denoted as  $\sigma_r$ .

When the Prandtl number effect is correlated in terms of the partial Prandtl number, the effect of energy transport by diffusion must be treated separately. The first exact calculation of this effect is reported in Reference 19, wherein the expression:

$$\mathcal{L} = \frac{\dot{q}_{N_{Le} \neq 1}}{\dot{q}_{N_{Le} = 1}} = 1 + \left( N_{Le}^{.52} - 1 \right) \frac{I_{e,D}}{I_e} \quad (A-40)$$

was found to agree well with exact solutions for  $N_{Le} = 1.4$  in stagnation point flow. In high Mach number flows, however, Equation (A-40) may predict a significant diffusion effect under conditions for which no dissociation actually exists, since the temperatures within the boundary layer may be well below the stagnation value. To avoid this inconsistency, Equation (A-40) was modified to operate on the local reference enthalpy, corresponding to  $\rho_r\mu_r$ , rather than the stagnation value. The modified expression is given by:

$$\mathcal{L} = 1 + \left( N_{Le}^{.52} - 1 \right) \frac{i_{r,D}}{i_r} \quad (A-41)$$

Calculations made by Cohen (Reference 22) of Lewis number effects for non-stagnation boundary layers are shown in Figure 20, along with computations from Equation (A-41).

d. Reference Density-Viscosity Product

The reference density-viscosity product was first evaluated for zero Mach number with various degrees of wall cooling using the solutions of References 20, 23, and 24 and some unpublished solutions by Halvorson and Cassmeyer of The Boeing Company, as shown in Figure 21.

	○	□	△
Reference	7	23	22
Prandtl number	Constant	Constant	Variable
Specific heat	Constant	Constant	Variable
$\rho\mu$ product	Variable	Constant	Variable

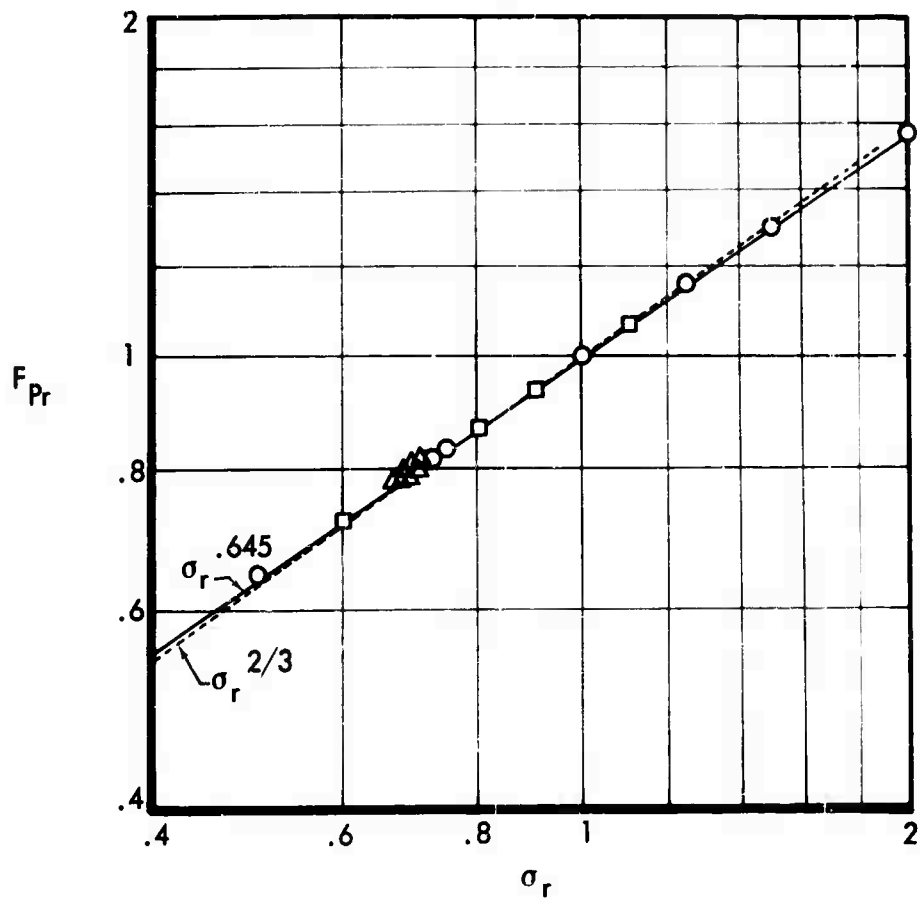


Figure 19: LAMINAR PRANDTL NUMBER EFFECT ON REYNOLDS ANALOGY FACTOR

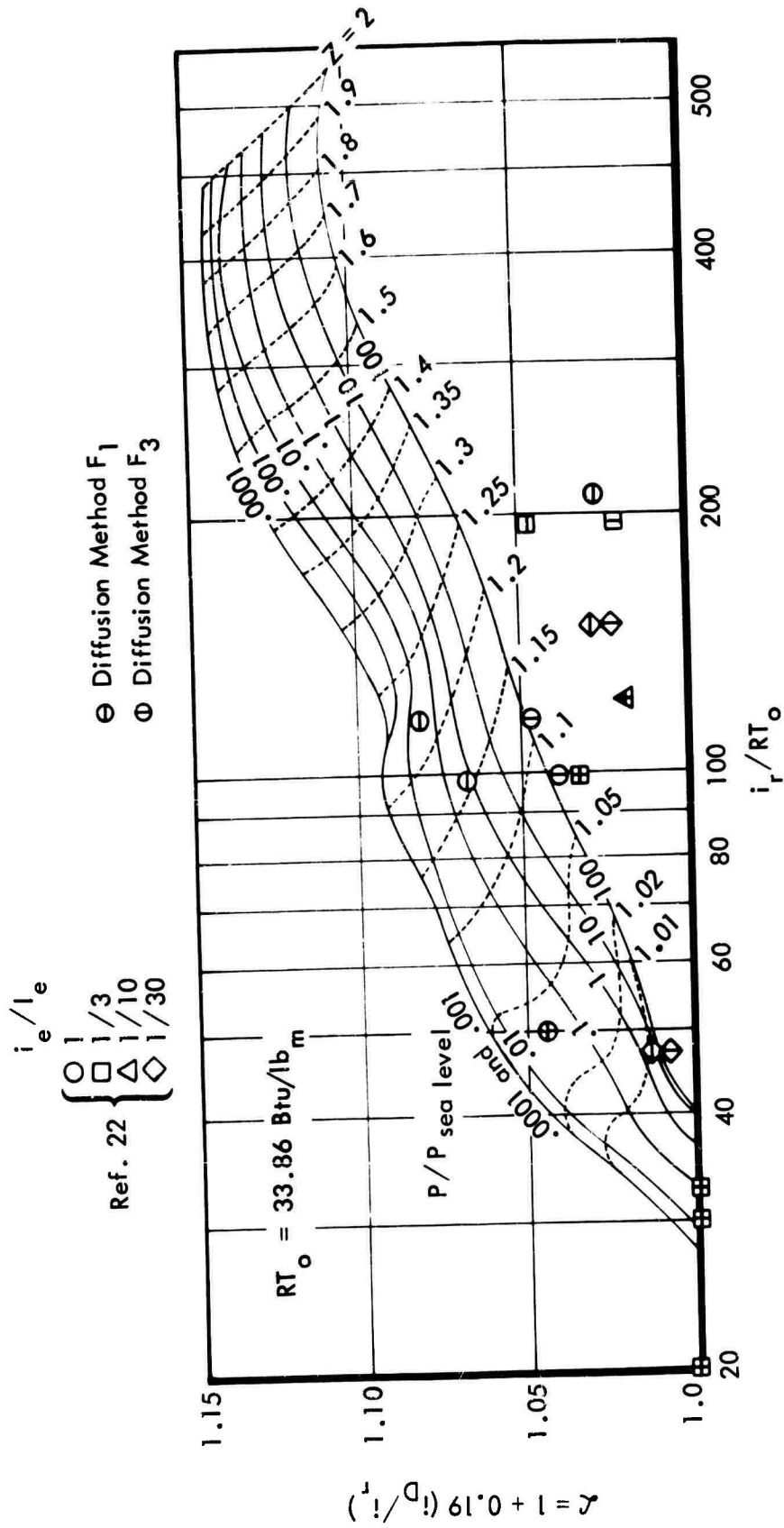


Figure 20: DIFFUSION EFFECT ON LAMINAR HEAT TRANSFER

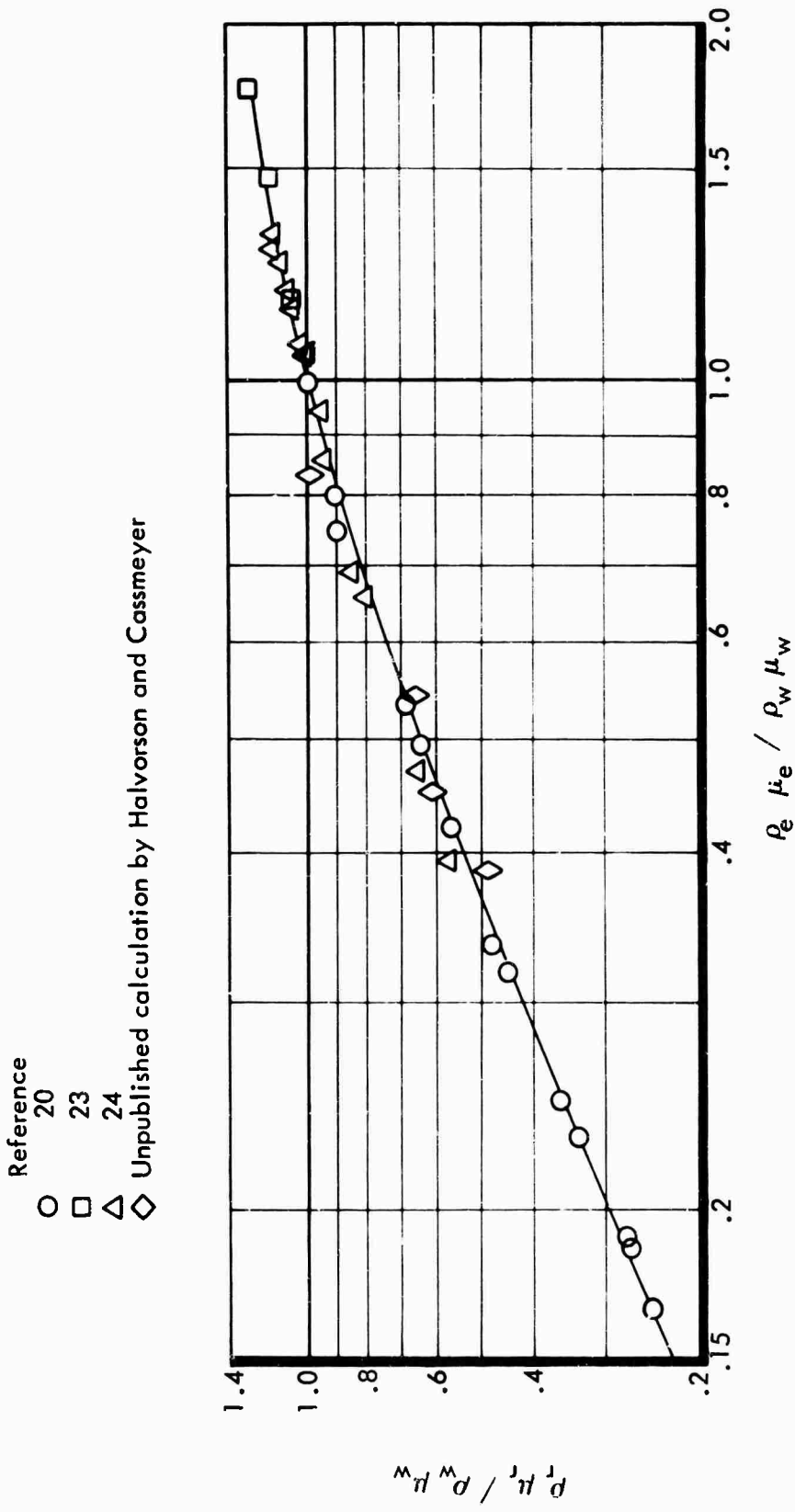


Figure 21: CORRELATION OF REFERENCE DENSITY-VISCOSITY PRODUCT AT M = 0

For edge Mach numbers greater than zero, it was found that the reference density-viscosity product  $\rho_r \mu_r$  can be represented as a function only of  $\rho_e \mu_e$ ,  $\rho_w \mu_w$  and  $\rho_{S'} \mu_{S'}$  where the latter is the density-viscosity product evaluated at stagnation enthalpy and the local pressure. The correlation obtained is given below:

$$\rho_r \mu_r = \rho_w \mu_w \left[ \frac{(\rho_e \mu_e)_{\text{eff}}}{\rho_w \mu_w} \right]^{\frac{7}{8}} \left\{ \frac{1.2}{.2 + \left[ \frac{(\rho_e \mu_e)_{\text{eff}}}{\rho_w \mu_w} \right]^5} \right\}^{\frac{1}{10}} \quad (\text{A-42})$$

where

$$(\rho_e \mu_e)_{\text{eff}} = \left\{ K^* \left[ \frac{13}{16} + \frac{3}{16} \exp \left( -K^* \frac{\rho_e \mu_e}{\rho_w \mu_w} \right) \right] \right\} \rho_e \mu_e$$

and

$$K^* = \frac{\rho_{S'} \mu_{S'}}{\rho_e \mu_e} \left[ \frac{1.005}{.005 + \left( \frac{\rho_{S'} \mu_{S'}}{\rho_e \mu_e} \right)^7} \right]^{\frac{1}{14}}$$

Equation (A-42) is plotted in Figure 2 (Section III. 1) using the approximation that the exponent  $K^*[(\rho_e \mu_e)/(\rho_w \mu_w)]$  is unity. The contribution of this term is small, and Figure 2 can be used to obtain  $\rho_r \mu_r$  without introducing significant errors. Subsequent investigations have shown that  $\rho_r \mu_r$  is independent of pressure gradients, as demonstrated by comparisons with exact solutions shown in Figure 22.

#### e. Pressure Gradient Effects

##### 1) Evaluation of $J_L$ and $\bar{E}$

Referring to Equation (A-23) and recalling the earlier comment that  $C_x$ ,  $m$ ,  $F_{Pr}$ , and  $\mathcal{L}$  are by definition taken as the flat plate values, it is seen that all pressure gradient effects are reflected in  $\rho_r \mu_r$  and  $x_{eq}$ . These effects can be evaluated for similar flows from the solutions published which consider streamwise pressure gradients, (e. g. , References 12 and 20) and those which consider crossflow pressure gradients (e. g. , References 21 and 22).

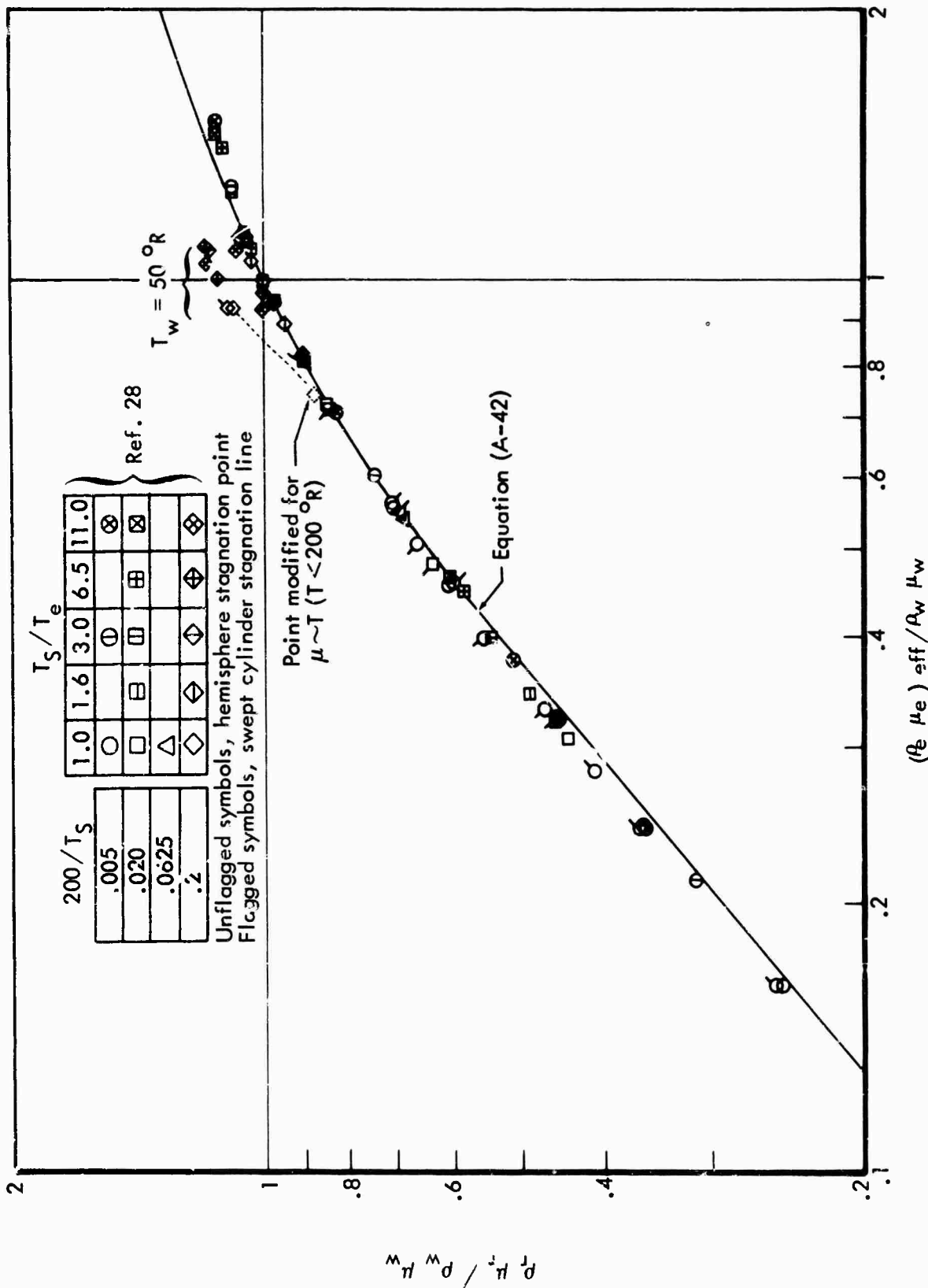


Figure 22: REFERENCE DENSITY-VISCOSITY PRODUCT FOR FLOWS WITH PRESSURE GRADIENT

Beginning with the simplest possible case, two-dimensional flow of an ideal gas with unit Prandtl number, and the viscosity proportional to temperature, the equivalent distance effects can be isolated. Since  $\rho\mu$  is always equal to  $\rho_e\mu_e$ , then  $\rho_r\mu_r$  is also equal to  $\rho_e\mu_e$ . (Note that  $\rho\mu$  is not necessarily constant through the flow field, but varies with the local boundary layer edge pressure.) With these values incorporated, the equivalent distance expression in Equation (A-24) reduces to:

$$x_{eq} = \frac{1}{J_L} \frac{\int_0^{x_1} \rho_e \mu_e u_e dx}{\left[ \rho_e \mu_e u_e \right]_{x_1}} \quad (A-43)$$

In Equation (A-43) the term  $\rho_e \mu_e u_e$  reflects the effects of upstream variations, while  $J_L$  accounts for local streamwise pressure gradient effects on the boundary layer profiles.

A correlation has been found for  $J_L$  which may be written:

$$J_L = [1 + .718(\sqrt{1 + F_\beta F_\Sigma} - 1)] \text{ when } \beta \geq 0$$

and

$$J_L = [1 + .718(\sqrt{1 + F_\beta F_\Sigma} - 1)]^{-1} \text{ when } \beta < 0 \quad (A-44)$$

where  $\beta$  is the dimensionless pressure gradient parameter similar to that defined by the authors of Reference 11. The parameters  $\beta$ ,  $F_\beta$ , and  $F_\Sigma$  are defined by Equations (A-50) to (A-53). Subsequent investigations of exact solutions for non-unit Prandtl number and nonlinear viscosity laws have shown that expressions of the form of Equation (A-43) are valid for these more complex conditions as well, either for two-dimensional flows with streamwise pressure gradients, or for yawed cylinder flow. The expressions finally adopted are:

$$(\rho_r \mu_r)_\beta = (\rho_r \mu_r)_{\beta=0} \quad (A-45)$$

and a generalization of Equation (A-43):

$$x_{eq, I} = \frac{1}{J_L} \frac{\int_0^{x_1} G_L dx}{\left[ G_L \right]_{x_1}} \quad (A-46)$$

where:

$$G_L = \rho_r u_{r e} \left( \frac{E_L}{r_f} \right)^2 \quad (A-47)$$

$$J_L = \left[ 1 + .718 (\sqrt{1 + F_{\beta, s} F_{\Sigma, s}} - 1) \right] \text{ when } \beta \geq 0$$

$$J_L = \left[ 1 + .718 (\sqrt{1 + F_{\beta, s} F_{\Sigma, s}} - 1) \right]^{-1} \text{ when } \beta < 0 \quad (A-48)$$

$$\bar{E}_L = 1 + .718 (\sqrt{1 + F_{\beta, c} F_{\Sigma, c}} - 1) (2 \Sigma_c)^{\exp K} \quad (A-49)$$

where:

$$\exp K = 0 \text{ when } N \leq .05 \text{ and } .99 \leq N \leq 1.01,$$

$$\exp K = -.194 \exp \left[ -\frac{2}{3} N(N-1) \right] \text{ when } .05 < N < .99,$$

$$\exp K = .194 \exp \left[ -\frac{2}{3} (N-1) \right] \text{ when } N > 1.01, \text{ and } N = \frac{x}{r_f} \frac{\partial(rf)}{\partial x}$$

The subscripts  $s$  and  $c$  are introduced to distinguish between streamwise and crossflow pressure gradients; it should be noted that  $J_L$  is concerned only with streamwise pressure gradient effects and  $\bar{E}_L$  only with crossflow effects; also, note that  $J_L = 1.0$  for  $\beta_s = 0$ .

The functions  $F_{\beta}$ ,  $\beta$ ,  $F_{\Sigma}$ , and  $\Sigma$  are given for either streamwise or crossflow pressure gradients by the following expressions:

(a) Streamwise Pressure Gradients:

$$F_{\beta, s} = \frac{\left\{ 1 + 2 \left[ \frac{(ZT)_e / (ZT)_s}{i_e / I_e} \right] \right\} |\beta_s|}{2 \left[ \frac{(ZT)_e / (ZT)_s}{i_e / I_e} \right] + \frac{j+1}{2} \beta_s} \quad (A-50)$$

where

$$j = |\beta_s| / \beta_s$$

$$\beta_s = 2 \frac{i_e \frac{d \ln u_e}{d \ln x}}{I_e} \frac{\int_0^{x_1} G_L dx}{[G_L x]_{x_1}} \quad (\text{A-51})$$

$$F_{\Sigma, s} = \frac{\Sigma_s - .294}{.402} \left( \frac{i_{aw}}{I_e} \right) \sigma_r^{.355} \quad (\text{A-52})$$

and

$$\Sigma_s = \frac{\rho_s}{\rho_{m, s}} = \frac{(ZT)_{m, s}}{(ZT)_s} \quad (\text{A-53})$$

The subscript m denotes evaluations at local pressure and a mean boundary layer enthalpy defined by:

$$i_{m, s} = .5(I_e - i_w) \quad (\text{A-54})$$

The second equality in Equation (A-53) follows from the condition of constant pressure across the boundary layer.

(b) Crossflow Pressure Gradients:

$$F_{\beta, c} = \beta_c = 1 \quad (\text{A-55})$$

$$F_{\Sigma, c} = \frac{\Sigma_c - .294}{.402} \sigma_r^{.355} \quad (\text{A-56})$$

$$\Sigma_c = \frac{\rho_{e, SL}}{\rho_{m, c}} = \frac{(ZT)_{m, c}}{(ZT)_{e, SL}} \quad (\text{A-57})$$

The subscript SL refers to the stagnation line and  $(ZT)_{m,c}$  is evaluated at local pressure and a mean boundary layer enthalpy defined by:

$$i_{m,c} = .5(i_w + i_{e,SL}) + .206 (i_e - I_{e,SL}) \sigma_r \sqrt{\frac{\rho_{S'} \mu_{S'}}{\rho_w \mu_w}} \quad (A-58)$$

With a minor modification of  $x_{eq,L}$ , it is easily shown that the definition of  $\beta_S$ , given by Equation (A-51), is identical to the corresponding parameter of Reference 12. The expressions for obtaining  $J_L$ . Equations (A-48) and (A-50) to (A-54) were developed on the basis of providing the best fit to the exact similar solutions shown in Figure 23. However, the obvious similarity of Equations (A-50) to (A-54) to the various reference enthalpies appearing in the literature provides some analytical justification for these correlations.

The equations for obtaining  $J_L$  furnished a basis for determining  $\bar{E}$ . The cross-flow pressure gradient parameter  $\beta_c$  was assumed to be unity, which is the value for an unyawed cylinder. Comparisons of  $\bar{E}$  from Equations (A-49) and (A-55) to (A-58) for swept cylinder flow are shown in Figure 24. Similar comparisons with yawed cone solutions are presented in Figure 25. The term  $(2\Sigma_c)^{\exp K}$  was developed on the basis of the yawed cone comparisons. Note that this term is unity for the cylinder case.

## 2) Evaluation of $P_L$

Correlations of "exact" laminar solutions show that the influence of streamwise pressure gradients on skin friction, which is reflected in  $P_L$ , can be easily related to the corresponding effect on  $J_L$ . The relationship is:

$$P_L = J_L^5 \quad (A-59)$$

Comparisons with solutions presented in References 11 and 22 are shown in Figure 26. Equation (A-36) now becomes:

$$S_{cq} = \frac{\int_0^{x_1} G_L dx}{\left[ J_L^5 G_L \right]_{x_1}} = \frac{x_{eq}}{J_L^4} \quad (A-60)$$

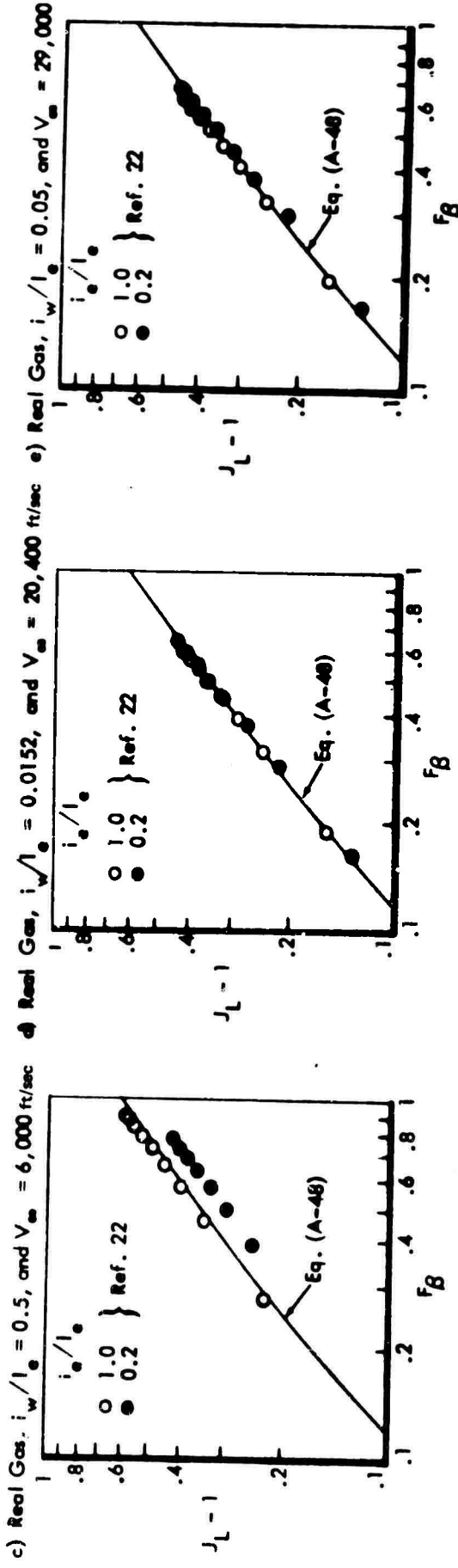
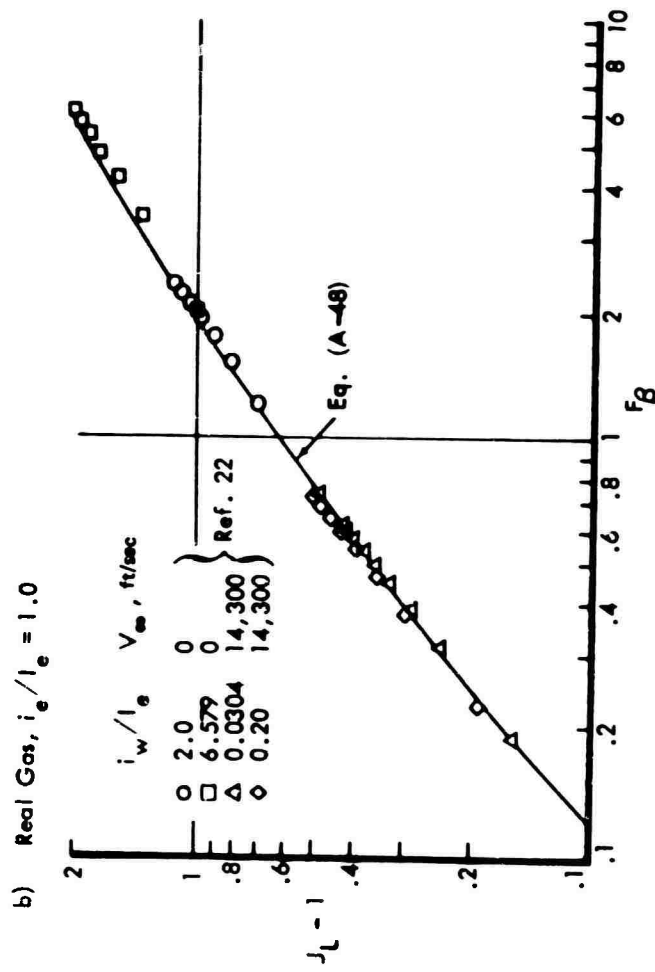
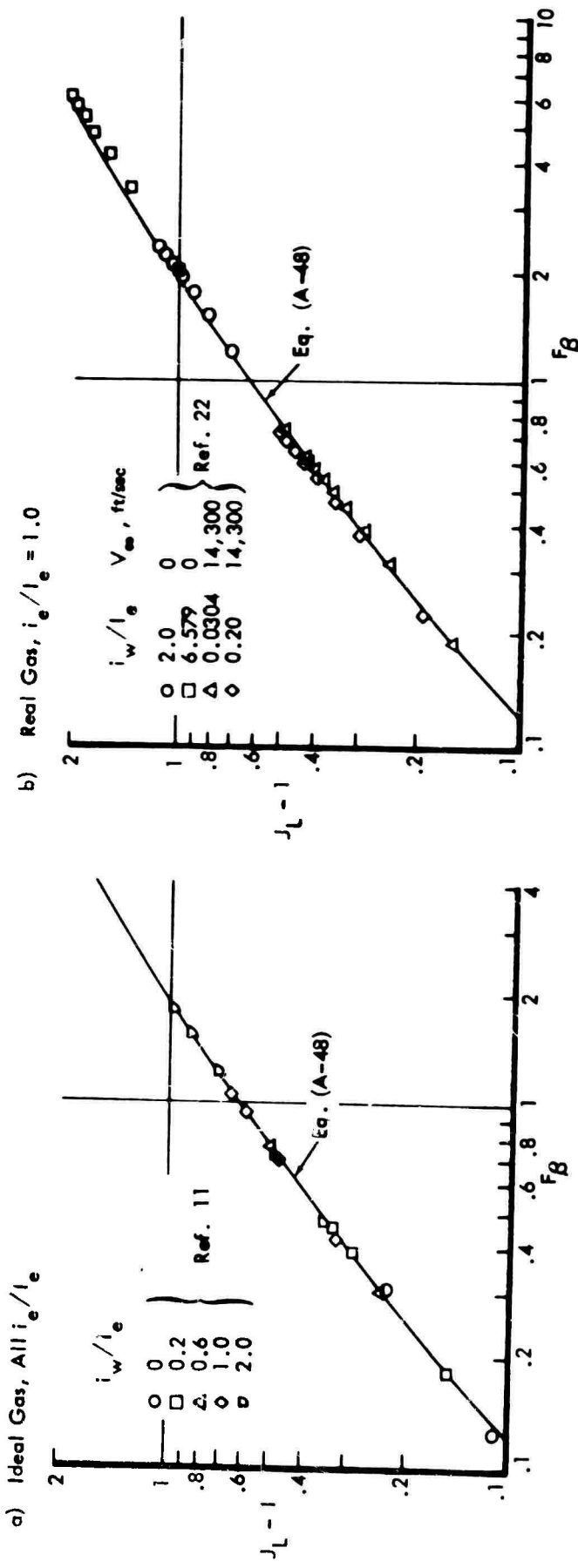


Figure 23: STREAMWISE PRESSURE GRADIENT FUNCTION  $J_L$

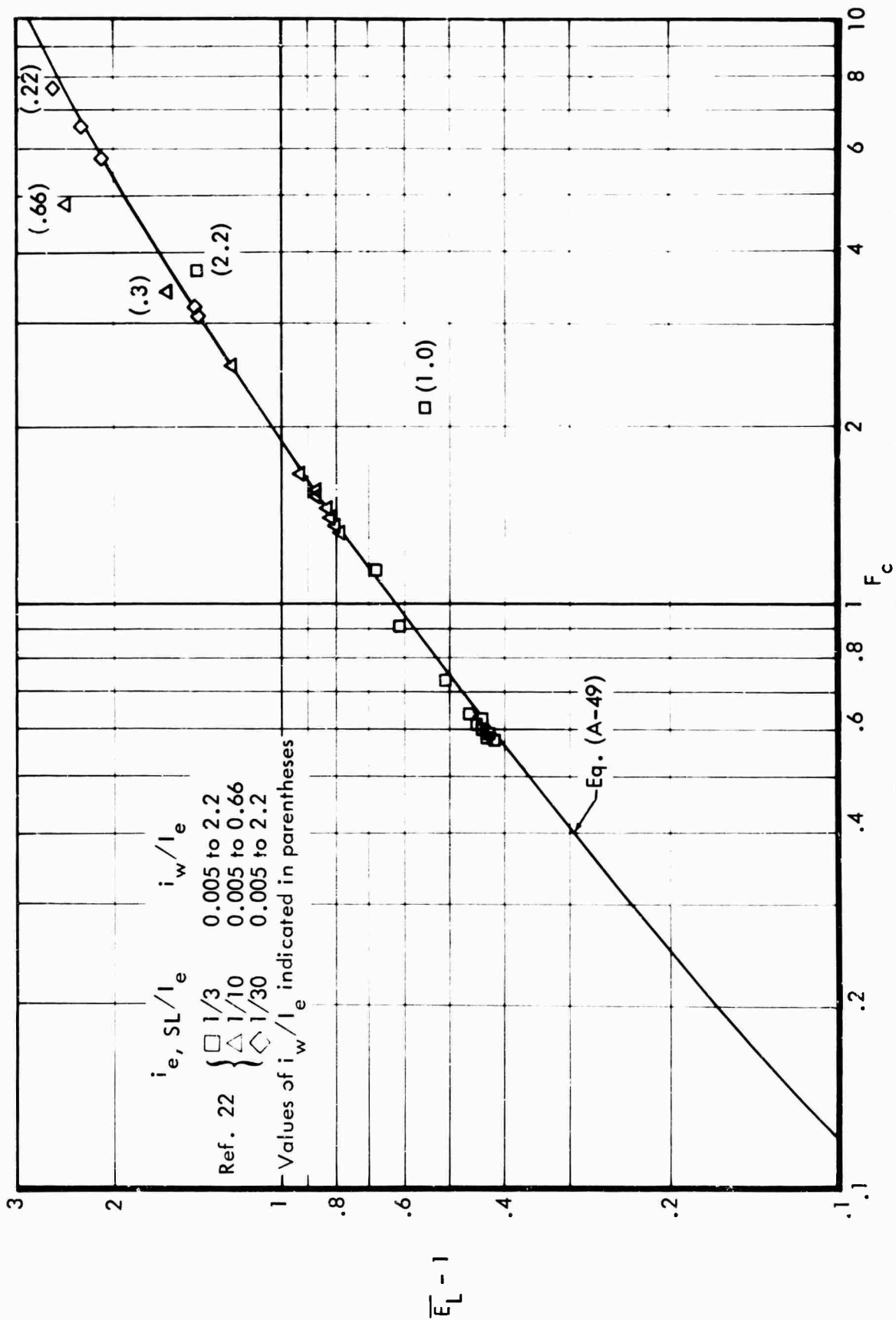


Figure 24: REAL-GAS CORRELATION PARAMETER FOR SWEEP INFINITE CYLINDERS

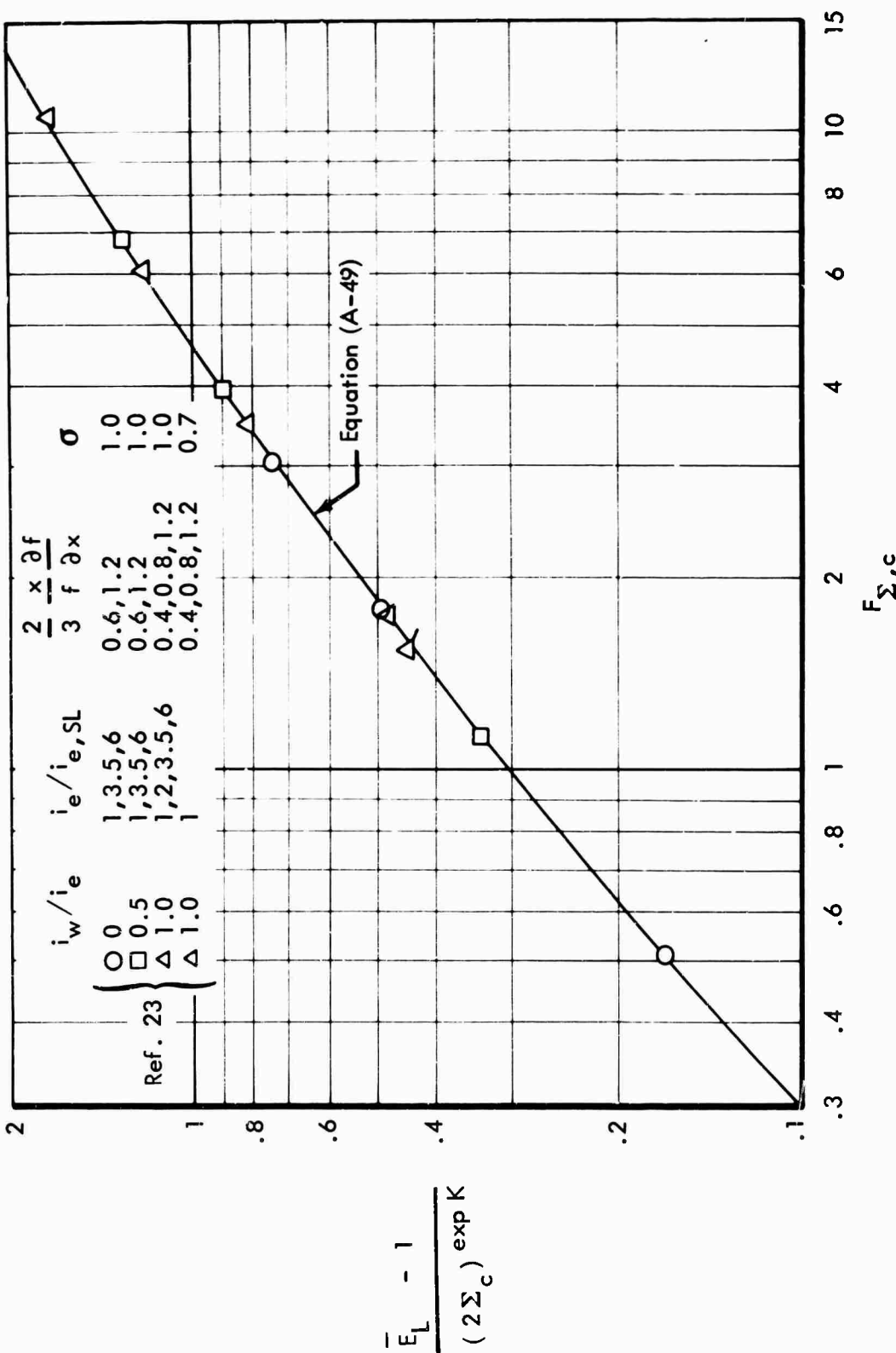


Figure 25: CROSSFLOW CORRELATIONS FOR YAWED CONE FLOW

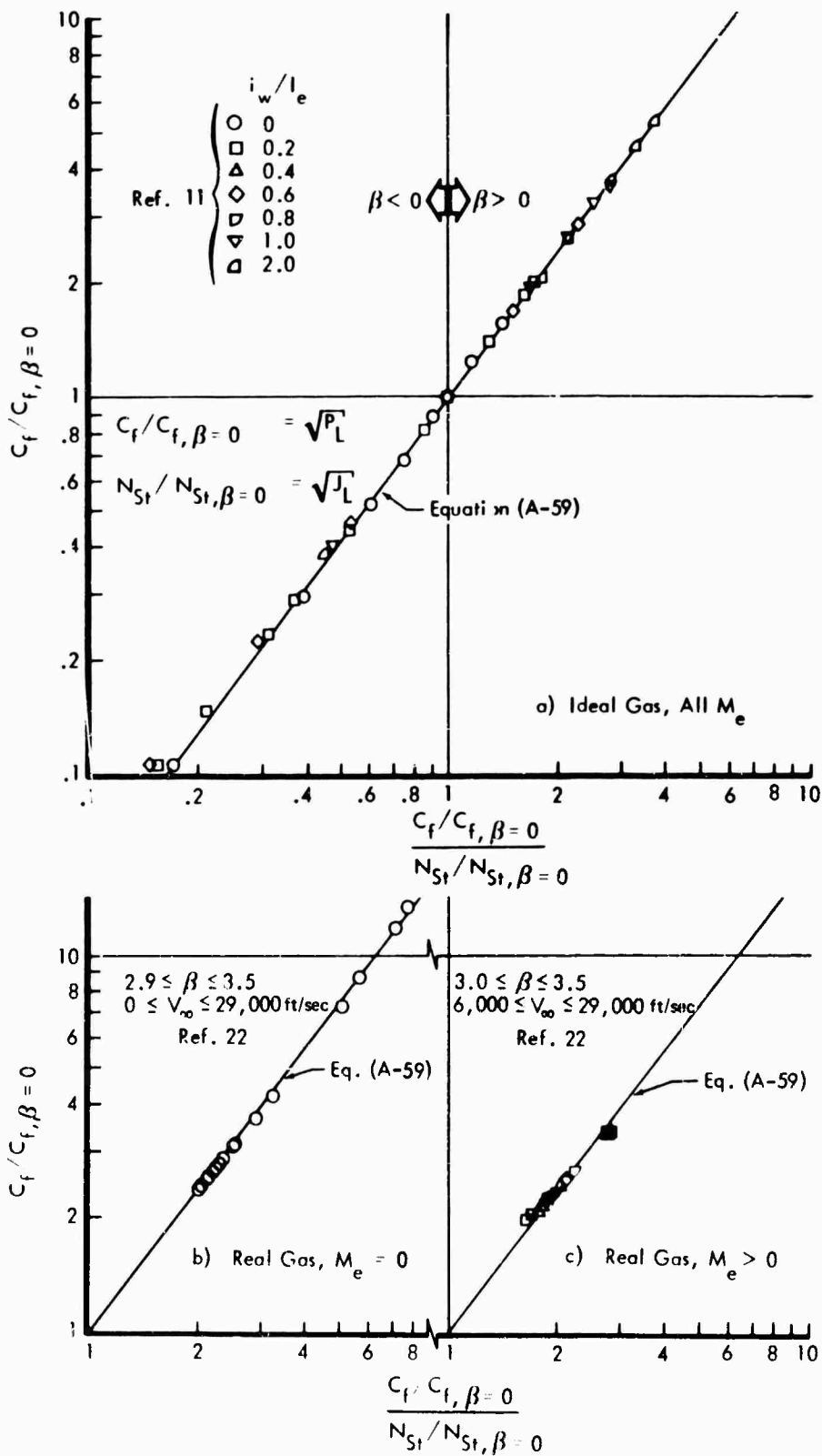


Figure 26: STREAMWISE PRESSURE GRADIENT EFFECT ON SKIN FRICTION

## 5. COMBINED LAMINAR AND TURBULENT METHOD<sup>4</sup>

The  $\rho_r \mu_r$  computer program described in Appendix D is intended for making heat transfer and skin friction predictions for both laminar and turbulent flows. For computer purposes, it is convenient to utilize parameters common to both laminar and turbulent boundary layers whenever possible. A problem is encountered in defining a reference Reynolds number since the equivalent distances  $x_{eq}$ , Equation (A-43), and  $S_{eq}$ , Equation (A-60), are usually different for the two types of flow. To remedy this, the following definitions for reference Reynolds numbers are used:

$$\bar{N}_{R,r,Q} = \frac{\rho_r \mu_r u_e \bar{x}_{eq,L}}{(F_{x,Q} \mu_o)^2} \quad (A-61)$$

and

$$\bar{N}_{R,r,S} = \frac{\rho_r \mu_r u_e \bar{S}_{eq,L}}{(F_{x,S} \mu_o)^2} \quad (A-62)$$

where

$$F_{x,Q} = \left[ J_L \frac{17}{20} \left( \frac{b_{eq,T}}{b_{eq,L}} \right) \right]^{\frac{1}{3}} \quad (A-63)$$

$$F_{x,S} = \left[ J_L \frac{17}{4} \left( \frac{b_{eq,T}}{b_{eq,L}} \right) \right]^{\frac{1}{3}} \quad (A-64)$$

$$b_{eq,T} = \frac{\int_0^{x_1} G_T dx}{[G_T]_{x_1}} \quad (A-65)$$

<sup>4</sup> Parameters defined in this section are used only in the  $\rho_r \mu_r$  computer program and except for Appendix C are not used elsewhere in this report.

$$b_{eq, L} = \frac{\int_0^{x_1} G_L dx}{|G_L|_{x_1}} \quad (A-66)$$

$$\bar{x}_{eq, L} = J_L^{\frac{6}{10}} x_{eq, L} = J_L^{-\frac{4}{10}} b_{eq, L} \quad (A-67)$$

and

$$\bar{S}_{eq, L} = J_L^3 S_{eq, L} = J_L^{-2} b_{eq, L} \quad (A-68)$$

Definitions for  $G_L$ ,  $G_T$ ,  $J_L$ ,  $x_{eq, L}$ , and  $S_{eq, L}$  are given in preceding sections of this appendix.

a. Laminar Flow

Using the definitions given above, the general expressions for heat transfer, Equation (A-23), and skin friction, Equation (A-34), become; respectively:

$$H = \frac{C_x \bar{Q}_L F_{x, Q}}{\sigma_r \cdot 645 \bar{x}_{eq, L}} \left( \bar{N}_{R, r, Q} \right)^{\frac{m}{m+1}} \quad (A-69)$$

and

$$\frac{\tau_w}{u_e} = \frac{C_x \mu_o \bar{P}_L F_{x, S}}{\bar{S}_{eq, L}} \left( \bar{N}_{R, r, S} \right)^{\frac{m}{m+1}} \quad (A-70)$$

where

$$\bar{Q}_L = J_L^{\frac{3}{10}}$$

and

$$\bar{P}_L = J_L^{\frac{3}{2}}$$

b. Turbulent Flow

For turbulent flow, the form of Equations (A-69) and (A-70) can be changed to the Schultz-Grunow form given by Equations (13) and (14). The final turbulent equations then become:

$$H = \frac{.185 \mathcal{L} \mu_o \bar{Q}_L F_{x,Q}}{\sigma^{.645} \bar{x}_{eq,L}} \frac{\bar{N}_{R,r,Q}}{\left[ \log_{10} (\bar{N}_{R,r,Q} + 3000) \right]^{2.584}} \quad (A-71)$$

and

$$\frac{\tau_w}{u_e} = \frac{.185 \mu_o \bar{P}_L F_{x,S}}{\bar{s}_{eq,L}} \frac{\bar{N}_{R,r,S}}{\left[ \log_{10} (\bar{N}_{R,r,S} + 3000) \right]^{2.584}} \quad (A-72)$$

## APPENDIX B

### SIMPLIFIED $\rho_r \mu_r$ METHOD

The complete  $\rho_r \mu_r$  equations presented in the text of this report are intended for computer use only, since manual computations are exceedingly tedious. However, simplified equations have been found that greatly reduce the work required in making slide rule calculations with little loss in accuracy. First, general simplifications for arbitrary geometries are presented, and secondly, equations for a few specific body shapes are given. Comparisons with results obtained using the complete  $\rho_r \mu_r$  equations are also shown.

#### 1. GENERAL SIMPLIFICATIONS

##### a. Evaluation of $\rho_r \mu_r$

A convenient method for estimating  $\rho_r \mu_r$  presented in Reference 2 provides values within about three percent of those obtained using Equation (A-42). The suggested expressions are:

$$\rho_r \mu_r = (\rho_e \mu_e)_{\text{eff}} \left[ 1.6 - .6 \frac{(\rho_e \mu_e)_{\text{eff}}}{(\rho_w \mu_w)} \right]$$

$$(\rho_e \mu_e)_{\text{eff}} = \rho_{S'} \mu_{S'} \left[ 1.85 - .85 \frac{\rho_{S'} \mu_{S'}}{\rho_e \mu_e} \right] \quad (\text{B-1})$$

Note that  $\rho_{S'} \mu_{S'}$  is evaluated at the stagnation enthalpy and the local pressure.

##### b. $\rho_r \mu_r$ Variation with x

Unless large variations in wall temperature occur,  $\rho_r \mu_r$  can be considered to be proportional to pressure along a given streamline. Also, the effect of the pressure gradient parameter  $J_T$  on heat transfer can usually be neglected. For example, the pressure gradient effect on the peak turbulent heating rate for a hemisphere is only about 3 or 4 percent. With these approximations, Equation (8) reduces to:

$$x_{1,T} = \frac{1}{\left[ P_e u_e (r \bar{E})^{5/4} \right]_{x_1}} \int_0^{x_1} P_e u_e (r \bar{E})^{5/4} dx \quad (\text{B-2})$$

and

$$\rho_r \mu_r = (\rho_r \mu_r)_m (P_e/P_m)$$

The subscript m denotes that the evaluation is made at approximately the mean pressure along the streamline.

c. Evaluation of  $\bar{E}_T$

For most cases the influence of the following term appearing in Equation (32) can be neglected:

$$(2 \Sigma_c)^{\exp K}$$

Note that this term is large only when  $(x/rf) (\partial rf/\partial x)$  is small; consequently, the influence of  $\bar{E}_T$  is also usually small. In addition, it is seen in Figure 7 that  $\sigma$  varies only from .68 to .776. Thus, using an average  $\sigma_r = .728$  in computing

$$\sigma_r^{.355} = .893 \quad (\text{B-4})$$

in Equation (A-56) will result in, at most, an error of 2.4 percent. Equation (32) can now be simplified to

$$\bar{E}_T = \left[ 1 + .55 \left( \sqrt{1 + F_{\Sigma, c, o}} - 1 \right) \right] \left[ \frac{1 + .718 \left( \sqrt{1 + F_{\Sigma, c}} - 1 \right)}{1 + .718 \left( \sqrt{1 + F_{\Sigma, c, o}} - 1 \right)} \right]^4 \quad (\text{B-5})$$

where

$$F_{\Sigma, c} = 2.22 (\Sigma_c - .294)$$

Equations (A-57) and (A-58) define  $\Sigma_c$  and Equation (30) defines  $\Sigma_{c, o}$ . Equation (B-5) is plotted in Figure 27 to facilitate computations of  $\bar{E}_T$ .

d. Evaluation of  $\mathcal{L}$  and  $F_{Pr}$

For real-gas flow in chemical equilibrium, the diffusion influence parameter can be obtained either from Equation (A-41) or Figure 20. However, this term is usually quite close to unity. The maximum value of  $\mathcal{L}$  obtained from thermal analysis of the reentry vehicle presented in Section VIII was 1.04, representing a correction of only 4%.

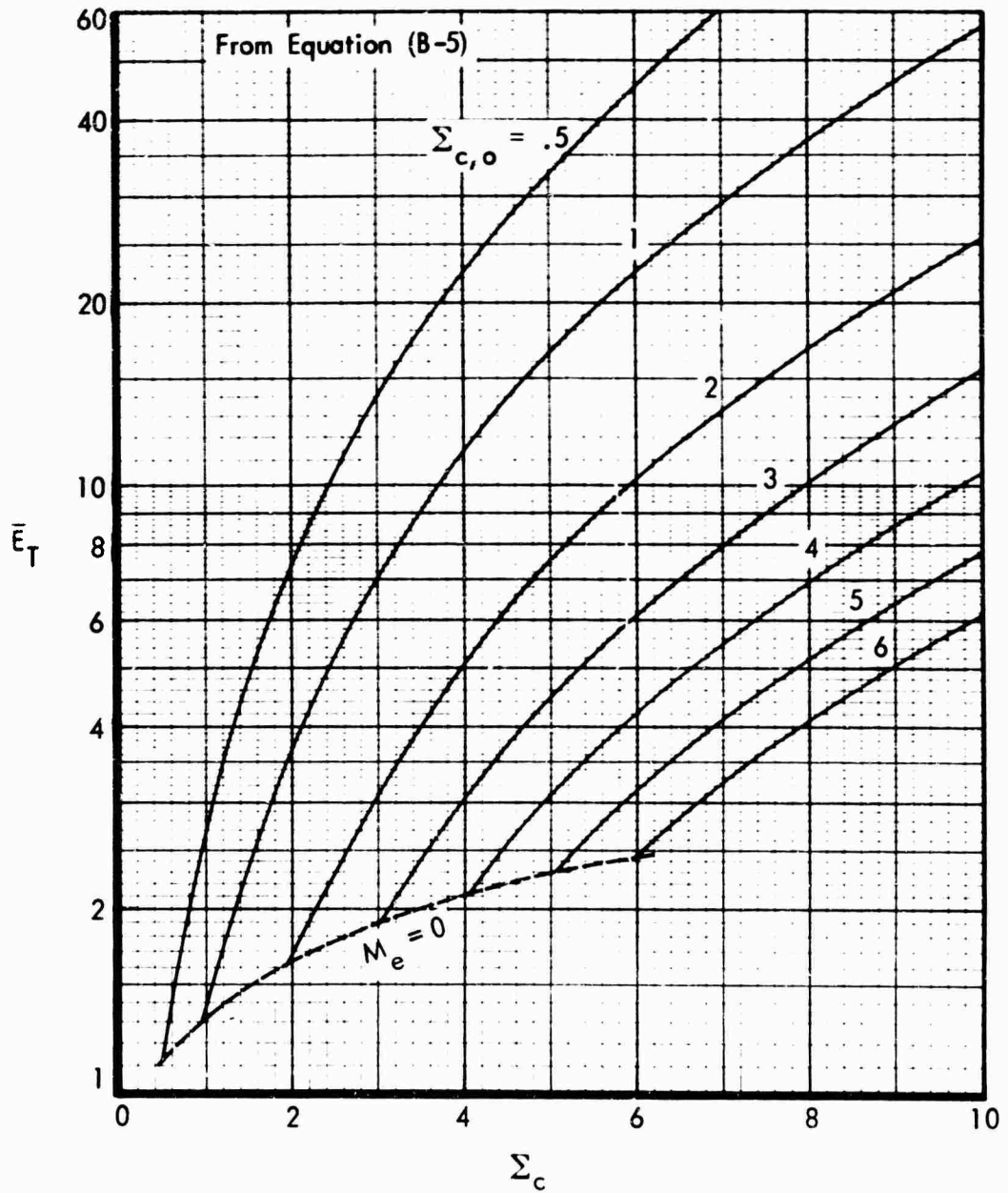


Figure 27: TURBULENT CROSSFLOW MOMENTUM THICKNESS RATIO

Similarly, when using Equation (20), the approximation that  $\sigma_r = .728$ , or

$$\sigma_r^{.645} = .815 \quad (\text{B-6})$$

can lead to, at most, an error of 4.3 percent.

e. Summary Heat Transfer Equation

Using all of the approximations given above, Equations (13) and (15) reduce to:

$$H_T = .228 \frac{\mu_o}{x_{eq,T}} \frac{N_{R,r,Q}}{\left[ \log_{10} (N_{R,r,Q} + 3000) \right]^{2.584}} \quad (\text{B-7})$$

$$N_{R,r,Q} = \frac{P_e}{P_m} \frac{(\rho_r \mu_r) u_e x_{eq,T}}{\mu_o^2} \quad (\text{B-7})$$

The equivalent distance  $x_{eq,T}$  can be obtained using Equation (B-2) and the stagnation viscosity  $\mu_o$  from Equation (19).

f. Momentum Thickness

An alternate method for computing momentum thickness is provided by:

$$\theta_T = .231 \frac{\mu_o}{\rho_e u_e} \frac{N_{R,r,S}}{\left[ \log_{10} (N_{R,r,S} + 3000) \right]^{2.584}} \quad (\text{B-9})$$

If the effects of pressure gradient on the boundary layer profiles are neglected ( $J_T = P_T = 1.0$ ), the equivalent distances for heat transfer and skin friction are equal. For this case, Equation (B-9) can be written:

$$\begin{aligned} \theta_T &= \frac{5}{4} \frac{F_{Pr}}{\mathcal{L}} \frac{H_T}{\rho_e u_e} x_{eq,T} \\ &\approx 1.015 \frac{H_T}{\rho_e u_e} x_{eq,T} \end{aligned} \quad (\text{B-10})$$

## 2. SPECIAL CASES

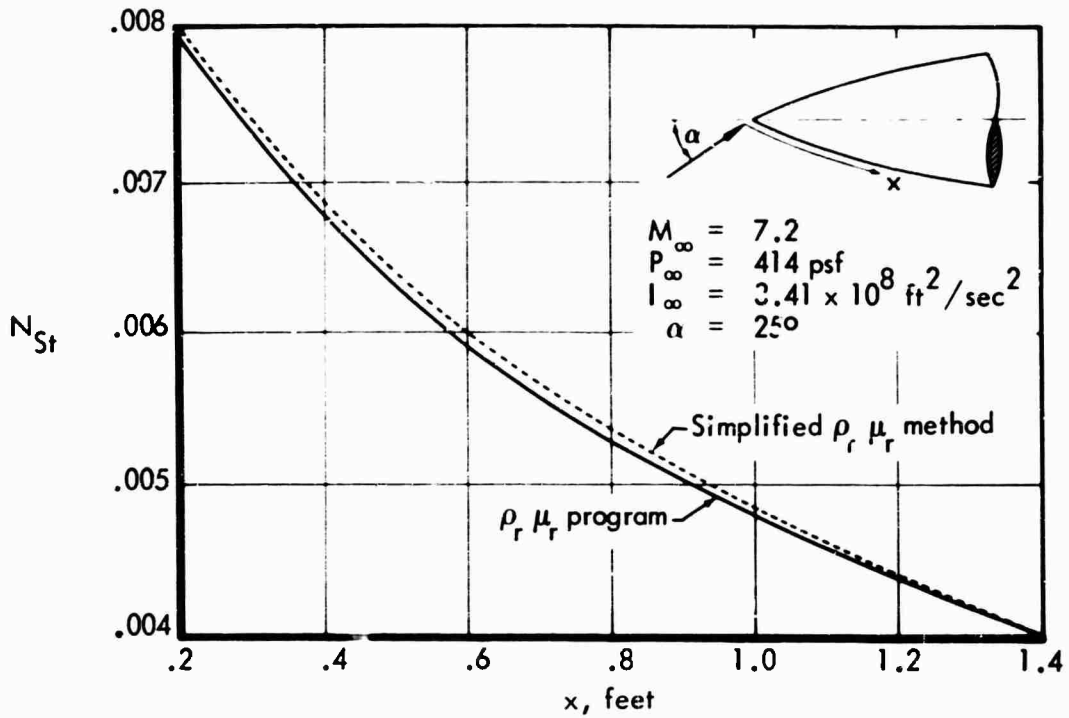
In most cases, the most tedious task in computing heating rates is the computation of the equivalent distance. For many common body shapes, Equation (B-2) can be simplified further. The following table summarizes the expressions for equivalent distance for some simple configurations.

Configuration	$\alpha$		$x_{eq, T}$
Flat plate	All		$x$
Cone	0		$(4/9)x$
	$\neq 0$		$\frac{x}{(9/4) + (5/4) N \bar{E}_T}$
Swept infinite cylinder stagnation line	0		$\frac{u_e}{(5/4) (\partial v_e / \partial y) \bar{E}_T}$
Delta wing centerline	0		$x$
	$\neq 0$	$n \leq 1$	$\frac{x}{1 + (5/4) n [2 - n + (n - 1) \bar{E}_T]}$
	$\neq 0$	$n > 1$	$\frac{x}{1 + (5/4) [1 + (n - 1) \bar{E}_T]}$

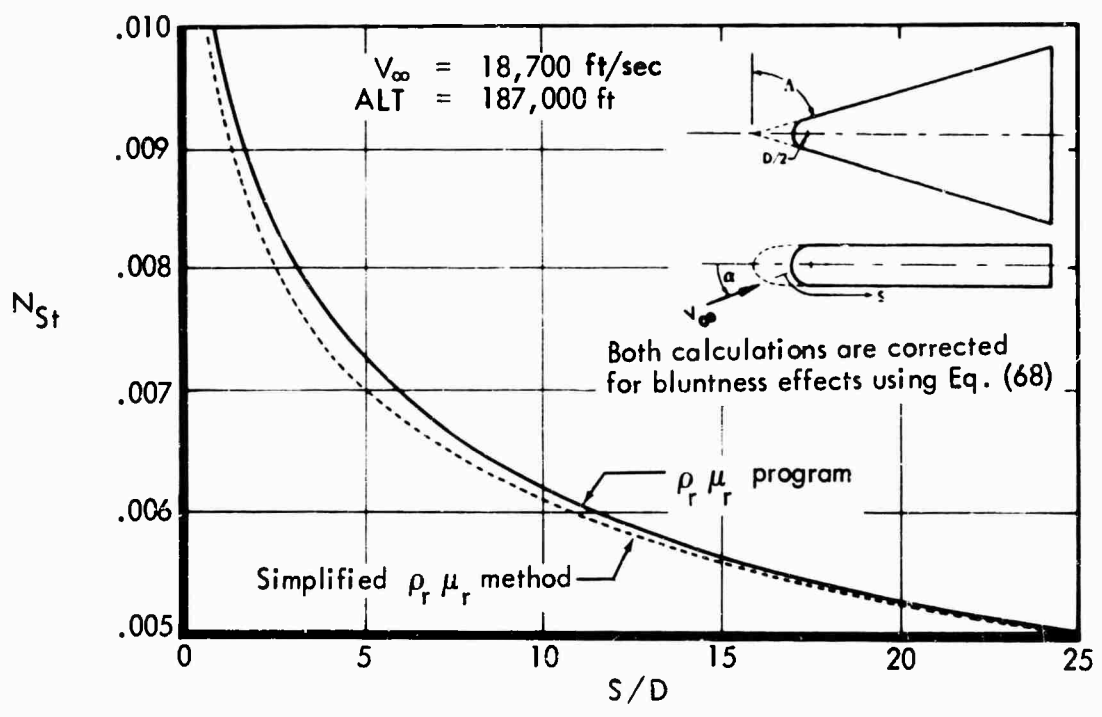
Equations for evaluating  $N$  and  $n$  are presented in Section V for the respective configurations.

## 3. COMPARISONS WITH COMPUTER RESULTS

Comparisons of Stanton numbers along the stagnation line of a sharp ogive at angle of attack are shown in Figure 28a. The simplified  $\rho_r \mu_r$  results were obtained using Equation (B-7) together with an equivalent distance computed using Equation (B-2). These results are seen to agree within 2% with those obtained using the  $\rho_r \mu_r$  program described in Volume III. The free stream flow conditions represent a typical test condition in the CAL high energy shock tunnel.



a) CAL Shock Tunnel, Sharp Ogive



b) Flight, Blunt Delta Wing Centerline

Figure 28: STANTON NUMBERS FROM SIMPLIFIED AND COMPLETE  $\rho_r \mu_r$  EQUATIONS

Similar comparisons along the centerline of a blunt delta wing are presented in Figure 28b. The configuration and flight conditions ( $V_\infty = 18,700$  ft/sec and ALT = 187,000 ft) correspond to the orbital reentry analysis described in Section VIII. The Stanton numbers obtained from both methods have been corrected for bluntness effects using Equation (74). The momentum thickness used in computing bluntness corrections for the simplified  $\rho_r \mu_r$  values were obtained using Equation (B-10). Results from the two methods are seen to differ by less than about 4%.

## APPENDIX C

### TURBULENT NONSIMILAR METHOD

The primary purpose in developing this method was to provide a means of computing complete boundary layer profiles for compressible turbulent flows. Preliminary results from this analysis are reported in Reference 25. The flow equations are solved in partial differential form, and unlike previous methods, empirical correlations are required only in defining the Reynolds stresses. Solutions obtained in this way are not subject to the usual restrictions regarding profile similarity; hence, effects of streamwise pressure and wall temperature gradients are easily included. This approach has been successfully used in treating laminar flows for several years (References 1 and 6).

The turbulent nonsimilar equations have been programmed for both the IBM 7094 and the Univac 1108 digital computers. This program, including equations and sample input sheets, is presented in Volume III. The existing program is restricted to ideal gases, but real gas effects could be included by adding tables for obtaining gas properties as a function of enthalpy and pressure.

The development of the turbulent nonsimilar method is presented in four parts:

1. Derivations of flow equations
2. Evaluation of turbulent stresses
3. Heat transfer results
4. Convergence and stability

#### 1. DERIVATION OF FLOW EQUATIONS

Several formulations of the fundamental turbulent flow equations can be found in the literature (e.g., References 3 and 7). Normally, the suggested expressions consist of the corresponding laminar equation with an added term, or terms, representing the influence of the turbulent fluctuations. The flow equations can then be written for two dimensional flow, in the following form:

$$\text{(x-Momentum)} \quad \rho u \frac{\partial u}{\partial x} - \left( \int_0^y \frac{\partial \rho u}{\partial x} dy \right) \frac{\partial u}{\partial y} = -\frac{\partial P}{\partial x} + \frac{\partial}{\partial y} \left( \mu \frac{\partial u}{\partial y} + \tau_T \right) \quad (\text{C-1})$$

$$\begin{aligned}
 \text{(Energy)} \quad \rho u \frac{\partial I}{\partial x} - \left( \int_0^y \frac{\partial \rho u}{\partial x} dy \right) \frac{\partial I}{\partial y} &= \frac{\partial}{\partial y} \left( \frac{\mu}{N_{Pr}} \frac{\partial i}{\partial y} + \dot{q}_T \right) \\
 &+ \frac{\partial}{\partial y} \left[ u \left( \mu \frac{\partial u}{\partial y} + \tau_T \right) \right] \quad \text{(C-2)}
 \end{aligned}$$

$$\text{(Equation of State)} \quad P = \rho RT \quad \text{(C-3)}$$

$\tau_T$  is the effective turbulent shear and  $\dot{q}_T$  is the effective turbulent heat conduction term. It should be noted that  $\tau_T$  and  $\dot{q}_T$  do not truly represent viscous and conduction effects, but account for the net effect of the turbulent fluctuations. Except for these turbulent stress terms, Equations (C-1) and (C-2) are identical with the corresponding equations for laminar flow.

Minor differences exist in the literature concerning both the definition and formulation of the turbulent stress terms. However, in the present analysis, empirical correlations are used in evaluating these terms, and the exact analytical formulation is immaterial.

It is now convenient to introduce a velocity parameter  $\tilde{v}$  defined by:

$$\frac{1}{r} \frac{\partial \rho u r}{\partial x} + \frac{\partial \rho \tilde{v}}{\partial y} = 0 \quad \text{(C-4)}$$

or

$$\tilde{v} = \frac{1}{r} \int_0^y \frac{\partial \rho u r}{\partial x} dy$$

The streamline divergence parameter  $r$  is introduced into Equation (C-4) to account for three-dimensional effects. For laminar flows it is seen from the mass conservation equation that  $\tilde{v}$  is equal to the velocity component normal to the surface ( $v$ ). This is not necessarily the case for turbulent flows, because of the fluctuating terms denoted by primes appearing in the conservation equation shown below:

$$\frac{1}{r} \frac{\partial \rho u r}{\partial x} + \frac{1}{r} \frac{\partial \rho' u' r}{\partial x} + \frac{\partial \rho v}{\partial y} + \frac{\partial \rho' v'}{\partial y} = 0 \quad \text{(C-5)}$$

Using Equation (C-4), Equations (C-1) and (C-2) can be written:

$$\frac{\partial u}{\partial x} = \frac{1}{\rho u} \left[ -\frac{\partial P}{\partial x} + \frac{\partial}{\partial y} \left( \mu \frac{\partial u}{\partial y} + \tau_T \right) \right] - \frac{\tilde{v}}{u} \frac{\partial u}{\partial y} \quad \text{(C-6)}$$

$$\frac{\partial I}{\partial x} = \frac{1}{\rho u} \frac{\partial}{\partial y} \left[ \frac{\mu}{N_{Pr}} \frac{\partial i}{\partial y} + \dot{q}_T + u \left( \mu \frac{\partial u}{\partial y} + \tau_T \right) \right] - \frac{\tilde{v}}{u} \frac{\partial I}{\partial y} \quad \text{(C-7)}$$

Solutions are to be obtained by numerically integrating Equations (C-6) and (C-7) with respect to  $x$ . In order to perform this integration,  $\partial u/\partial x$  and  $\partial I/\partial x$  must be expressed explicitly by the flow properties at a given station in  $x$ . That is, the right side of Equations (C-6) and (C-7) cannot contain derivatives with respect to  $x$  other than  $\partial P/\partial x$  and  $\partial r/\partial x$ , which are specified at all  $x$  locations. The purpose of the following derivation is to obtain an expression for  $\tilde{v}$  that does not contain  $x$  derivatives other than  $\partial P/\partial x$  and  $\partial r/\partial x$ .

Using the equation of state (C-3), Equation (C-4) can be expanded to:

$$-\rho \frac{\partial \tilde{v}}{\partial y} - \rho \tilde{v} \left( \frac{\partial P/\partial y}{\rho} - \frac{\partial T/\partial y}{T} \right) = \rho \frac{\partial u}{\partial x} + \rho u \left( \frac{\partial P/\partial x}{P} - \frac{\partial T/\partial x}{T} + \frac{\partial r/\partial x}{r} \right) \quad (C-8)$$

We can assume  $\partial P/\partial y \approx 0$ , since this analysis is restricted to thin boundary layers. Also, assuming an ideal gas ( $i = c_p T$ ), Equation (C-8) can be further expanded to give:

$$-\frac{\partial \tilde{v}}{\partial y} + \tilde{v} \left( \frac{\partial I/\partial y}{i} - u \frac{\partial u/\partial y}{i} \right) = \frac{\partial u}{\partial x} + u \left[ \frac{\partial P/\partial x}{P} + \frac{\partial r/\partial x}{r} - \frac{\partial I/\partial x}{i} + u \frac{\partial u/\partial x}{i} \right] \quad (C-9)$$

Then, from Equations (C-6) and (C-7):

$$\begin{aligned} \frac{\partial u}{\partial x} &= A - \frac{\tilde{v}}{u} \frac{\partial u}{\partial y} \\ \frac{\partial I}{\partial x} &= B - \frac{\tilde{v}}{u} \frac{\partial I}{\partial y} \end{aligned} \quad (C-10)$$

where

$$\begin{aligned} A &= \frac{1}{\rho u} \left( -\frac{\partial P}{\partial x} + \frac{\partial}{\partial y} \left( \mu \frac{\partial u}{\partial y} \right) + \frac{\partial \tau_T}{\partial y} \right) \\ B &= \frac{1}{\rho u} \frac{\partial}{\partial y} \left[ \frac{\mu}{N_{Pr}} \frac{\partial i}{\partial y} + \dot{q}_T + u \left( \mu \frac{\partial u}{\partial y} + \tau_T \right) \right] \end{aligned} \quad (C-11)$$

Substituting Equation (C-10) into Equation (C-9):

$$\begin{aligned} -\frac{\partial \tilde{v}}{\partial y} + \tilde{v} \left( \frac{\partial I/\partial y}{i} - u \frac{\partial u/\partial y}{i} \right) &= A - \frac{\tilde{v}}{u} \frac{\partial u}{\partial y} + u \left( \frac{\partial P/\partial x}{P} \right. \\ &\left. + \frac{\partial r/\partial x}{r} \right) + \frac{u^2}{i} \left( A - \frac{\tilde{v}}{u} \frac{\partial u}{\partial y} \right) - \frac{u}{i} \left( B - \frac{\tilde{v}}{u} \frac{\partial I}{\partial y} \right) \end{aligned} \quad (C-12)$$

Making the indicated cancellations and rearranging, Equation (C-12) becomes:

$$\tilde{v} \frac{\partial u}{\partial y} - u \frac{\partial \tilde{v}}{\partial y} = u^2 \left( \frac{\partial P / \partial x}{P} + \frac{\partial r / \partial x}{r} \right) + uA \left( 1 + \frac{u^2}{i} \right) - \frac{u^2}{i} B \quad (\text{C-13})$$

The subscript  $i$  is now used to designate the  $y$  location to be considered. A constant increment  $\Delta y$  is used in the following analysis. Then:

$$i = y_i / \Delta y$$

$$i - 1 = y_{i-1} / \Delta y$$

We now use the central difference approximation:

$$\tilde{v}_i \approx \tilde{v}_{i-1} + \frac{1}{2} \left[ \left( \frac{\partial \tilde{v}}{\partial y} \right)_i + \left( \frac{\partial \tilde{v}}{\partial y} \right)_{i-1} \right] \Delta y \quad (\text{C-14})$$

or

$$\left( \frac{\partial \tilde{v}}{\partial y} \right)_i \approx \frac{2}{\Delta y} (\tilde{v}_i - \tilde{v}_{i-1}) - \left( \frac{\partial \tilde{v}}{\partial y} \right)_{i-1}$$

Equation (C-13) can now be written:

$$\begin{aligned} \tilde{v}_i \left( \frac{\partial u}{\partial y} \right)_i - \frac{2u_i}{\Delta y} (\tilde{v}_i - \tilde{v}_{i-1}) + u_i \left( \frac{\partial \tilde{v}}{\partial y} \right)_{i-1} &= u_i^2 \left( \frac{\partial P / \partial x}{P} + \frac{\partial r / \partial x}{r} \right) \\ + u_i A \left( 1 + \frac{u_i^2}{i_i} \right) - \frac{u_i^2}{i_i} B & \end{aligned} \quad (\text{C-15})$$

Solving for  $\tilde{v}_i$ ,

$$\begin{aligned} \tilde{v}_i &= \left[ \frac{1}{\frac{\partial u}{\partial y}_i - \frac{2u_i}{\Delta y}} \right] \left[ u_i^2 \left( \frac{\partial P / \partial x}{P} + \frac{\partial r / \partial x}{r} \right)_i + u_i A \right. \\ &\quad \left. - \frac{u_i^2}{i_i} (B - uA)_i - 2u_i \frac{(\tilde{v})_{i-1}}{\Delta y} - \left( \frac{\partial \tilde{v}}{\partial y} \right)_{i-1} u_i \right] \end{aligned} \quad (\text{C-16})$$

Replacing A and B in Equation (C-16) using Equation (C-11), the final expression for  $\tilde{v}_i$  now becomes:

$$\begin{aligned} \tilde{v}_i = & \left[ \frac{1}{\frac{\partial u_i}{\partial y} - \frac{2u_i}{\Delta y}} \right] \left\{ u_i^2 \left( \frac{\partial P / \partial x}{P} + \frac{\partial r / \partial x}{r} \right)_i + \frac{1}{\rho_i} \left[ - \frac{\partial P}{\partial x} \right. \right. \\ & + \frac{\partial}{\partial y} \left( u \frac{\partial u}{\partial y} \right) + \left. \frac{\partial \tau_T}{\partial y} \right]_i - \frac{u_i}{i \rho_i} \left[ \frac{\partial}{\partial y} \left( \frac{\mu}{N_{Pr}} \frac{\partial i}{\partial y} \right) + \frac{\partial \dot{q}_T}{\partial y} \right. \\ & \left. \left. + \frac{\partial u}{\partial y} \left( \mu \frac{\partial u}{\partial y} + \tau_T \right) + u \frac{\partial P}{\partial x} \right]_i - 2u_i \frac{\tilde{v}_{i-1}}{\Delta y} - \left( \frac{\partial \tilde{v}}{\partial y} \right)_{i-1} u_i \right\} \end{aligned} \quad (C-17)$$

$\tilde{v}_i$  can now be obtained explicitly from given  $u$  and  $H$  profiles providing that  $\tau_T$ ,  $\dot{q}_T$ ,  $\partial r / \partial x$ , and  $\partial P / \partial x$  are known. First,  $\tilde{v}_i$  is computed using Equation (C-17) with the wall boundary conditions specifying that  $\tilde{v}_0$  and  $(\partial \tilde{v} / \partial y)_0$  are both zero. Next,  $(\partial \tilde{v} / \partial y)_1$  is computed using Equation (C-14). This procedure is repeated until all values of  $\tilde{v}$  in the boundary layer are obtained.

## 2. EVALUATION OF TURBULENT STRESSES

### a. Incompressible Flow

Published methods for estimating turbulent shear stresses were studied, but were found to be unsatisfactory for use in the present analysis. The Prandtl linear mixing length expression provides valid results only when constant shear is assumed. The correlations used by von Karman and van Driest require that the boundary layer be divided into sublayers, with a separate correlation for each sublayer. This procedure would unnecessarily complicate the solution of Equations (C-6) and (C-7).

The general form of the correlation for  $\tau_T$  selected for the turbulent nonsimilar method is derived in the following paragraphs.

Assuming incompressible flat plate flow and that  $\mu \frac{\partial^2 u}{\partial y^2} \ll \tau_T$ , Equations (C-4) and (C-6) reduce to:

$$\tilde{v} = - \int_0^y \frac{\partial u}{\partial x} dy \quad (C-18)$$

and

$$\rho \frac{\partial u}{\partial x} + \rho \tilde{v} \frac{\partial u}{\partial y} = \tau_T \quad (C-19)$$

Following common practice, it is further assumed that the velocity profile and boundary layer thickness are given by

$$\frac{u}{u_e} = \left(\frac{y}{\delta}\right)^{1/7} \quad (\text{C-20})$$

$$\delta = \frac{.37x^{4/5}}{\left(\frac{\rho u_e}{\mu_e}\right)^{1/5}} \quad (\text{C-21})$$

Using Equation (C-20):

$$\frac{\partial u}{\partial y} = \left(\frac{u_e}{\delta}\right) \frac{\partial(u/u_e)}{\partial(y/\delta)} = \frac{1}{7} \left(\frac{u_e}{\delta}\right) \left(\frac{y}{\delta}\right)^{-6/7} \quad (\text{C-22})$$

and

$$\frac{\partial u}{\partial x} = u_e \left[ \frac{\partial(u/u_e)}{\partial(y/\delta)} \right] \left[ \frac{\partial(y/\delta)}{\partial x} \right] = \left(\frac{u_e}{7}\right) \left(\frac{y}{\delta}\right)^{-6/7} \frac{\partial(y/\delta)}{\partial x} \quad (\text{C-23})$$

where

$$\frac{\partial(y/\delta)}{\partial x} = -\left(\frac{y}{\delta^2}\right) \left(\frac{\partial \delta}{\partial x}\right) \quad (\text{C-24})$$

Substituting Equation (C-23) into Equation (C-24):

$$\frac{\partial u}{\partial x} = -\left(\frac{u_e}{7}\right) \left(\frac{y}{\delta}\right)^{1/7} \left(\frac{\partial \delta / \partial x}{\delta}\right) \quad (\text{C-25})$$

Also, it is easily shown that:

$$\int_0^y \left(\frac{\partial u}{\partial x}\right) dy = -\left(\frac{u_e}{8}\right) \left(\frac{y}{\delta}\right)^{8/7} \left(\frac{d\delta}{dx}\right) \quad (\text{C-26})$$

Substituting Equations (C-20), (C-22), (C-25), and (C-26) into Equation (C-22), we get:

$$-\rho \left(\frac{u_e^2}{7}\right) \left(\frac{y}{\delta}\right)^{2/7} \left(\frac{\partial \delta / \partial x}{\delta}\right) + \left(\frac{\rho u_e^2}{56}\right) \left(\frac{y}{\delta}\right)^{2/7} \left(\frac{\partial \delta / \partial x}{\delta}\right) = \frac{\partial \tau_T}{\partial y} \quad (\text{C-27})$$

Combining terms on the left side of Equation (C-27), results in:

$$-\frac{1}{8} \left( \rho u_e^2 \right) \left( \frac{\partial \delta / \partial x}{\delta} \right) \left( \frac{y}{\delta} \right)^{2/7} = \frac{\partial \tau_T}{\partial y} \quad (\text{C-28})$$

From Equation (C-21):

$$\frac{\partial \delta}{\partial x} = \left( \frac{4}{5} \right) \left( \frac{\delta}{x} \right) \quad (\text{C-29})$$

Substituting Equations (C-21) and (C-29) into Equation (C-28):

$$\frac{\partial \tau_T}{\partial y} = - \left( \frac{1}{10} \right) \left( \frac{\rho u_e^2}{x} \right) \left( \frac{y}{\delta} \right)^{2/7} \quad (\text{C-30})$$

Solving for x in Equation (C-29), we get:

$$x = (.37)^{-5/4} \left( \frac{\rho u_e^2}{\mu} \right)^{1/4} \delta^{5/4} \quad (\text{C-31})$$

Replacing the x in Equation (C-30) with Equation (C-31):

$$\frac{\partial \tau_T}{\partial y} = - \left( \frac{1}{10} \right) (.37)^{5/4} \left( \frac{\rho u_e^2}{\mu} \right)^{3/4} \frac{u_e \mu}{\delta^{5/4}} \left( \frac{y}{\delta} \right)^{2/7} \quad (\text{C-32})$$

Equation (C-32) is still unsatisfactory for usage in the turbulent nonsimilar equations, since  $\delta$  is rather arbitrarily defined. This term can be removed using the following substitutions. Differentiating Equation (C-22) with respect to y gives:

$$\frac{\partial^2 u}{\partial y^2} = - \left( \frac{6}{49} \right) \left( \frac{u_e}{\delta^2} \right) \left( \frac{y}{\delta} \right)^{-13/7} \quad (\text{C-33})$$

or

$$- \left( \frac{49}{6} \right) \left( \frac{\delta^2}{u_e} \right) \left( \frac{y}{\delta} \right)^{13/7} \left( \frac{\partial^2 u}{\partial y^2} \right) = 1 \quad (\text{C-34})$$

Multiplying the right side of Equation (C-32) by Equation (C-34):

$$\frac{\partial \tau_T}{\partial y} = \left( \frac{49}{6} \right) \left( \frac{1}{10} \right) (.37)^{5/4} \left( \frac{\rho u y}{\mu} \right)^{3/4} \left( \frac{y}{\delta} \right)^{36/28} \mu \left( \frac{\partial^2 u}{\partial y^2} \right) \quad (\text{C-35})$$

Noting that:

$$(y/\delta)^{36/25} = (u/u_e)^9$$

Equation (C-35) can be expressed by:

$$\frac{\partial \tau_T}{\partial y} = .236 \left( \frac{\rho u y}{\mu} \right)^{3/4} \left( \frac{u}{u_e} \right)^9 \frac{\partial \tau_L}{\partial y} \quad (C-36)$$

where

$$\tau_L = \mu \left( \frac{\partial u}{\partial y} \right)$$

We now have an acceptable equation describing  $\partial \tau_T / \partial y$ . Note that Equation (C-36) depends only on local flow properties and derivatives in  $y$ .

Computations of skin friction made using Equation (C-6), with the expression for  $\partial \tau_T / \partial y$  given by Equation (C-36) were found to be in poor agreement with experimental data. This result is not surprising, considering the approximations used in deriving Equation (C-36). For example, the contribution of the laminar shear term was neglected in deriving Equation (C-36), but was included in making skin friction computations. Also, the  $1/7$  power law profile results in a finite value of  $\partial u / \partial y$  at the edge of the boundary layer, but the correct boundary condition  $(\partial u / \partial y)_e = 0$  is imposed on the program equations.

Equation (C-36) is useful, however, in that it suggests the general form of the required shear parameter given by:

$$\frac{\partial \tau_T}{\partial y} = c \left( \frac{\rho u y}{\mu} \right)^a \left( \frac{u}{u_e} \right)^b \left( \frac{\partial \tau_L}{\partial y} \right) \quad (C-37)$$

Computer results indicated that  $a$  and  $c$  did not appreciably influence the velocity profile. Several values for  $b$  were tried, and the resulting profiles were compared with the empirical results. A value of 12 was selected on the basis of these comparisons. Computed velocity profiles for incompressible flow on a flat plate using  $b = 12$  are shown in Figure 29 along with a  $1/7$  power law profile. The agreement appears reasonably good, although some difference in profile shape is noted.

The constant  $c$  and exponent  $a$  were determined on the basis of comparisons of skin friction results from the program with estimates obtained using the well established empirical methods. Analysis of skin friction results from the program indicated that the variation in skin friction coefficient with Reynolds number  $d(\ln C_f) / d(\ln N_{R,e})$  is determined by the exponent  $a$ . After establishing the correct

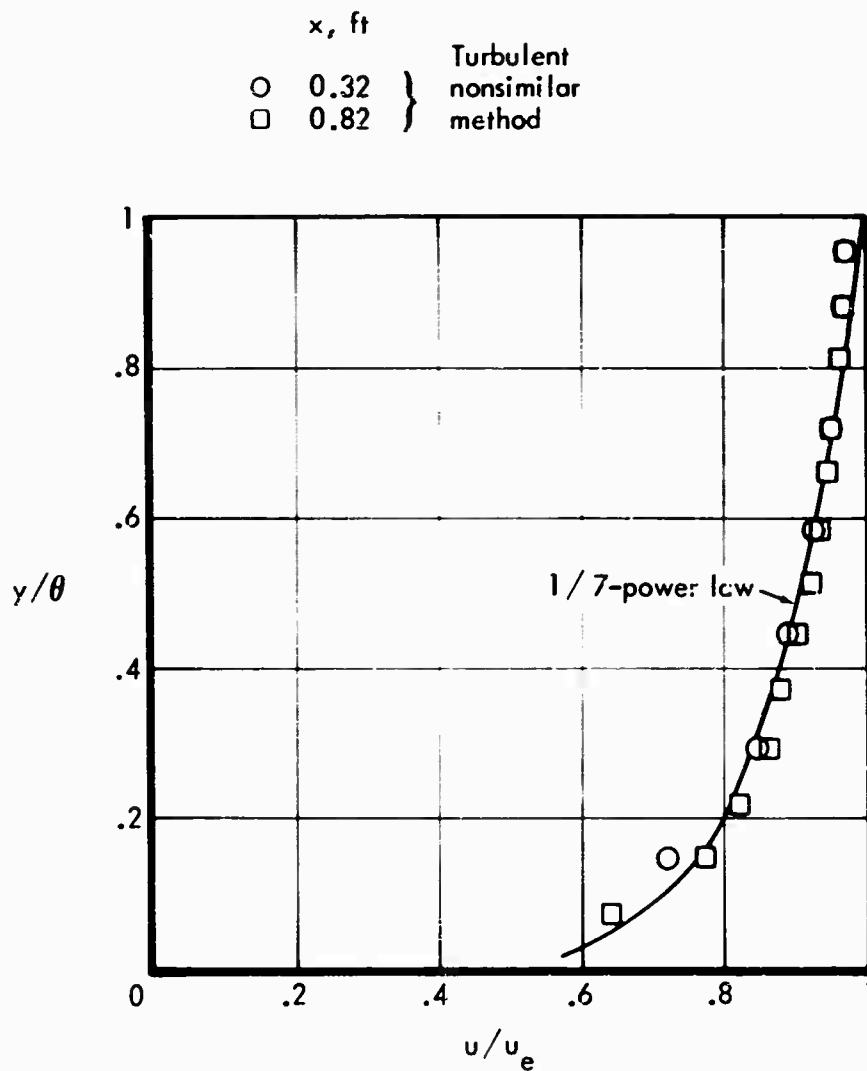


Figure 29: COMPARISONS OF TURBULENT VELOCITY PROFILES FOR INCOMPRESSIBLE FLOW ON A FLAT PLATE

trend of  $C_f$  with  $N_{R,e}$  the constant  $c$  was selected to yield the correct magnitude of  $C_f$ . Results obtained using  $a = .833$  and  $c = .054$  are shown in Figure 30, along with the Schultz-Grunow (Reference 9) correlation. The agreement is seen to be good for all Reynolds numbers investigated.

#### b. Compressible Flow

In order to extend the program capability to include compressible flow it was necessary, first, to determine thermal effects on the turbulent shear term  $\partial\tau_T/\partial y$ , and secondly, to evaluate the turbulent conduction term  $\dot{q}_T$ . The turbulent shear and conduction were assumed to be related by an effective turbulent Prandtl number  $N_{Pr,T}$  in the same way as the corresponding laminar terms. Thus,

$$\dot{q}_T = \frac{\epsilon}{N_{Pr,T}} \frac{\partial i}{\partial y} \quad (C-35)$$

where

$$\epsilon = \frac{\tau_T}{\partial u / \partial y}$$

Since the turbulent Prandtl number has very little influence on skin friction, it is possible to consider thermal effects on the shear stress and turbulent Prandtl number separately.

Appropriate modifications to the turbulent shear were determined by considering adiabatic flow on a flat plate. The compressible form for the turbulent shear gradient was assumed to be of the form:

$$\frac{\partial\tau_T}{\partial y} = \left(\frac{\rho}{\rho_e}\right)^d \left[ .054 \left(\frac{\rho u y}{\mu}\right)^{.833} \left(\frac{u}{u_e}\right)^{12} \frac{\partial}{\partial y} \left(\mu \frac{\partial u}{\partial y}\right) \right] \quad (C-39)$$

The selection of the form given by Equation (C-39) was somewhat intuitive, since no theoretical basis could be found for estimating compressibility effects. The justification for this selection must be based on comparisons with data.

Program results were found to furnish good agreement with experimental data presented in Reference 26 with  $d = 4$ , as shown in Figure 31. The compressible skin friction coefficients were obtained using the Schultz-Grunow method. The influence of Reynolds number on  $C_f/C_{f,inc}$  is known to be quite small, and is neglected in these comparisons.

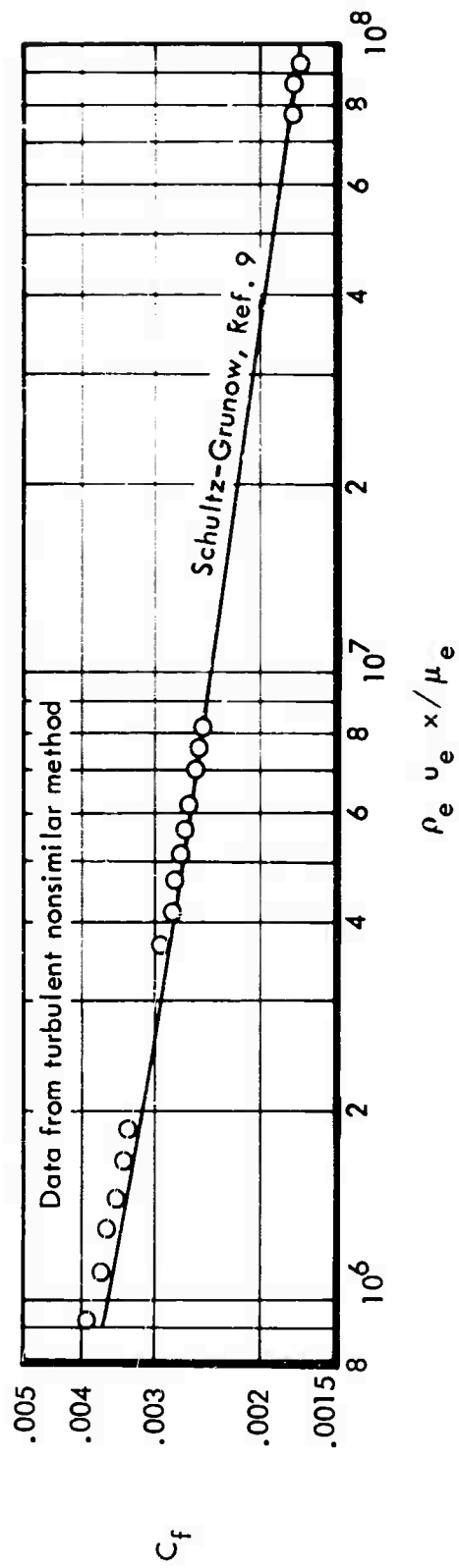


Figure 30: COMPARISONS OF TURBULENT SKIN FRICTION COEFFICIENTS FOR INCOMPRESSIBLE FLOW ON A FLAT PLATE

All experimental data from Ref. 26

- |                        |                               |
|------------------------|-------------------------------|
| ○ Brinich and Diaconis | ◻ Monaghan and Cooke          |
| ◻ Chapman and Kester   | ◻ Monaghan and Johnson        |
| △ Cales                | ◊ O'Donnell                   |
| ◊ Goddard              | ◻ Rubesin, Maydew, and Varga  |
| ◻ Hakkinen             | ◊ Shutts, Hartwis, and Weller |
| ◻ Korkegi              | ◊ Wade                        |
| ▽ Matting, et al.      | ◻ Wilson                      |

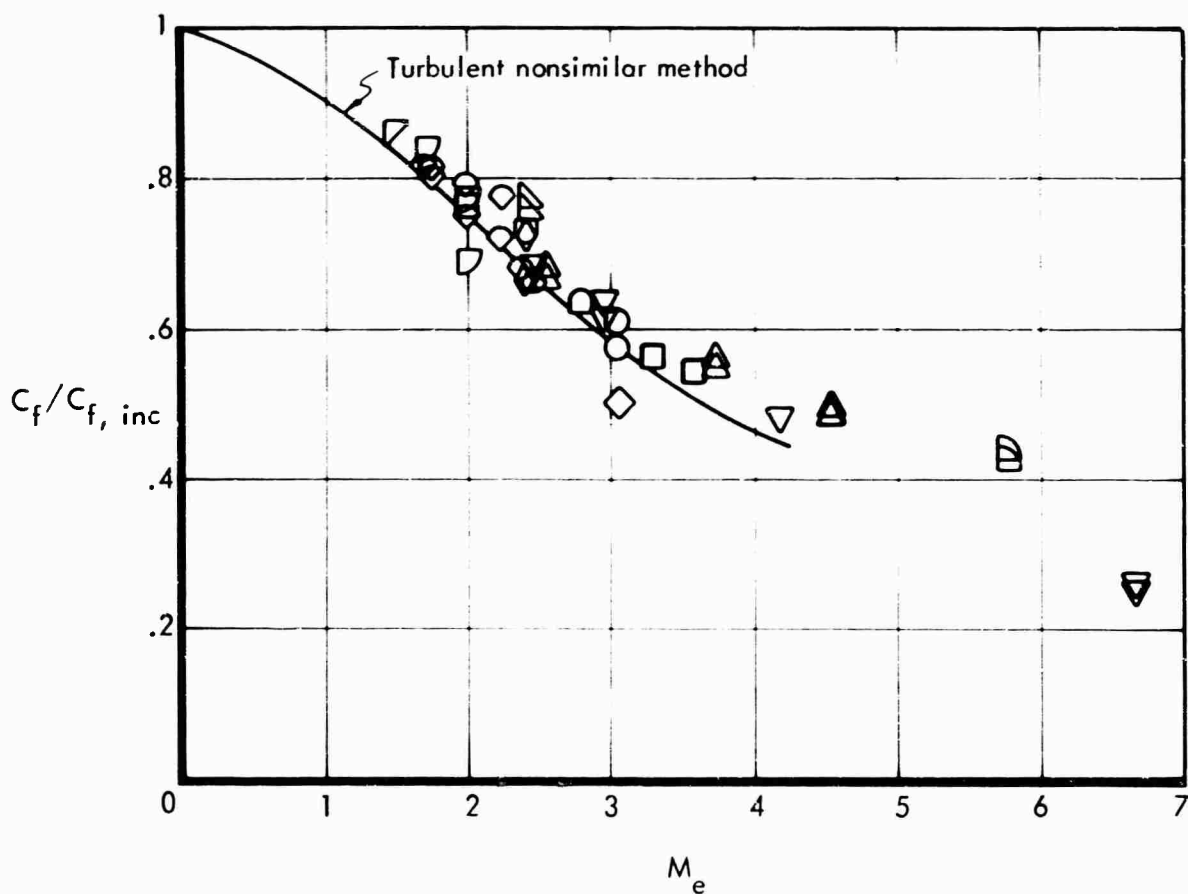


Figure 31: MACH NUMBER EFFECT ON TURBULENT SKIN FRICTION FOR ADIABATIC FLOW ON A FLAT PLATE

The combined effects of Mach number and wall cooling are shown in Figure 32. Qualitative agreement between program results and data is noted regarding trends with Mach number and wall cooling, but predicted values appear to be generally lower than the data.

Unlike skin friction, heat transfer rates are strongly influenced by the turbulent Prandtl number. Since the turbulent Prandtl number cannot be obtained directly from experimental results, the evaluation is made on the basis of the turbulent recovery factor ( $r$ ), where:

$$r \equiv \frac{i_{aw} - i_e}{I_e - i_e} \quad (C-40)$$

$i_{aw}$  is the adiabatic wall enthalpy.  $I_e$  and  $i_e$  are the total and static enthalpies evaluated at the edge of the boundary layer. Experimental results (e.g., Reference 27) have shown that for turbulent flat plate flows  $r$  is approximately 0.9. In order to establish the corresponding value of  $N_{Pr,T}$ , program solutions are obtained using  $N_{Pr,T} = 1.0, 0.85,$  and  $0.71$ . The wall temperature is the adiabatic wall temperature based on  $r = .9$ .

Turbulent Prandtl numbers are plotted against  $r$  in Figure 33, where  $r$  was computed by:

$$r = \frac{(\dot{q}_w/H) + i_w - i_e}{I_e - i_e} \quad (C-41)$$

The heat flux  $\dot{q}$  is obtained directly from the program, and  $H$  is computed from the skin-friction coefficient using a Reynolds analogy given by

$$\frac{H}{\rho_e u_e} = \frac{C_f}{2 N_{Pr,T}} \quad (C-42)$$

The recovery factors are shown in Figure 33 to be correlated by

$$r = N_{Pr,T}^{1.07} \quad (C-43)$$

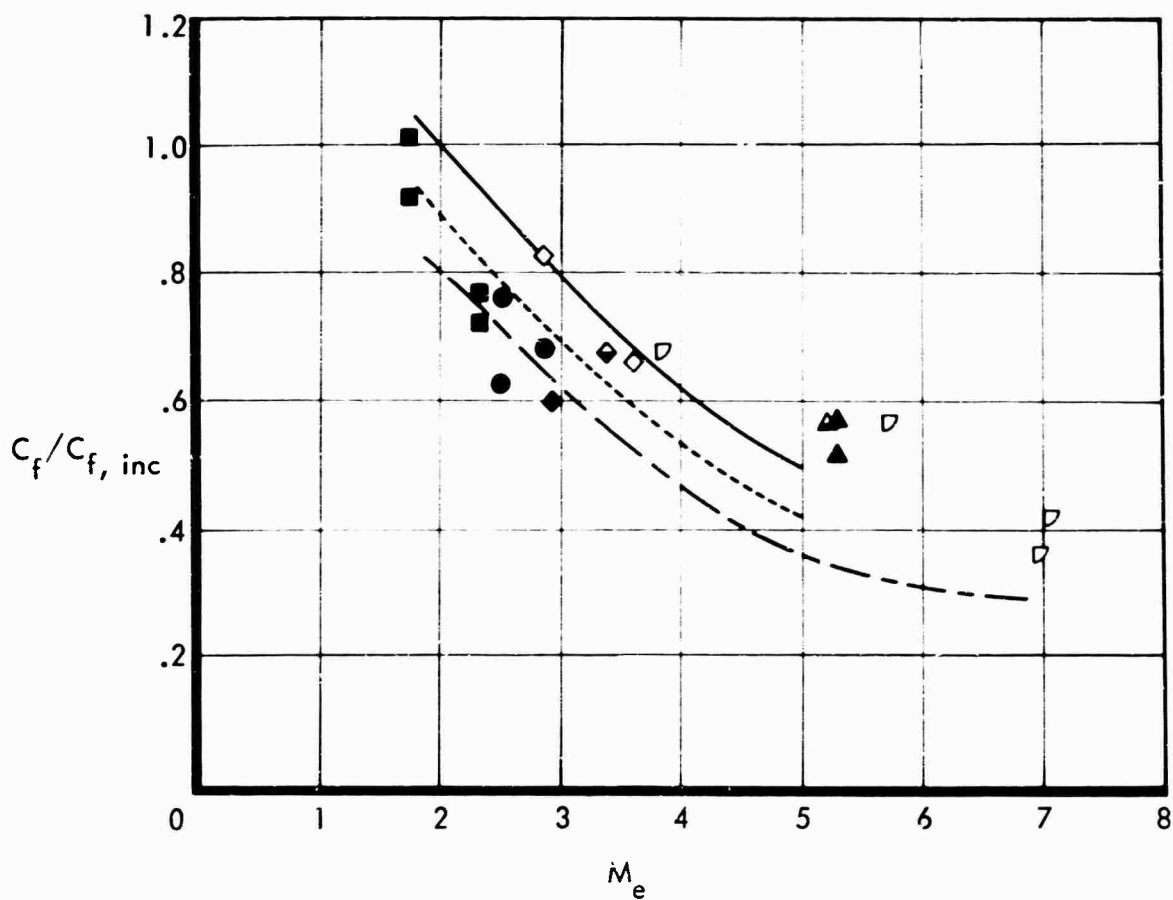
Thus, for  $r = 0.9$

$$N_{Pr,T} \approx 0.9 \quad (C-44)$$

The selection of  $N_{Pr,T}$  completes the evaluation of the Reynolds stresses appearing in Equations (C-6), (C-7), and (C-17).

All experimental data from Ref. 26

$T_w/T_o$	Author
○ 1.35 to 1.58	Monaghan and Cooke
□ 1.04 to 1.08	Pappas
△ 0.58 to 0.85	Winkler and Cha
◇ 0.49 to 0.80	Swanson, Buglia, and Chauvin
▽ 0.16 to 0.40	Sommer and Short



$T_w/T_o$	Symbol Type	Condition
0.2	} Turbulent nonsimilar method	Open symbols, $T_w/T_o < 0.5$
0.5		Semifilled symbols, $0.5 < T_w/T_o < 0.8$
0.8		Filled symbols, $T_w/T_o > 0.8$

Figure 32: COMBINED EFFECTS OF MACH NUMBER AND WALL COOLING ON TURBULENT SKIN FRICTION ON A FLAT PLATE

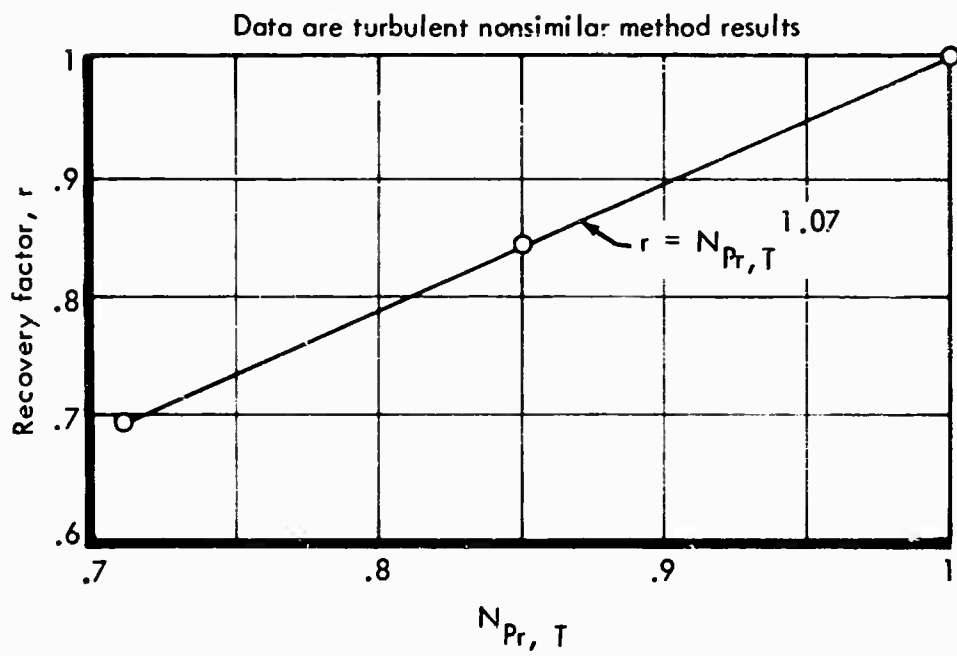


Figure 33: TURBULENT PRANDTL NUMBER EFFECT ON RECOVERY FACTOR

### 3. HEAT TRANSFER RESULTS

Comparisons of heating rates calculated using the turbulent nonsimilar and the  $\rho_r \mu_r$  programs are shown below for a range of Mach numbers and enthalpy ratios.

$M_e$	$u_e$ , ft/sec	$i_w/I_e$	$\dot{q}$ , Btu/ft <sup>2</sup> -sec	
			Turbulent nonsimilar method	$\rho_r \mu_r$ method
5.06	5946	.502	56.6	54.0
5.03	5923	.8	13.8	14.88
4.77	5840	.204	113.1	108.7
1.75	1993	.802	4.7	4.8
1.74	1989	.501	14.8	14.34
1.70	1926	.207	26.4	23.0

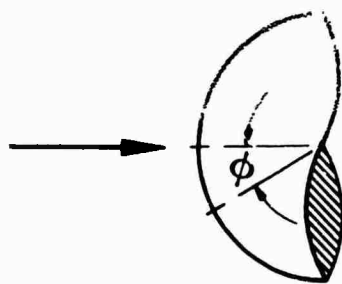
Heat transfer rates from the two programs are seen to agree within 5% except for the case where  $M_e = 1.7$  and  $i_w/I_e = 0.207$ .

Comparisons between turbulent heating estimates from the nonsimilar and  $\rho_r \mu_r$  methods for a hemisphere are presented in Figure 34. The discrepancy seen near the stagnation point occurs because the  $\rho_r \mu_r$  method extrapolates to zero at the stagnation point, but the nonsimilar method provides the laminar value at that point. At angles greater than about 30 degrees the two methods are in good agreement.

Heat transfer rates for the linear wall temperature case shown in Figure 10 were also computed using the nonsimilar method. The nonsimilar results are not shown since differences with the  $\rho_r \mu_r$  predictions are so small that they would not be discernible.

### 4. ACCURACY AND STABILITY

It must be kept in mind that the results from the turbulent nonsimilar method do not represent solutions to Equations (C-6) and (C-7), but are solutions to a set of algebraic equations approximating the partial differential equations. First, the size of the grid net must be sufficiently small to allow an accurate description of the boundary layer profiles. Secondly, numerical instabilities must be avoided in performing the step-by-step integration.



$$M_\infty = 6.38$$

$$D = 5 \text{ inches}$$

$$T_w = 650^\circ\text{R}$$

$$I = 13.4 \times 10^6 \text{ ft}^2/\text{sec}^2$$

$$P_s = 86.9 \text{ psia}$$

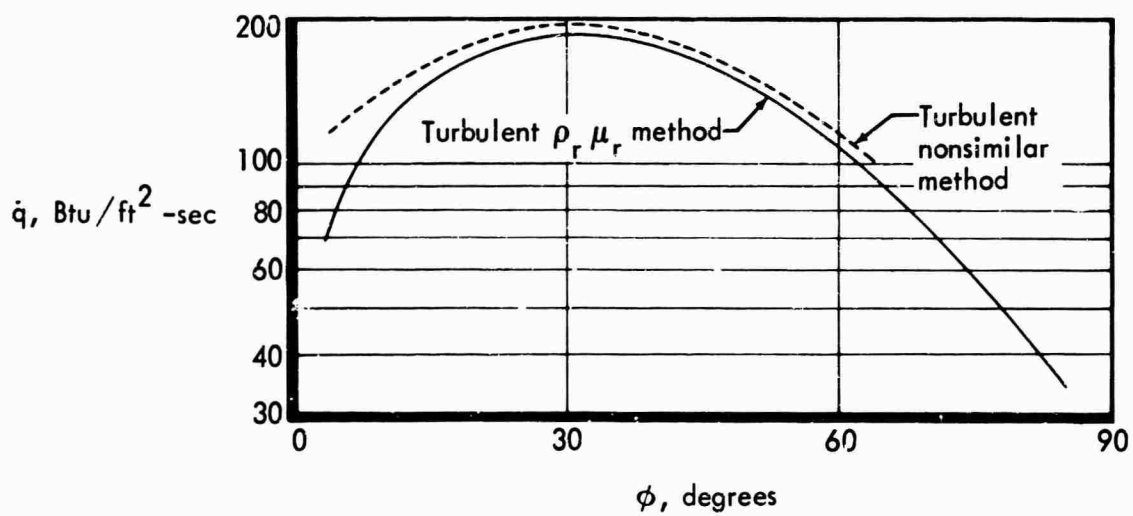


Figure 34: TURBULENT HEATING DISTRIBUTION ON A HEMISPHERE

a. Accuracy

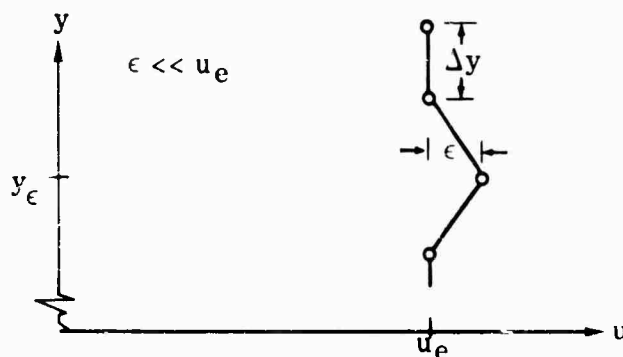
Solutions obtained near the leading edge of a flat plate are clearly not valid, since the boundary layer is described by only a few points. The minimum number of nodes within the boundary layer needed to obtain satisfactory solutions can be determined by examining program results along the plate. Results shown in Figure 35a indicate that for incompressible flow over a flat plate, skin-friction estimates are within 2 - 3% of the Karman-Schoenherr values when the velocity at the first node from the wall is smaller than 75% of the value at the boundary layer edge. A similar study was made for compressible flows by assuming that Mach number and wall cooling effects on skin friction are constant along the plate. The computed skin-friction coefficients should then be proportional to the corresponding incompressible values along the plate. Typical results shown in Figure 35b indicate that the accuracy criterion given for incompressible flows will provide good results for compressible flows. The influence of the incremental streamwise distance  $\Delta x$  on accuracy has been found to be negligible provided the numerical instabilities are avoided.

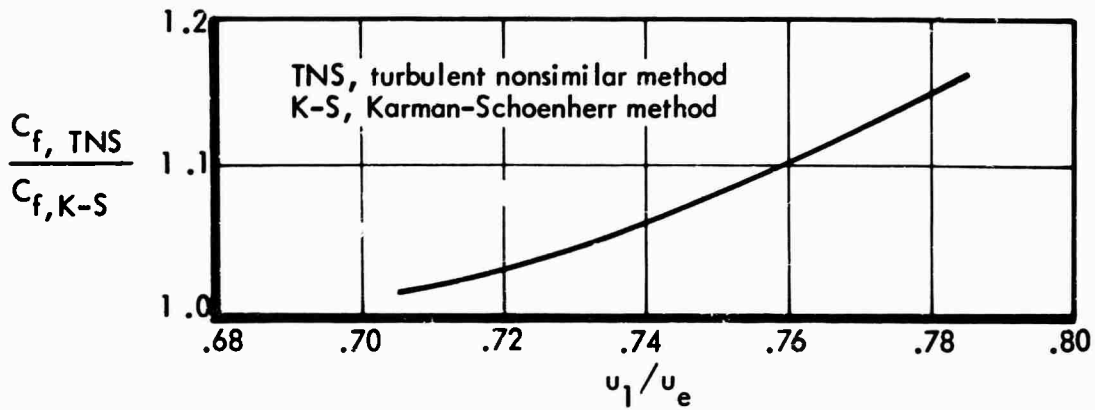
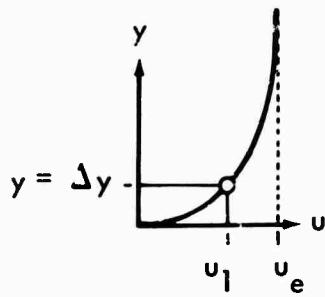
b. Numerical Instabilities

Examination of computer results show that numerical instabilities always originate near the edge of the boundary layer, where oscillations in velocity and enthalpy were sometimes amplified to the extent that the program results became meaningless. Although no rigorous analysis for stability appears possible at this time, an approximate criterion is presented which is in excellent agreement with observed computer results. The instabilities are assumed to arise from the highest order differential, i.e., the shear term. The laminar shear contribution is assumed to be negligible compared to the turbulent value. The momentum equation at the boundary layer edge then becomes

$$\rho_e u_e \frac{\partial u}{\partial x} = .054 \left( \frac{\rho_e u_e y}{\mu_e} \right)^{.833} \mu_e \frac{\partial^2 u}{\partial y^2} \quad (C-45)$$

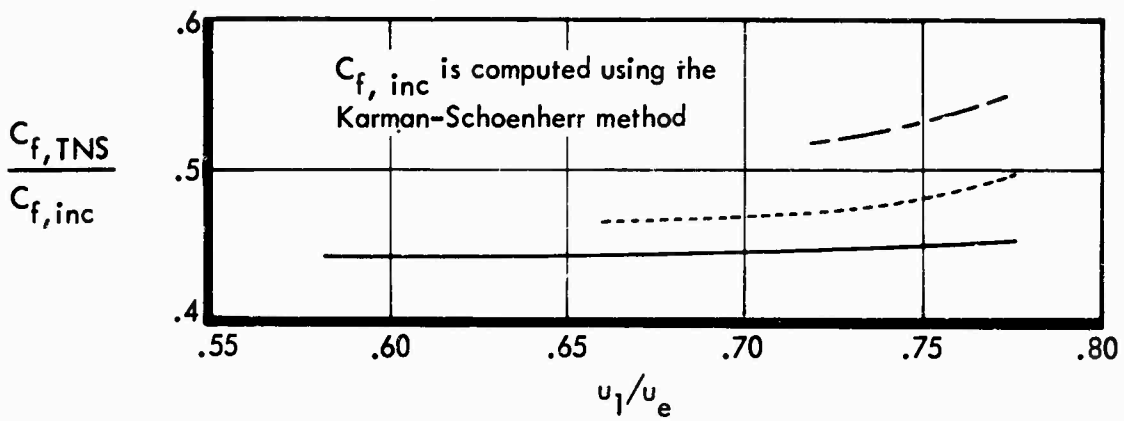
Initially, the velocity at one node is given by  $u = u_e + \epsilon$  where  $\epsilon$  is the initial error in computed velocity at  $y = y_\epsilon$ .





a) Incompressible Flow

	$M_e$	$T_w/T_o$
————	4.36	0.915
-----	3.96	0.920
-----	4.96	0.204



b) Compressible Flow

Figure 35: EFFECT OF  $\Delta y$  ON PREDICTED SKIN-FRICTION COEFFICIENTS

N is now defined as the number of nodes from the wall to  $y_\epsilon$ . Hence,

$$y_\epsilon = N\Delta y \text{ and } \left(\frac{\partial^2 u}{\partial y^2}\right)_{y_\epsilon} = \frac{2\epsilon}{\Delta y^2}$$

Equation (41) can now be written:

$$\begin{aligned} \left(\frac{\partial u}{\partial x}\right)_{y_\epsilon} &= -.054 \left(\frac{\mu_e}{\rho_e u_e}\right)^{.167} (N\Delta y)^{.833} \frac{2\epsilon}{\Delta y^2} \\ &= -.108 \left(\frac{\mu_e}{\rho_e u_e}\right)^{.167} \left[\frac{(N)^{.833}}{(\Delta y)^{1.167}}\right] (\epsilon) \end{aligned} \quad (C-46)$$

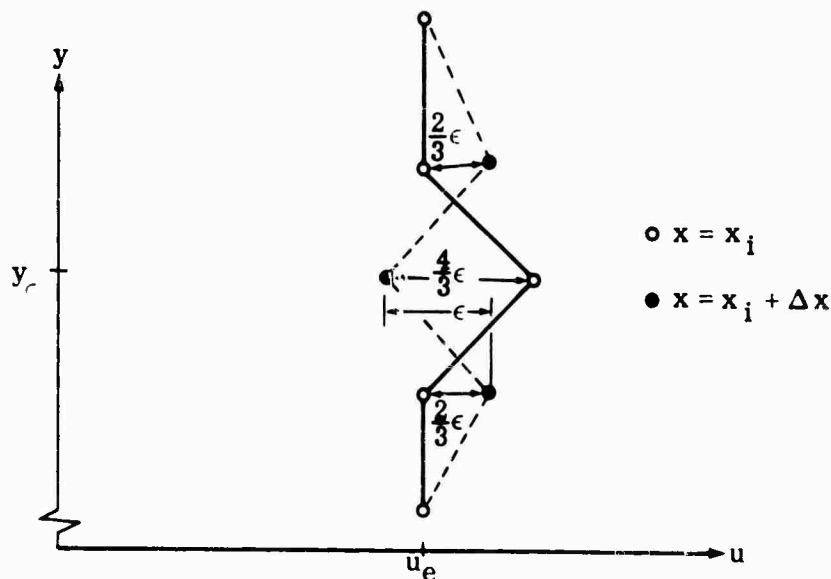
Neutral stability occurs when the difference between  $u$  at  $y_\epsilon$  and the two adjacent nodes remains unchanged at the adjacent downstream station, then the velocity gradient at the adjacent nodes is given by:

$$\left(\frac{\partial^2 u}{\partial y^2}\right)_{y_\epsilon \pm \Delta y} = \frac{\epsilon}{\Delta y^2} \quad (C-47)$$

then

$$\left(\frac{\partial u}{\partial x}\right)_{y_\epsilon \pm \Delta y} = .054 \left(\frac{\mu_e}{\rho_e u_e}\right)^{.167} \left[\frac{N^{.833}}{\Delta y^{1.167}}\right] (\epsilon) \quad (C-48)$$

The velocity profiles at the two  $x$  locations are sketched below:



It is seen that the difference between  $u_{y_\epsilon}$  and  $u_{y_\epsilon + \Delta y}$  is constant at the two  $x$  locations when

$$\left(\frac{\partial u}{\partial x}\right)_{y_\epsilon} = -\frac{4}{3} \frac{\epsilon}{\Delta x_{ns}} \quad (C-49)$$

where  $\Delta x_{ns}$  is the  $\Delta x$  required for neutral stability. Substituting Equation (C-49) into Equation (C-46) gives:

$$\frac{4}{3} \frac{\epsilon}{\Delta x_{ns}} = .108 \left(\frac{\rho_e u_e}{\mu_e}\right)^{.167} \left[\frac{N^{.833}}{\Delta y^{1.167}}\right] (\epsilon) \quad (C-50)$$

or

$$\Delta x_{ns} = \frac{12.26}{N^{.833}} \left(\frac{\rho_e u_e}{\mu_e}\right)^{.167} \Delta y^{1.167} \quad (C-51)$$

Thus, it is concluded that if  $\Delta x$  exceeds the value given by Equation (C-50) small oscillations in velocity will be amplified. Since small oscillations are unavoidable because of round-off errors, it is concluded that stability can be maintained only if  $\Delta x < \Delta x_{ns}$ . This conclusion is supported by computer results for two cases shown in Figure 36. The points presented as unstable are from the first  $x$  location at which oscillations are observed.

Equation (C-51) defines the maximum incremental distance  $\Delta x$  for neutral stability. In specifying the grid size to be used for normal operation of the turbulent nonsimilar program it is recommended that

$$\Delta x = \frac{\Delta x_{ns}}{2} = \frac{6.13}{N_{max}^{.833}} \left(\frac{\rho_e u_e}{\mu_e}\right)^{.167} \Delta y^{1.167} \quad (C-52)$$

where  $N_{max}$  is the number of points to be computed at the most downstream  $x$  location to be considered.

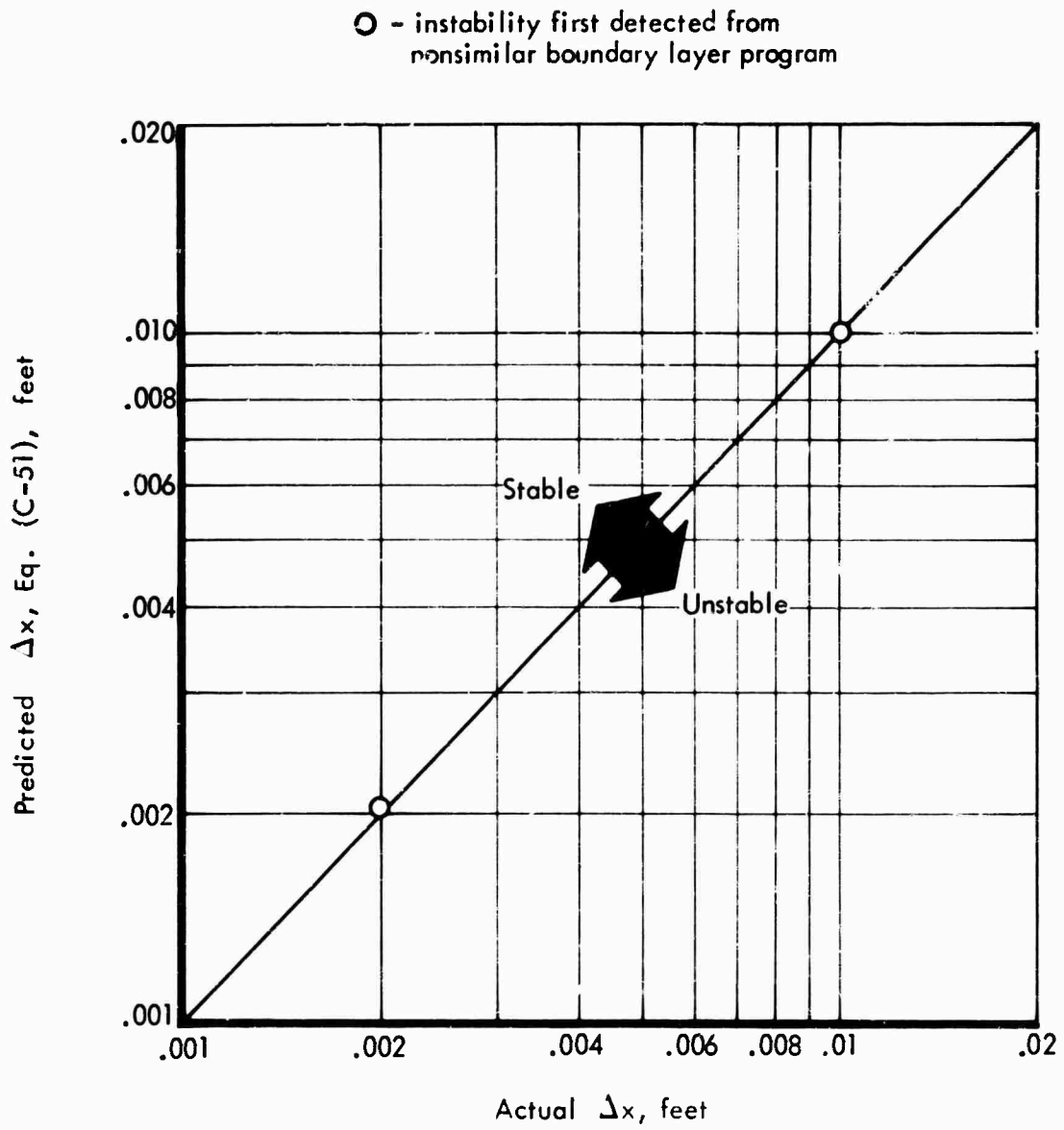


Figure 36: NUMERICAL STABILITY CRITERIA FOR NONSIMILAR BOUNDARY LAYER PROGRAM

## REFERENCES

1. Hanks, R. A. ; and Savage, R. T. : Thermal Design Methods for Recoverable Launch Vehicles with Consideration of Arbitrary Wall Temperatures and Surface Conditions, NASA CR-74714, August 1965.
2. Nagel, A. L. ; Fitzsimmons, H. D. ; and Doyle, L. B. : Analysis of Hypersonic Pressure and Heat Transfer Tests on Delta Wings with Laminar and Turbulent Boundary Layers, NASA CR-535, August 1966.
3. Mager, A. : "Transformation of the Compressible Turbulent Boundary Layer," JAS, Vol. 25, No. 5, May 1958, pp. 305-311.
4. Thomas, A. C. ; and Perlbachs, A. : Application of Ground Test Data to Reentry Vehicle Design, AFFDL-TR-66-229, Air Force Flight Dynamics Laboratory, Wright-Patterson Air Force Base, Ohio, January 1967.
5. Thomas, A. C. ; Perlbachs, A. ; and Nagel, A. L. : Advanced Reentry Systems Heat-Transfer Manual for Hypersonic Flight, AFFDL-TR-65-195, Air Force Flight Dynamics Laboratory, Wright-Patterson Air Force Base, Ohio, October 1966.
6. Jaeck, C. ; and Jackson, W. : Nonsimilar Boundary Layer - Real Gas Computer Program - Deck AS1188, Boeing Document D2-81296, DDC AD 446 581, August 1964.
7. Schlichting, Hermann: Boundary Layer Theory, Fourth Edition, McGraw-Hill Book Co., New York, 1960.
8. van Driest, E. R. : "Turbulent Boundary Layer Flow in Compressible Fluids," JAS, Vol. 18, No. 3, March 1951.
9. Schultz-Grunow, F. : New Frictional Resistance Law for Smooth Plates, NACA Memorandum No. 986, August 1940.
10. Wallace, J. E. ; and McLaughlin, E. J. : Experimental Investigations of Hypersonic, Turbulent Flow and Laminar, Leeward-Side Flow on Flat Plates, AFFDL-TR-66-63, Air Force Flight Dynamics Laboratory, Wright-Patterson Air Force Base, Ohio, July 1966.
11. Cohen, C. B. ; and Reshotko, E. : Similar Solutions for Compressible Laminar Boundary Layer with Heat Transfer and Pressure Gradient, NACA TN 3325, February 1955.
12. Kennet, Haim: The Inviscid Hypersonic Flow on the Windward Side of a Delta Wing, IAS Paper No. 63-55, 1963.

#### REFERENCES (Continued)

13. Eichorn, R.; Eckert, E. R. G.; and Anderson, A. D.: An Experimental Study of the Effects of Non-Uniform Wall Temperature on Heat Transfer in Laminar and Turbulent Axisymmetric Flow along a Cylinder, WADC-TR-58-33, Wright Air Development Center, Wright-Patterson Air Force Base, Ohio, July 1958.
14. Beckwith, I. E.; and Gallagher, J. J.: Local Heat Transfer and Recovery Temperatures on a Yawed Cylinder at a Mach Number of 4.15 and High Reynolds Numbers, NASA Memo 2-27-59L, April 1959.
15. van Hise, Vernon: Analytic Study of Induced Pressure on Long Bodies of Revolution with Varying Nose Bluntness at Hypersonic Speeds, NASA TR R-78, 1961.
16. Hansen, C. F.: Approximations for the Thermodynamic and Transport Properties of High Temperature Air, NACA TN 4150, March 1958.
17. Moeckel, W. E.; and Weston, K. C.: Composition and Thermodynamic Properties of Air in Chemical Equilibrium, NACA TN 4265, April 1958.
18. Howarth, L.: "Velocity and Temperature Distribution for a Flow Along a Flat Plate," Proceedings of the Royal Society, London, 1936.
19. Fay, J. A.; and Riddell, F. R.: Theory of Stagnation Point Heat Transfer in Dissociated Air, AVCO Research Report No. 1, April 1957.
20. Kemp, N. H.; Rose, P. H.; and Detra, R. W.: Laminar Heat Transfer Around Blunt Bodies in Dissociated Air, AVCO Research Report No. 15, May 1958.
21. Reshotko, E.; and Beckwith, I. E.: Compressible Laminar Boundary Layer Over a Yawed infinite Cylinder with Heat Transfer, NACA TN 3986, June 1957.
22. Cohen, N. B.: Boundary Layer Similar Solutions and Correlation Equations for Laminar Heat Transfer Distribution in Equilibrium Air at Velocities up to 41,000 Feet Per Second, NASA TR R-118, 1961.
23. Reshotko, E.: Laminar Boundary Layer with Heat Transfer on a Cone at Angle of Attack in a Supersonic Stream, NACA TN 4152, December 1957.
24. Young, G. B. W.; and Janssen, E.: "The Compressible Boundary Layer," JAS, Vol. 19, No. 4, April 1952.
25. Savage, R. T.: A Method for Computing Turbulent Boundary Layer Profiles using Finite Differences, M. S. Thesis, University of Washington, 1966.

REFERENCES (Concluded)

26. Peterson, J. B.: A Comparison of Experimental and Theoretical Results for the Compressible Turbulent Boundary Layer Skin Friction with Zero Pressure Gradient, NASA TN D-1795, March 1963.
27. Schubauer, G. B.; and Tchen, C. M.: Turbulent Flow, Princeton University Press, 1959.

UNCLASSIFIED  
Security Classification

DOCUMENT CONTROL DATA - R&D		
<small>(Security classification of title, body of abstract and indexing annotation must be entered when the overall report is classified.)</small>		
1. ORIGINATING ACTIVITY (Corporate author) The Boeing Company P. O. Box 3868 Aerospace Group Seattle, Washington Space Division - Kent Facility 98124		2a. REPORT SECURITY CLASSIFICATION <b>UNCLASSIFIED</b>
		2b. GROUP
3. REPORT TITLE <b>INVESTIGATION OF TURBULENT HEAT TRANSFER AT HYPERSONIC SPEEDS Volume I - Analytical Methods</b>		
4. DESCRIPTIVE NOTES (Types of report, and inclusive dates) <b>Final Report (March 1965 to March 1967)</b>		
5. AUTHORS (First name, middle initial, last name) <b>Savage, Richard T. Jaeck, Carl L.</b>		
6. REPORT DATE <b>December 1967</b>	7a. TOTAL NO. OF PAGES <b>118</b>	7b. NO. OF REFS <b>27</b>
8a. CONTRACT OR GRANT NO. <b>AF33(615)-2372</b>	9a. ORIGINATOR'S REPORT NUMBERS <b>D2-113531-1</b>	
b. Project no. <b>1366</b>		
c. Task no. <b>136607</b>	9b. OTHER REPORT NO(S) (Any other numbers that may be assigned this report)	
d. <b>BPSN 5(61136-62405334)</b>	<b>AFFDL-TR-67-144, Volume I</b>	
10. DISTRIBUTION STATEMENT <b>This document has been approved for public release and sale; its distribution is unlimited.</b>		
11. SUPPLEMENTARY NOTES	12. SPONSORING MILITARY ACTIVITY <b>Air Force Flight Dynamics Laboratory Air Force Systems Command Wright-Patterson Air Force Base, Ohio 45433</b>	
13. ABSTRACT <p>This report presents a combined analytical and experimental investigation of turbulent heat transfer on basic and composite configurations at hypersonic speeds. The analytical results are presented in Volume I, the experimental results, including data-theory comparisons, are presented in Volume II, and computer programs incorporating the analytical methods described herein are presented in Volume III.</p> <p>Two analytical approaches are presented: the <math>\rho_r \mu_r</math> method and the turbulent nonsimilar boundary layer method.</p> <p>The <math>\rho_r \mu_r</math> method, which is derived from the boundary layer momentum and energy integral equations, is recommended for predicting turbulent heating rates. Effects of dissociation, pressure and wall temperature gradients, three-dimensional flow, and nose bluntness are included. Simplified methods for making turbulent heating estimates using slide-rules or desk calculators are also presented. The computation of heating rates on a typical reentry configuration in flight and the extrapolation of test data from ground test facilities to flight are described.</p> <p>The turbulent nonsimilar boundary layer approach offers several advantages over previous methods, and is recommended for specific parametric studies of turbulent flows. Calculations made using this method have been restricted to ideal gases. Modifications can be made to include real-gas effects.</p>		

**UNCLASSIFIED**

Security Classification

14.	KEY WORDS	LINK A		LINK B		LINK C	
		ROLE	WT	ROLE	WT	ROLE	2 T
	Aerodynamic Heating						
	Laminar Flow						
	Turbulent Flow						
	Boundary Layer						
	Streamwise Pressure Gradient						
	Crossflow Pressure Gradient						
	Hypersonic Speed						

**UNCLASSIFIED**

Security Classification